Dynamical Evolution of Stars and Planets in Star-Forming Regions

Emma Daffern-Powell

Department of Physics & Astronomy
The University of Sheffield

A dissertation submitted in candidature for the degree of Doctor of Philosophy at the University of Sheffield

December 2021

Declaration

I declare that the work presented in this thesis is my own. No part of this thesis has been accepted or is currently being submitted for any other qualification at the University of Sheffield or elsewhere.

Much of the work presented here has been published, submitted, or is in preparation as the following journal articles:

Daffern-Powell & Parker (2020) *Dynamical evolution of fractal structures in star-forming regions.* Monthly Notices of the Royal Astronomical Society. Volume 493(4). Pages 4925-4935.

Daffern-Powell, Parker & Quanz (submitted) *The Great Planetary Heist: Theft and capture in star-forming regions.* Monthly Notices of the Royal Astronomical Society.

Daffern-Powell & Parker (in-prep) *Can Jupiters form before they are ejected?* Monthly Notices of the Royal Astronomical Society Letters.

Acknowledgements

First, I must thank Richard Parker, for being such a supportive and kind supervisor. And, I hate to admit it, but also for making me do a conference talk within the first 6 months... You really got me through. I only wish we had have had the chance to go to the pub more this last couple of years.

I also need to thank Simon Goodwin for being such an amazing 3rd and 4th year project supervisor. Your projects showed me how much I enjoyed coding and got me started with Fortran nice and early. I'd also like to thank Clive Tadhunter. I don't know if he knows it, but he is the best person in the department to direct your talk to because he always looks so engaged and interested, and it's really helped me whenever I've been nervous presenting.

Outside of the department, my two dyspraxia tutors, Eleanor Machin and Emma Tudhope, have been invaluable this past year.

Lastly, I can't thank my family enough. My parents have been endlessly supportive and encouraging. And I wouldn't have wanted to do this PhD in the first place if it wasn't for all of the childhood sci-fi watching with them. Finally, my husband, Nath, who I can't imagine the past four years without, and who kept me very well stocked with sweets while writing up, even though he never failed to pass up on an opportunity to remind me that I'm still a student.

Summary

Most stars, and their planets, appear to form within filamentary structures within giant molecular clouds. These filaments funnel the stars into central hubs, where the filaments intersect. Most stars and planets, therefore, form in groups where the relative proximity to other stars can affect both their formation and evolution.

In this thesis, I begin by investigating how we can quantify and model the substructured nature of star-forming regions. Contrary to recent work, I find that the well-established Q-parameter method remains an appropriate analysis for determining the amount and type of substructure in observed star-forming regions. However, the main components of the Q-parameter should not be directly compared to idealised geometries, such as synthetic box-fractals and Plummer spheres, that have not undergone dynamical evolution.

I then run N-body simulations of planets in star-forming regions and investigate how their evolution may be affected by dynamical interactions with other bodies. Two possible outcomes for a planet are its capture or theft. In planet capture, a planet is first ejected from its original system by a dynamical interaction, and is then free-floating before being captured by a passing star. In planet theft, a planet is directly exchanged between two passing stars. I find that planets that have been captured and stolen have distinct orbital properties, and it may therefore be possible to observationally distinguish populations of them.

Finally, I consider the destructive effects that photoevaporation can have on the formation of planets whose orbits are later disrupted. I find that many planets that are disrupted or ejected from their system in previous studies, such as my own, may not fully form due to external photoevaporation of their protoplanetary disks.

Table of Contents

Chapter 1

Introduction

1.1 Motivation for Study

Stars can be seen as the atoms of the universe, and humans seem to have wondered about their origin since prehistoric times. Today, the study of star and planet formation has far-reaching ties to other fields, such as the physics of magnetism, the chemistry of molecule formation, and the biology of life both on Earth and potentially elsewhere in the universe. More specifically, within modern astronomy, star formation is closely linked to our understanding of how stars and their planets evolve, as well as the environments within which this happens.

Most recently, there has been a paradigm shift in the view of how the material in giant molecular clouds collects to form stars. We now know that giant molecular clouds are highly substructured and that the star formation within them occurs in filamentary structures, which funnel the young stars into central hubs. Consequently, stars and planets often form in areas of high local density where their evolution is partially determined by dynamical interactions and their proximity to massive stars.

The implications of this are diverse. For example, our Solar System may be unusual and have been partly shaped by dynamical interactions, while chemical enrichment from a nearby supernova may have provided the conditions for life as we know it on Earth. Further afield, exoplanets have been observed on unexpectedly wide orbits, and the population of free-floating planets is likely to be significant. Both free-floating and wide-orbit planets are likely to result from planet-planet scattering in multi-planet systems and external dynamical interactions in dense star-forming environments.

In this chapter, I introduce the mechanisms through which stars and planets are thought to form. I then focus on their formation within relatively dense and substructured star-forming regions and discuss how these environments can affect the formation and evolution of the stars and planets within them.

In the following research chapters of this thesis, I investigate how we quantify the substructured nature of star-forming regions in order to understand the substructure and the effects that it can have on stars and planets. I then simulate the dynamical evolution of substructured star-forming regions and compare the outcomes for planets that undergo different types of dynamical interactions. I finish by analysing the destructive effects that photoevaporation can have on planet formation. I use this to add context to the results of simulations, which assume unhindered and instantaneous planet formation, where planetary orbits are then affected by dynamical interactions.

1.2 Star Formation

1.2.1 The Nebular Hypothesis

Our current understanding of how stars and planets form has its origins in the Nebular Hypothesis. The Nebular Hypothesis dates back to the 18th century, when Kant and Laplace proposed that the Solar System formed from a solar nebula that collapsed under its own gravity (Hetherington, 1997).

In the Nebular Hypothesis, the gaseous solar nebular forms a disk as it collapses, conserving angular momentum while minimising the system's potential energy. In practice, this is because the nebula would not initially have zero angular momentum and, as the nebula collapses, collisions between particles will tend to bring their motion in line with the average motion of the cloud. Over time, this leads to a disk forming, containing particles whose angular momenta point in approximately the same direction.

It is from this nebula that the central star forms, followed by its planets from the disk. However, many problems lie beyond this broad, general understanding of star formation because of the many physical processes involved (Krumholz, 2014). Therefore, star and planet formation remains a very active field of research.

1.2.2 Current Theories

The Shu et al. model

Modern theories of star formation begin with the Shu et al. (1987) model, which still influences our current understanding of the star formation process. In this model, star formation is a slow and essentially isolated process that can be divided into four stages, shown as panels *a*-*d* in Figure 1.1 (Shu, et al., 1987). First, slowly rotating cores form from the material in a molecular cloud (panel *a* of Figure 1.1). This happens as the support from magnetic field lines ‘leaks’ out of the cloud through ambipolar diffusion (Mestel & Spitzer, 1956), allowing the denser areas of material to collapse into cores under gravity. In molecular clouds, ambipolar diffusion is the process by which neutral particles decouple from the plasma and the support of the magnetic

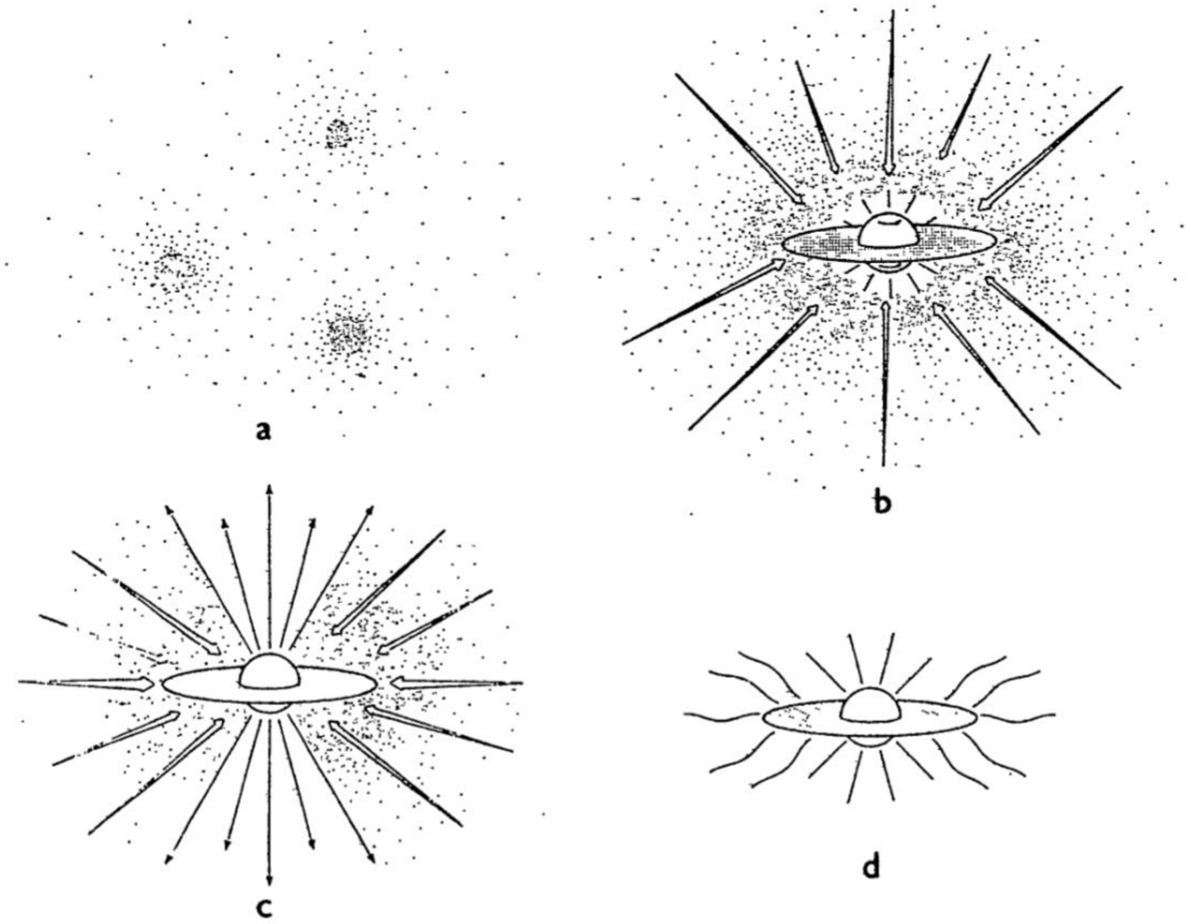

Figure 1.1 The four stages of the Shu et al. (1987) model of star formation: (a) Cores form within a molecular cloud; (b) ‘inside out’ collapse of a core produces an embedded, accreting inner protostar; (c) bi-polar outflows break through the envelope as the accretion rate reduces; (d) accretion stops, leaving a young, pre-main sequence object. Figure taken from Shu et al. (1987).

field. This happens when the ionisation fraction is low enough that interactions between neutral and ionised particles are rare, which allows the neutral hydrogen molecules to 'slip' through the magnetic field and undergo gravitational collapse. Second, when a core overcomes a density threshold, it begins an 'inside-out' collapse where the inner region collapses towards stellar densities (panel *b* of Figure 1.1). This leads to the formation of a heavily embedded central protostar, which is fed from its disk and the surrounding infalling material. In the third stage, the accretion rate slows. This reduces the pressure caused by the inward motion of material towards the star and disk, thereby allowing the outflows to break out (panel *c* of Figure 1.1). The outflows break out through the poles because these are the channels of least resistance, as material preferentially falls towards the disk rather than the star itself. In the final stage, material continues to fall increasingly onto the disk rather than the protostar, further reducing the inwards pressure on the protostar. This causes the opening angle of the outflows to widen, and the previously collimated bi-polar outflows become a stellar wind. The stellar wind overcomes the now reduced accretion, and leaves a young pre-main sequence stellar object that is surrounded by a disk (panel *d* of Figure 1.1).

However, there are problems with the Shu et al. (1987) model, including the long timescales required and the lack of primordial binaries. The Shu et al. (1987) model requires timescales of ~100 Myr, mainly because the process of ambipolar diffusion is relatively slow. However, observations found that most star-forming regions only contain stars that are ~1-10 Myr old (Hartmann, et al., 2001) and, by the 1980s, evidence of this was beginning to emerge (Herbig, et al., 1986). This is a problem for the Shu et al. model because, if star formation is slow, stars within star-forming regions would have a larger spread of ages (Elmegreen, 2000). Furthermore, observations of young star-forming regions, such as those in Taurus, which have nearly finished forming stars, found that they have a hierarchical spatial structure (Elmegreen, 2000). Interactions between stars and tidal interactions would have wiped out this spatial structure if more than a crossing time had passed since star formation began. Instead, the young stars appear to have formed fast enough that they have *"crystalized instantly"* (Elmegreen, 2000) out of their star-forming region and have therefore maintained its hierarchical structure. Observations of Taurus in particular (see references in Hartmann et al., 2001) then motivated research into faster star formation mechanisms. In these models, star formation happens within one or two crossing times – the average time that it would take for a star to traverse the star-forming region – rather than tens (Elmegreen, 2000; Hartmann, et al., 2001). Meanwhile, in terms of the production of primordial binaries, the Shu et al. (1987) model only allows stars to form individually, meaning that binary and multiple systems would have to form dynamically. However, the observed binary fraction is hard to achieve this way, especially for young pre-main sequence stars (Clarke, 1992; Clarke & Pringle, 1993).

“Star formation in a crossing time”

Although there are still many open questions (Krumholz, 2014), star formation is now seen as being primarily driven by turbulence and not significantly slowed by magnetic fields (McKee & Ostriker, 2007). This leads to star formation that is relatively fast (Elmegreen, 2000) and which naturally forms primordial binary and multiple systems (Duchêne & Kraus, 2013), therefore overcoming the problems with the Shu et al. model (Elmegreen, 2000; Hartmann, et al., 2001; Hartmann, 2003; McKee & Ostriker, 2007).

The current picture of star formation begins with the star-forming environment, with most stars appearing to form within filamentary structures in giant molecular clouds (Lada & Lada, 2003; Gieles, et al., 2012; André, et al., 2014). Giant molecular clouds are first assembled when mechanisms such as supernova shock fronts and the motion of the spiral arms create large-scale compressions in the diffuse interstellar medium (Elmegreen, 1991; Ballesteros-Paredes, et al., 2007; Dobbs, et al., 2014; Ballesteros-Paredes, et al., 2020). These compressions can produce giant molecular clouds that either undergo global collapse, or that are supported globally but still collapse on local scales (Ballesteros-Paredes, et al., 2007). In both cases, the giant molecular clouds are transient structures, with lifetimes of up to ~10 Myr (Hartmann, et al., 2001; Ballesteros-Paredes, et al., 2007; Dobbs, et al., 2014).

Within giant molecular clouds is a hierarchical hub-filament structure, where the filaments can be seen as conveyor belts that converge onto a central star-forming hub and feed it with gas as well as prestellar cores and protostars (Bate, 2009; Myers, 2009; André, et al., 2010; André, et al., 2014). These hub-filament structures are seen in all nine of the nearest stellar groups that

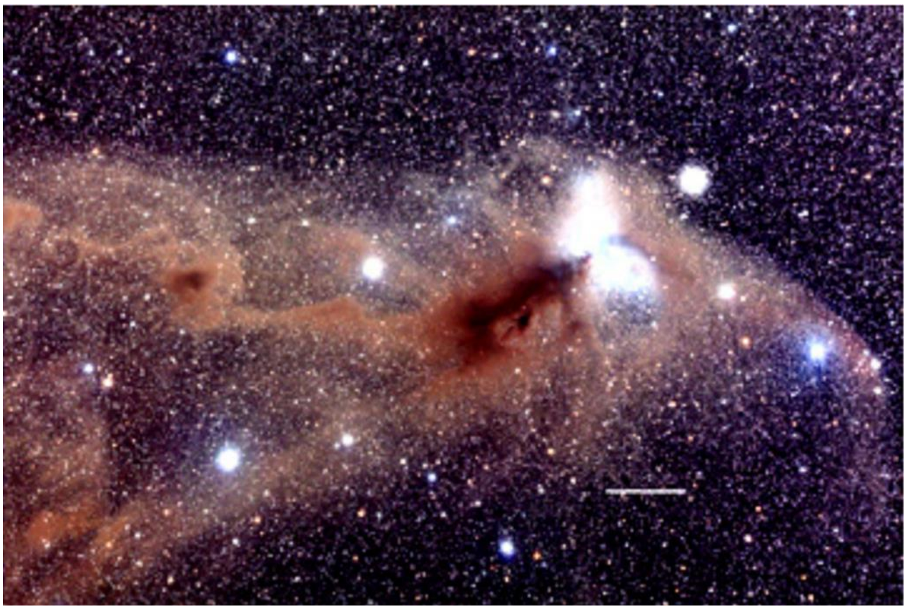

Figure 1.2 Optical image of Corona Australis, showing its hub-filament structure with 8 filaments. Scale bar is 1 pc. From Myers (2009), starryscapes.com.

are forming stars (Myers, 2009), including Corona Australis, which is shown in Figure 1.2. Filaments are ~0.1 pc (~10,000 AU) wide (Arzoumanian, et al., 2011; André, et al., 2014), and parsec scale in length (Bate, 2009). This means that one giant molecular cloud can contain multiple hub-filament structures.

Myers (2009) suggest that hub-filament structures are caused by the large-scale compression of the clumpy gas that giant molecular clouds form from. This leads to a less dense outer layer which forms filaments, and a denser inner clump which can quickly collapse and form stars with a high local efficiency (Myers, 2009; Peretto, et al., 2012). For example, in hydrodynamical simulations, Bate (2009) found a local star formation efficiency of ~40%. In this model of hub-filament formation, it is the initially clumpy nature of the gas that leads to the formation of the central hubs (Myers, 2009). If the initial gas was uniform, the compression would only cause the formation of filaments, and not hubs.

The densest parts of filaments form pre-stellar cores, which are collapsing, dense regions of gas (McKee & Ostriker, 2007). Evidence for star formation beginning within filaments includes observations of the Aquila star-forming complex, where $> 60\%$ of the bound pre-stellar cores and some of the protostars are found in supercritical, gravitationally unstable filaments, which are prone to collapsing radially (André, et al., 2010; Ballesteros-Paredes, et al., 2020). Meanwhile, pre-stellar cores are not found in subcritical filaments, both in active star-forming regions and regions that are not yet forming stars, such as Polaris (André, et al., 2010; Miville-Deschênes, et al., 2010; André, et al., 2014). This implies that the formation of filaments precedes star formation (André, et al., 2014). There are, however, some observed star-forming regions where star formation appears to only occur within the central hub, such as the B59 hub in the Pipe Nebula (Peretto, et al., 2012). In this way both the filaments and hubs are an active component of the star formation process (André, et al., 2014).

Physically, the formation of prestellar cores happens when the pressure within a filament or hub is unable to support it against gravitational collapse, meaning that it is Jeans-unstable and prone to collapse and fragmentation (Ward-Thompson & Whitworth, 2011). The condition for collapse can also be understood in terms of the Jeans mass, Equation 1.1, and the Jeans length, Equation

1.2 (Jeans, 1902). In these equations c_s is the sound speed, which depends on the thermal energy, and ρ is the density of the potentially collapsing region. A region may gravitationally collapse into a core and condense out of its filament if it has a size greater than the Jeans length, or a mass greater than the Jeans mass (Ward-Thompson & Whitworth, 2011). Because of the dependence on the sound speed and density, the Jeans mass and length can change over time and during the collapse itself. The core must therefore maintain these conditions throughout the collapse, or the collapse will not continue.

$$M_\mathrm{J} = \frac{4\pi c_\mathrm{s}^3}{3\mathrm{G}^{3/2}\rho^{1/2}} \tag{1.1}$$

$$R_\mathrm{J} = \sqrt{\frac{c_\mathrm{s}^2}{\mathrm{G}\rho}} \tag{1.2}$$

Protoplanetary disks begin to form almost immediately when a core collapses (Williams & Cieza, 2011). In terms of the pre-stellar core itself, the mass and size of cores that form are determined by the Jeans mass and length. This leads to typical masses of ~1 $\mathrm{M}_\odot$, with a distribution of masses that appears to be similar to the IMF (Offner, et al., 2014), and a size of ~0.1 pc.

The typical temperature of a core is ~10 K (Ward-Thompson & Whitworth, 2011). The initial collapse is isothermal because the core is optically thin to radiation, and the dust is therefore able to radiate away the increased thermal energy from the collapse (McKee & Ostriker, 2007). While the temperature remains at ~10 K, the sound speed is also constant. However, the density continues to increase during the collapse. This means that the Jeans mass decreases.

As the density of the core increases it becomes sufficiently opaque that it is optically thick to its own radiation, and can no longer continue to radiate the increased thermal energy efficiently enough for the collapse to remain isothermal (Ward-Thompson & Whitworth, 2011). The collapse then becomes adiabatic, where no heat is lost to the surroundings, and it is instead contained within the core. The increase in temperature that this causes means that the sound speed, which is dependent on the kinetic energy in the core, begins to increase. For the Jeans mass, shown in Equation 1.1, the sound speed term in the numerator dominates over the increasing density term in the denominator because it goes as c_s^3. The Jeans mass therefore begins to increase.

During the core collapse, there is therefore a minimum value of the Jeans mass, since it decreases while the collapse is isothermal, and then increases while the collapse is adiabatic. This minimum mass is ~10^{-2} $M_{\odot}$, or ~10 Jupiter masses, and occurs at a density of ~10^{-13} g cm^{-3}. This is the opacity limit for fragmentation, and it is at this point when fragmentation is most likely to occur. At this stage, the increased energy allows the first hydrostatic cores to form, which have sizes of a few AU and slowly contract (Ward-Thompson & Whitworth, 2011).

There is then a rapid second collapse once the core has contracted enough to reach a temperature of ~2000 K (McKee & Ostriker, 2007). This is because, at these temperatures, the contraction becomes nearly isothermal again as most of the increase in energy is absorbed by disassociating H_2, which acts as a heat sink. This causes a second minima of the Jeans mass, inducing a rapid second collapse to densities approaching that of a star, thereby forming a protostar (McKee & Ostriker, 2007). There can be one or more protostars per core, as a core can fragment into multiple objects which may form a binary or multiple system (McKee & Ostriker, 2007; Chen, et al., 2013; Pineda, et al., 2015).

Until the protostar reaches the main sequence, when nuclear fusion begins, it only produces energy through its slow contraction and inability to efficiently radiate away the energy produced from this (Ward-Thompson & Whitworth, 2011). During this time the protostar rapidly accretes mass from its envelope.

The protostar phase of a young star's evolution spans the Class 0 and Class I observational stages for low mass star formation. Each class corresponds to a distinct phase in the spectral energy distributions, and together they are thought to form an evolutionary sequence (Lada, 1987; Andre, et al., 1993; McKee & Ostriker, 2007). Class 0 sources, proposed by Andre et al. (1993), appear as a cold black body and this earliest stage appears to last for ~0.01 Myr. This is an embedded phase where the mass of the envelope is larger than, or comparable to, the mass of the star. It is, therefore, during this phase that protostars accrete a significant amount, or the majority, of their final mass (McKee & Ostriker, 2007). Classes I to III were introduced by Lada

(1987). Class I sources are evolved protostars with ages of ~0.1 Myr (McKee & Ostriker, 2007). They have a large infrared excess on top of their black body spectrum, as shown in the first panel of Figure 1.3 (Lada, 1987). This is dominated by the surrounding envelope and caused by dust particles absorbing and re-emitting radiation at redder wavelengths.

Once the material surrounding the protostar has either been accreted or dispersed, the protostars become pre-main sequence stars (Ward-Thompson & Whitworth, 2011). Young pre-main sequence stars observationally correspond to Class II sources/ classical T Tauri stars (McKee & Ostriker, 2007). These are stars that are still accreting and have a significant disk but no envelope (McKee & Ostriker, 2007). The shape of the spectral energy distribution for Class II sources is shown in the second panel of Figure 1.3 (Lada, 1987), where the infrared excess is now caused by the disk.

The Class II/ classical T Tauri star is then thought to evolve into a Class III/ weak-lined T Tauri star, once its accretion rate slows significantly (McKee & Ostriker, 2007). These stars are now near the zero-age main sequence and no longer have a significant infrared excess caused by a disk, as shown in panel 3 of Figure 1.3 (Lada, 1987).

Massive Star Formation

Two main mechanisms have been proposed for the formation of massive stars, with masses greater than 8 $M_\odot$ (Tan, et al., 2014): monolithic collapse and competitive accretion.

The monolithic collapse model sees high mass stars form in a similar way as low mass stars, as previously described, only scaled to higher masses (Zinnecker & Yorke, 2007). In this model the core would have to be kept warm in order to increase the Jeans mass. This would prevent the core from fragmenting into more than one protostar, leaving more mass available to form a single massive star.

In the competitive accretion model (Bonnell, et al., 1997; Bonnell, et al., 2001), all stars form with a similar initial mass that is determined by the Jeans mass. However, stars that happen to form in a more gas-rich region are able to accrete more mass. This then leads to runaway growth

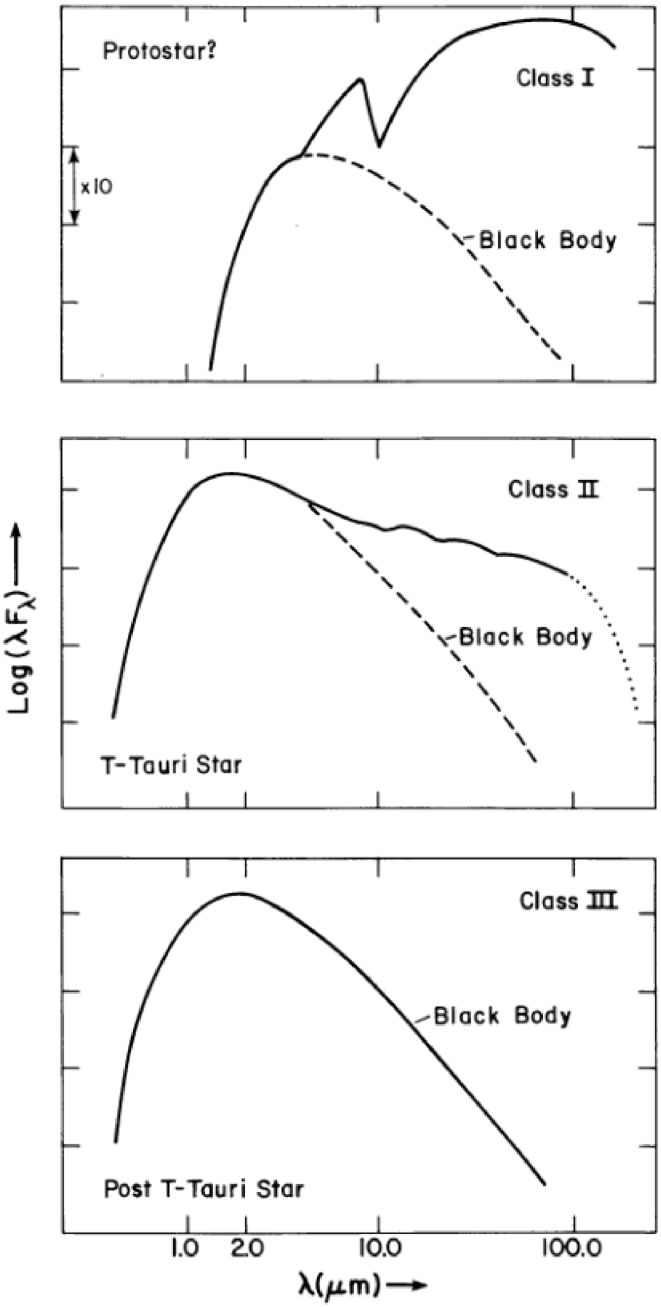

Figure 1.3 Spectral energy distributions for stellar evolution classes I to III. The black body component is labelled, and additional contributions to the infrared portion of the distributions are shown. Taken from Lada (1987).

as the more massive stars begin to dominate their local gravity potential, and an increasing proportion of the gas is funnelled onto them as they 'compete' against nearby lower mass stars.

It may also be possible for massive stars to form through collisions and mergers. These mergers can be of stars that directly collide (Bonnell, et al., 1998), or of the collision of stars within a close binary system that has been perturbed by an encounter with another star (Bonnell & Bate, 2005). Both scenarios require high densities and would be expected to only occur in the densest areas of a star-forming region or young cluster. Therefore, this mechanism is less favoured (Tan, et al., 2014).

1.2.3 Properties of Stars

Mass

The masses of stars range from M-dwarfs that are just massive enough to burn hydrogen, above the 0.08 $M_\odot$ brown dwarf mass limit, to those that are hundreds of solar masses (Crowther, et al., 2010). The initial mass function is the probability function of the mass distribution of stars once they have formed. It also includes brown dwarfs, with masses below 0.08 $M_\odot$. The form and potential universality of the initial mass function has far-reaching effects (Offner, et al., 2014). For example, it places important observational constraints on theories of star and planet formation.

The origin of the initial mass function is highly debated (Offner, et al., 2014). On the one hand, it is argued that the initial mass function is pre-determined and inherited from the core mass function (Alves, et al., 2007). Evidence for this includes the similarities between the core and initial mass functions. There has also been recent research into the filament mass function and the extent to which this may determine both the core and initial mass functions. André et al. (2019) suggest that the initial mass function is *"at least partly inherited"* from the filament mass function due to similarities in their form. In this view, the filament mass function is determined by the effects of the characteristic compression, turbulence, and accretion that causes filaments to form and gain mass from the molecular cloud. The filament mass function that is produced is characteristic and distinct from that of other bound material and clumps, and is then inherited by the cores followed by the stars that form within them.

On the other hand, it is argued that similarities between the mass distributions of cores and young stars are coincidental in that it is not possible for the core mass function to directly fragment into the observed initial mass function without other processes shaping it (Clark, et al., 2007; Offner, et al., 2014). Instead, in this view, the form of the initial mass function is primarily determined by dynamical effects such as competitive accretion.

Many functional forms of the initial mass function have been proposed. The first was developed by Salpeter (1955) by observing the luminosity function of stars in the solar neighbourhood. Five parameterisations, including the Salpeter initial mass function, are shown in Figure 1.4 (Offner, et al., 2014). In general, models of the initial mass function include a high mass slope, where the probability of higher mass stars becomes increasingly low, and a low mass turnover which causes the functional form to peak at lower masses between ~0.1-0.5 $M_\odot$.

It is debated whether the maximum potential mass of a star depends on the mass of its star-forming region, or whether stellar masses within a given region are consistent with having been sampled from a universal initial mass function. Weidner & Kroupa (2006) argue that the maximum stellar mass does correlate with the mass of its cluster, in such a way that only the most massive star-forming regions would produce very massive stars. However, other studies find that observations are consistent with a random sampling of the IMF (Maschberger & Clarke, 2008), and there are clear examples of low mass regions which contain massive stars (Parker & Goodwin, 2007). For example, the cluster γ Velorum has a mass of ~100 $M_\odot$, yet contains the γ^2 Velorum binary system whose components likely both had initial masses of over 20 $M_\odot$ (Eldridge, 2009).

Binary Fraction

Cores often fragment into multiple objects which may remain bound gravitationally and lead to a binary, or higher order, multiple star system (Chen, et al., 2013; Pineda, et al., 2015). The frequency of binary and multiple stellar systems, grouped by stellar mass, is summarised in

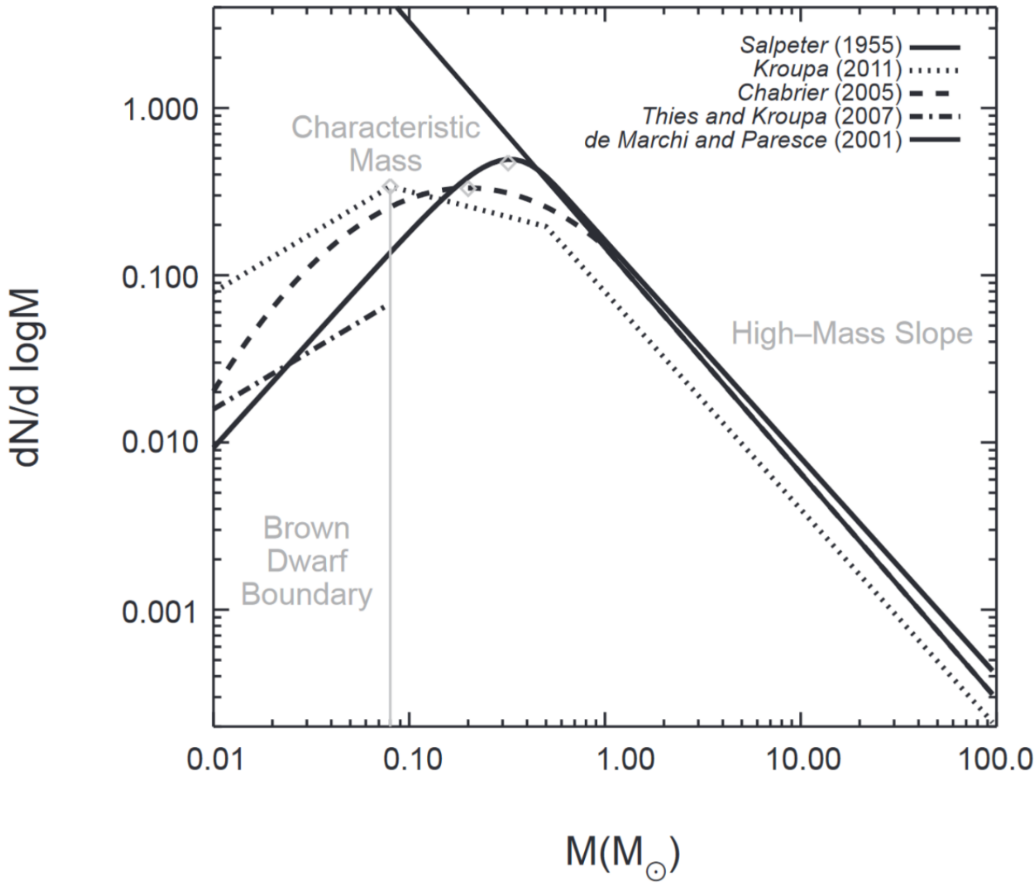

Figure 1.4 A comparison of five functional forms of the initial mass function. Taken from Offner et al. (2014).

Figure 1.5 (Duchêne & Kraus, 2013). The multiplicity fraction (how many stellar systems are multiples) is shown in blue, and the companion fraction (the average number of companions per star) is shown in red. Figure 1.5 shows that the majority of high mass stars are part of a multiple system, while the majority of low mass stars are single.

The formation of binary and multiple systems naturally follows from the star formation process, and the initial binary fraction distribution may be universal (Duchêne & Kraus, 2013). The properties of binary and multiple systems are therefore useful for constraining star formation theories.

However, it is also possible for multiple systems to form and be destroyed dynamically. For example, the multiplicity fraction is observed to be lower in denser regions where destructive dynamical interactions are more common and can reduce the binary fraction by a factor of 2 to 4 (Kroupa, 1995a; Kroupa, 1995b; Parker, et al., 2011; Duchêne & Kraus, 2013). Destruction by dynamical interactions preferentially affects wider separation binaries which are more loosely bound (Kroupa & Petr-Gotzens, 2011).

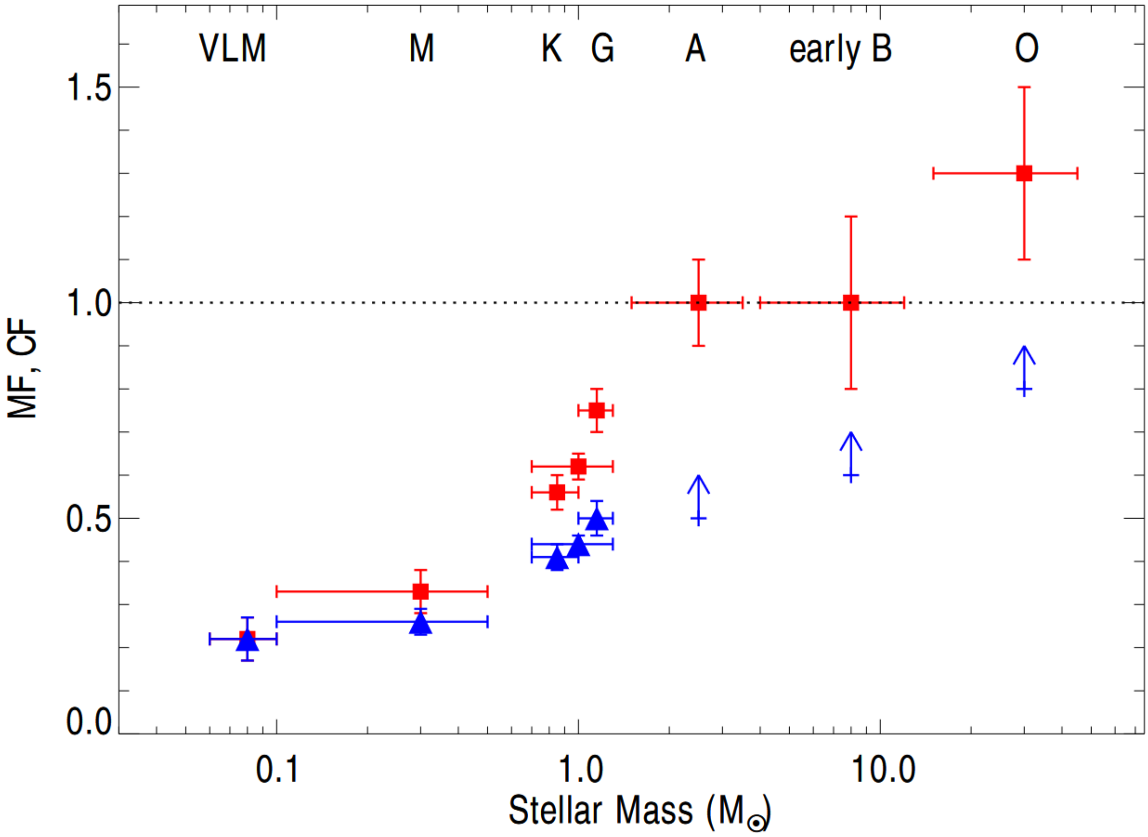

Figure 1.5 The observed multiplicity fraction (MF, shown in blue) and companion fraction (CF, shown in red) for a range of stellar masses. The VLM data point is for Very Low Mass objects i.e. sub-stellar brown dwarfs. Taken from (Duchêne & Kraus, 2013).

1.3 Planet Formation

1.3.1 Protoplanetary Disks

That planets form within the disks around young stars has been confirmed by observations (e.g. Quanz et al., 2015; Keppler et al., 2018), and the universality of planet formation and circumstellar disks means that they are usually described as protoplanetary disks (Venturini, et al., 2020), rather than accretion disks as they were often previously known. Protoplanetary disks supply the reservoir of material needed for both star and planet formation, and it is through these disks of gas and dust that the processes of star and planet formation are linked (Li, et al., 2014).

Protoplanetary disks are rotating disks of cool gas and dust that extend from 10's to 100's of AU from the central star (Williams & Cieza, 2011; Andrews, 2020). Observations have found that larger disks extend out to ~100-500 AU from their central star, and that the dust component extends around half this distance, while smaller disks extend out only tens of AU[1] (Ansdell, et al., 2018; Andrews, 2020; Hendler, et al., 2020). Within this radius, protoplanetary disks contain a mass of around ~1% of the central stellar mass (Andrews & Williams, 2007; Andrews, et al., 2013). However, there are large variations within this, and mass estimates are currently uncertain. This is due to the reliance on tracers to calculate the total disk mass, and that significant mass can be 'hidden' within pebbles that are larger than centimetre-sized and therefore do not emit detectable infrared radiation (Williams & Cieza, 2011; Venturini, et al., 2020). Furthermore, if planet formation has already significantly progressed once the star is observable and no longer embedded, it is possible that we are measuring the mass of already depleted disks (Greaves & Rice, 2010; Andrews, 2020). Across the protoplanetary disk, the mass decreases approximately inversely with radius, and the edge is tapered approximately exponentially (Williams & Cieza, 2011).

---

[1] It is expected that the lower limits on disk sizes that have been found in surveys are due to resolution limits, rather than physically motivated lower limits in the disk sizes themselves (Andrews, 2020).

There have been rapid developments in our understanding of protoplanetary disks in the last decade, largely due to observations with ALMA. Although dust only accounts for ~1% of the material in a protoplanetary disk, the dust is easier to observe than the gas (Andrews, 2020). Therefore, observations of protoplanetary disks detect the dust in the disk through infrared and millimetre observations (Williams & Cieza, 2011).

ALMA observations have provided new insight into the morphology of protoplanetary disks. Figure 1.6 shows images of 20 protoplanetary disks taken with DSHARP/ALMA and illustrates some of the morphologies that have been observed. These morphologies include ring-gap, spiral, and arc structures which may either be indicative of planet formation and/or migration within the disk, or a signature of the fluid mechanics within the disk (Andrews, 2020). In particular, the gaps in ring-gap structures may have been carved out by planets that have accreted the material within the gap's anulus (Lodato, et al., 2019; Pinte, et al., 2020). One example of this is the planet PDS 70b, which can be seen orbiting at a distance of 22 AU inside a gap in its protoplanetary disk in Figure 1.7 (Keppler, et al., 2018). This is seen as evidence that the gaps in at least some protoplanetary disks have been carved out by planets (Andrews, 2020). However, it is also possible for other processes to produce ring-gap structures in protoplanetary disks. For example, the position of some snow lines (e.g. that of CO) can evolve 10's of AU on 1,000 and 10,000 year timescales, a process which can create gaps within the disk (Owen, 2020).

Once a protoplanetary disk has evolved, and the gas is mostly depleted, it transitions to become a debris disk (Hughes, et al., 2018). This depletion can happen due to a range of processes. These include external and internal photoevaporation, truncation by a binary companion or passing star, and the material simply being used up in planet formation (Williams & Cieza, 2011).

Disks around young stars retain a dust component (Fedele, et al., 2010; Richert, et al., 2018), and so debris disks consist of dust and solid objects in a range of sizes (Hughes, et al., 2018). The dust in these disks may then be continuously replenished by cascades of collisions between the solid objects, where the remnants of larger collisions continue to collide and break into smaller and smaller components (Pan & Schlichting, 2012). This has the potential to replenish

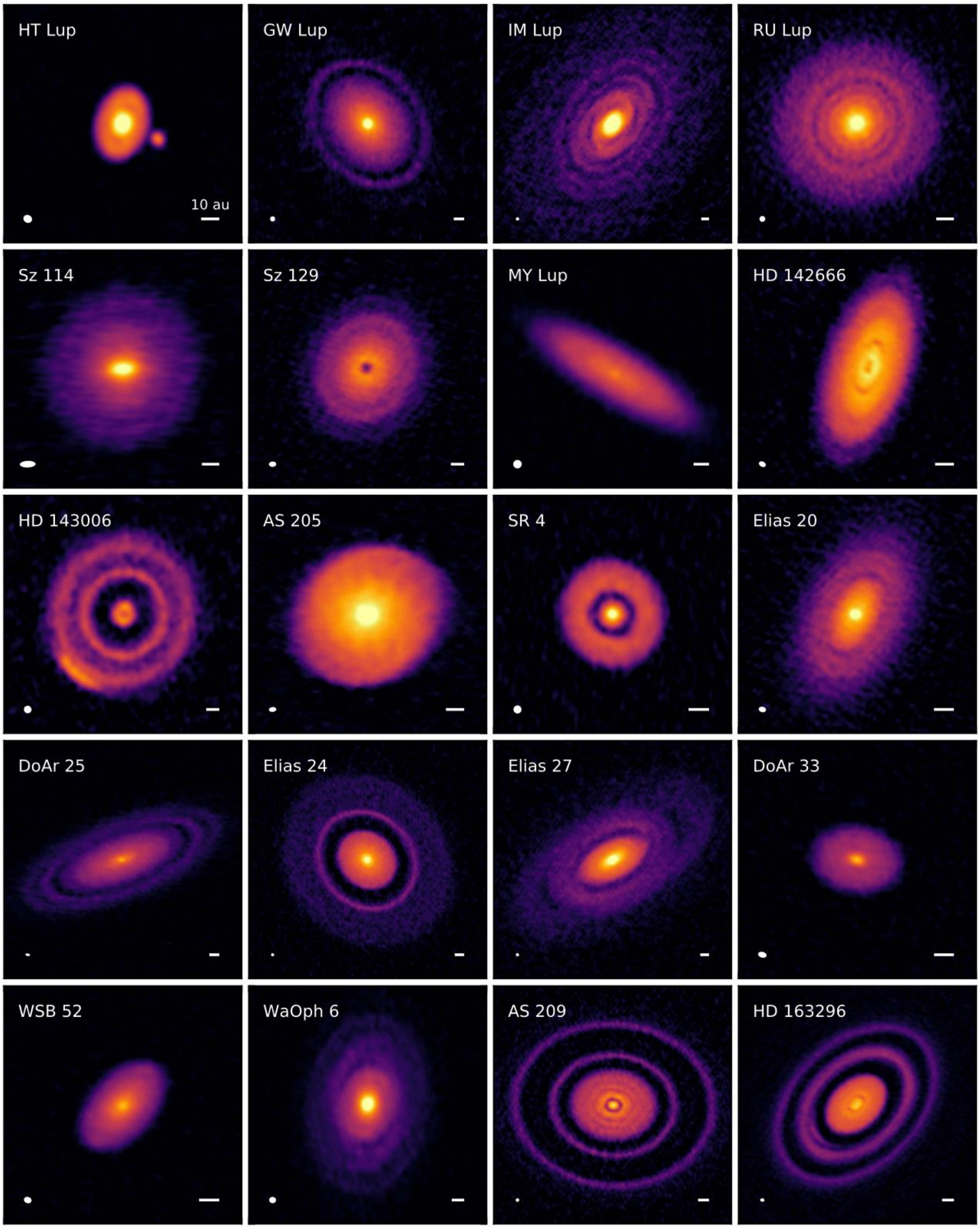

Figure 1.6 Images of 20 protoplanetary disks, taken using DSHARP at 1.25 mm. The scale bars are 10 AU, and the FWHM beam size, which is representative of the resolution, is shown in the lower left corner of each image. The array of images shows some of the wide range of disk morphologies that have been observed. Taken from: Andrews et al. (2018), ALMA, DSHARP.

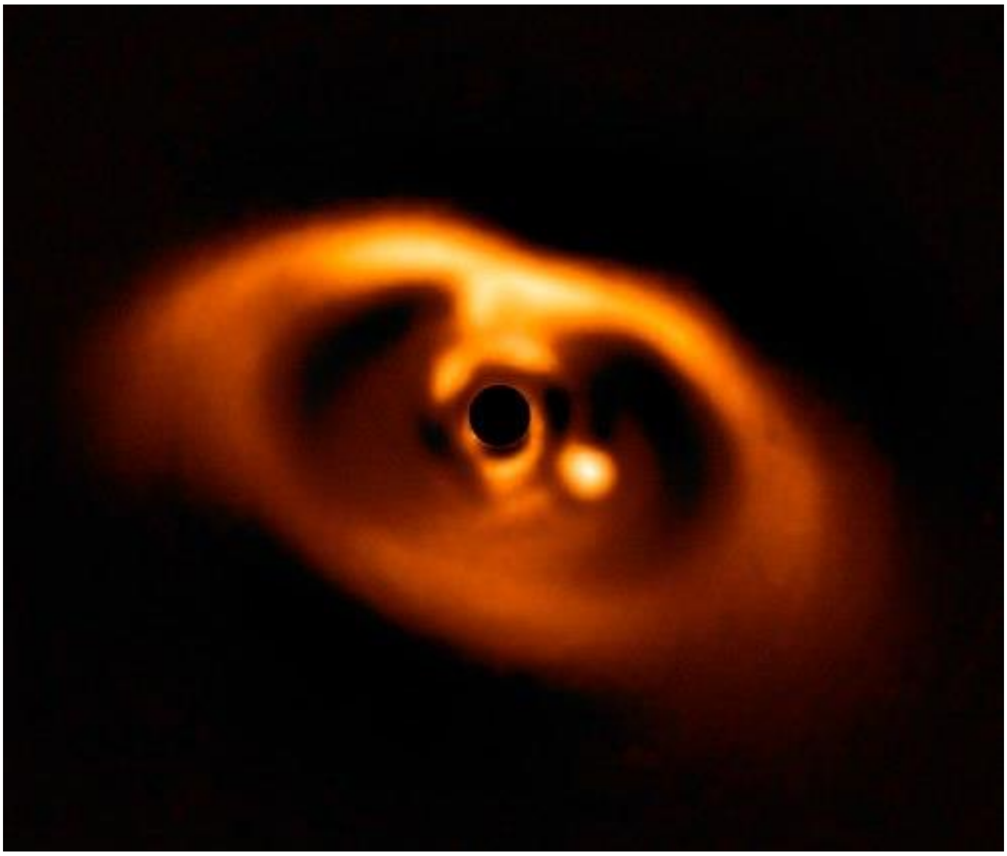

Figure 1.7 ALMA image of the protoplanetary disk around the star PDS 70, with the protoplanet PDS 70b visible towards the right of the central star within a gap in the disk. Credit: ALMA.

the disk for the duration of the star's lifetime, with debris disks around main sequence stars being similar to the Kuiper Belt in our Solar System (Hughes, et al., 2018).

1.3.2 Current Theories

The process of planet formation is likely to be fast and begin even while the protostar and protoplanetary disk itself are still forming and heavily embedded (Nixon, et al., 2018; Andrews, 2020). This means that planet formation has not been observed from start to finish and our understanding is relatively theoretical, where observations are used to constrain these theories. Here, I discuss three possible planet formation mechanisms: core accretion (Pollack, et al., 1996), disk instability (Boss, 1997), and core instability, where core accretion and disk instability are the dominant two theories.

Core Accretion

Core accretion is currently the leading theory for how most planets form. Core accretion begins with the dust in the protoplanetary disk settling further into the potential than the gas component, as it is not supported by gas pressure. This causes the formation of a thinner, dustier region where collisions between dust particles are more frequent. In this region, dust grains coagulate (i.e. stick together) as they collide. Initially, this leads to the formation of small pebbles which have sizes of the order of centimetres and meters.

Over time, km-sized planetesimals are formed (Venturini, et al., 2020). This can happen through runaway growth followed by oligarchic growth (Raymond, et al., 2014). In runaway growth, the pebbles are large enough that their size leads to an increased frequency of collisions, compared to the collision of two dust grains. Pebbles continue to grow in this way until the gravitational pull of a small minority of larger bodies begins to dominate and they are large enough to decouple from the disk, where previously they would have been kept on the disks Keplerian orbits by drag forces. It is at this point where gravitational focussing begins to have a significant effect and the growth becomes oligarchic. In this way, "the rich get richer" and the most massive bodies sweep up an increasing amount of the material in the anulus of their orbit, including other larger objects. This allows them to reach the size of planetesimals.

However, it is also possible that planetesimals may for from early instabilities in the disk. Nixon et al. (2018) find that the transient, gaseous spiral arms that naturally occur within young self-gravitating disks can act as dust traps. The collected dust may then fragment and produce planetesimals of sizes of the order of meters and larger. This process would allow planet formation to occur *"vigorously and early"* (Nixon, et al., 2018) during the Class 0 and I phases. An implication of this view is therefore that even the youngest observable protplanetary disks will contain planetesimals and planets.

Once a planetesimal grows to roughly the mass of Mars, its future mass depends on its distance from the host star, in particular, whether it is within or beyond the snow line (Bodenheimer & Pollack, 1986; Helled, et al., 2014; Venturini, et al., 2020). Within the snow line there are no ices for the planetesimals to accrete. These planetesimals therefore become smaller terrestrial planets. However, beyond the snow line, ice molecules can form and tend to coat dust particles. This means that a planetesimal which is beyond the snow line can accrete water ice and other solid volatiles, and therefore grow to higher masses. If a planet reaches ~10 Earth masses, and is close enough to the star that the gas density in the disk is high enough, it can also accrete a significant amount of gas. This happens through a runaway accretion, where the mass of the gaseous envelope grows faster than that of the solid core. These planets are gas giants. However, if a giant planet is at larger distances where the gas density of the disk is low, there is not enough available gas for it to become a gas giant. Instead, it will only be able to accrete frozen volatiles. These planets are, therefore, ice giants.

Planet formation by core accretion is thought to take up to ~3 Myr in total, where this is the total time for a planet to begin forming and then complete the stages of coagulation, runaway growth, and oligarchic growth (Helled, et al., 2014; Raymond, et al., 2014). The time taken for pebbles to form through the coagulation of dust grains is dependent on the collisional timescale, t_{coll}, given in Equation 1.3:

$$t_{\mathrm{coll}} = \frac{1}{\pi r^2 n \sigma} \tag{1.3}$$

where, r is the radius, n is the number density of the dust particles, and σ is the velocity dispersion. At a disk radius of 1 AU, this leads to timescales of ~0.3 Myr for a cm-sized pebble to form. At larger radii, the number density is lower, and the time for a pebble to form at 5 AU would increase to ~3 Myr. However, instabilities within the disk may increase the local number density, allowing pebbles to coagulate more rapidly.

Runaway growth to km-sized objects then occurs very rapidly, as the pebbles decouple from the disk. This stage does not add significantly to the timescale of planet formation. Planets that form through core accretion then continue to grow through the oligarchic growth phase for $\lesssim$0.1 Myr, as determined by:

$$M \sim \pi r^2 \Theta \sigma n m \qquad 1.4$$

where M is the accretion rate of the planetesimal, Θ is the Safranov number, which is a measure of gravitational focussing, and nm is the mass density of the disk.

The accretion of material onto a planet then stops either when a gap forms in the anulus of the disk where the planet orbits, or when the disk is otherwise depleted.

The current positions of the planet mean that Solar System appears to be well explained by the core accretion model (Helled, et al., 2014). The less massive, terrestrial planets are close to the Sun. And, beyond the ice line are the gas giant planets, which could accrete ices and gases, followed by the ice giant planets which could only accrete ices. Core accretion can also explain many of the properties that have been observed in the exoplanet population (Helled, et al., 2014) such as the observed low abundance of exoplanets orbiting low mass, solar metallicity, stars. For example, Johnson et al. (2010) find that 3% of solar metalicity 0.5 $M_\odot$ stars have giant planets, and that this rises to 14% for 2 $M_\odot$ stars. This is consistent with the core accretion model, as simulations reproduce such a correlation, but is in contrast to the disk instability model, discussed in the following subsection, which predicts that giant planets can form in low mass disks at frequencies that are not dependant on stellar properties and disk metallicity (Johnson, et al., 2010). However, the properties of some exoplanets pose problems for the core accretion model. For example, giant exoplanets have been observed on orbits beyond ~20 AU where there should not have been enough disk material for them to form through core accretion (Helled, et al., 2014).

Disk Instability

In the disk instability model of planet formation (Boss, 1997), there are gravitational instabilities in the protoplanetary disk. This causes the formation of over-densities and bound 'clumps' which may then fragment. This is somewhat similar to the core fragmentation mechanism by which stars form. However, because conditions within a protoplanetary disk are different to those in a pre-stellar core, there are different conditions for the fragmentation. This means that planet-mass objects can form this way, rather than being limited by the opacity limit for fragmentation, which sets the minimum mass of an object formed through core fragmentation at ~10 M_{Jup}.

The condition for fragmentation within a protoplanetary disk is set by the Toomre stability criterion (Toomre, 1964). This depends on the star-to-disk mass ratio, and the disk's aspect ratio, which is the ratio between the isothermal scale height and the disk radius. The isothermal scale height, H, is the sound speed divided by the Keplerian angular frequency, as shown in 1.5:

$$H = \frac{c_s}{\sqrt{\frac{GM}{R^3}}} \qquad 1.5$$

Where M is the mass of the star, and R is the mass of the disk.

Fragmentation can occur when the aspect ratio is less than the star-to-disk mass ratio, and these conditions can be met very early in the evolution of the protoplanetary disk, while it is still heavily embedded (Helled, et al., 2014).

However, the proportion of protoplanetary disks that meet the conditions for fragmentation is unclear, and it is expected that only a small amount of planets form this way (Helled, et al., 2014). Reasons for this include that the disk must be young and still massive enough for regions to be gravitationally unstable, yet the disk must have already cooled significantly in order for the formation of bound clumps by fragmentation to be possible (Rafikov, 2005; Kratter, et al., 2010).

It is especially unlikely that these conditions could be met within the inner regions of the disk. Past simulations have found that fragmentation can occur as close in as ~10 AU (Mayer, et al., 2002). However, recent simulations, with more accurate equations of state than those used previously find that the conditions for fragmentation are only generally met at distances ≳80 AU (Meru, 2015). Meru (2015) does find that fragmentation can occur at smaller distances of ≲50 AU if an initial fragmentation triggers spiral density waves with densities large enough to fragment. Disk fragmentation therefore tends to form giant planets at large distances from the star. Planets with these properties can be observed through direct detection, such as the HR 8799 planetary system which has three giant planets orbiting at 24, 38, and 68 AU (Marois, et al., 2008).

Disk fragmentation is more common in the very early embedded stages of the protoplanetary disk, including the Class 0 phase, and planets can form through this mechanism in ~few 10^5 years (Durisen, et al., 2007; Helled, et al., 2014).

The core accretion and disk instability models are generally seen as complementary, partly due to the different timescales over which they would be expected to occur and the different masses of planets that they would be expected to produce (Helled, et al., 2014). Disk fragmentation would be expected to produce the highest mass giant planets, whereas core accretion tends to produce the terrestrial and low-mass giant planets.

Core Fragmentation

It may also be possible for planets to form in the same way as stars – through the fragmentation of a core due to gravitational instabilities (Chabrier, et al., 2014). As already discussed, the opacity limit for fragmentation sets the minimum mass of an object that can form this way at ~10 M_{Jup}. This means that objects that have formed this way are massive, free-floating and more ‘star-like’ than ‘planet-like’ in terms of their formation mechanism. It is therefore argued that these objects should be considered to be brown dwarfs rather than planets (Chabrier, et al., 2014).

However, it can also be argued that it is more appropriate to distinguish giant planets from brown dwarfs based on their mass (Chabrier, et al., 2014): where giant planets have masses $<13\ M_{Jup}$, and are therefore unable to sustain deuterium burning, unlike brown dwarfs with masses $>13\ M_{Jup}$. This is the official International Astronomical Union definition and removes the overlap in mass that is present when distinguishing giant planets and brown dwarfs based on their formation mechanism.

1.3.3 Timescale

Regardless of the planet formation mechanism, there are observational constraints placed on how long the process can take, and at what stages of star formation it is possible for planets to form. Over time, the circumstellar material from which planets form is depleted from the disk (Williams & Cieza, 2011). This can happen due to the photoevaporation from both the central and nearby massive stars, dynamical interactions with a binary companion or passing objects, and the processes of star planet formation themselves (Clarke, 2011). These disk destruction mechanisms are discussed further in Section 1.5, and investigated in Chapter 5.

Because disk material must be present for planets to form, the measured lifetime of protoplanetary disks provides an upper limit for the timescale of planet formation (Haisch, et al., 2001a; Richert, et al., 2018). Measurement of disk lifetimes are therefore an important and relevant tool for studying planet formation. This is the case both for planet formation in general, as well as when studying the formation of terrestrial and Jovian planets separately, as the gas and dust lifetimes of the disk provide constraints for each of these (Richert, et al., 2018).

In a seminal study, Haisch et al. (2001) investigated this by observing star-forming regions with ages of 0.3-30 Myr, measuring the fraction of stars that have dusty circumstellar disks within radii of $\lesssim 0.1$ AU from the star. They do this by searching for L-band infrared excess which is indicative of the dust in the hottest (900 K) regions of the disk which are the most heated by the central star. Observations that detect mm emission, which is sensitive to dust out to tens of AU, have found that stars with disks at $\lesssim 0.1$ AU also tend to have outer disks, beyond 1 AU, and that inner and outer disks tend to disappear on the similar timescales (Williams & Cieza, 2011). The results from Haisch et al. (2001) and subsequent studies therefore likely apply to

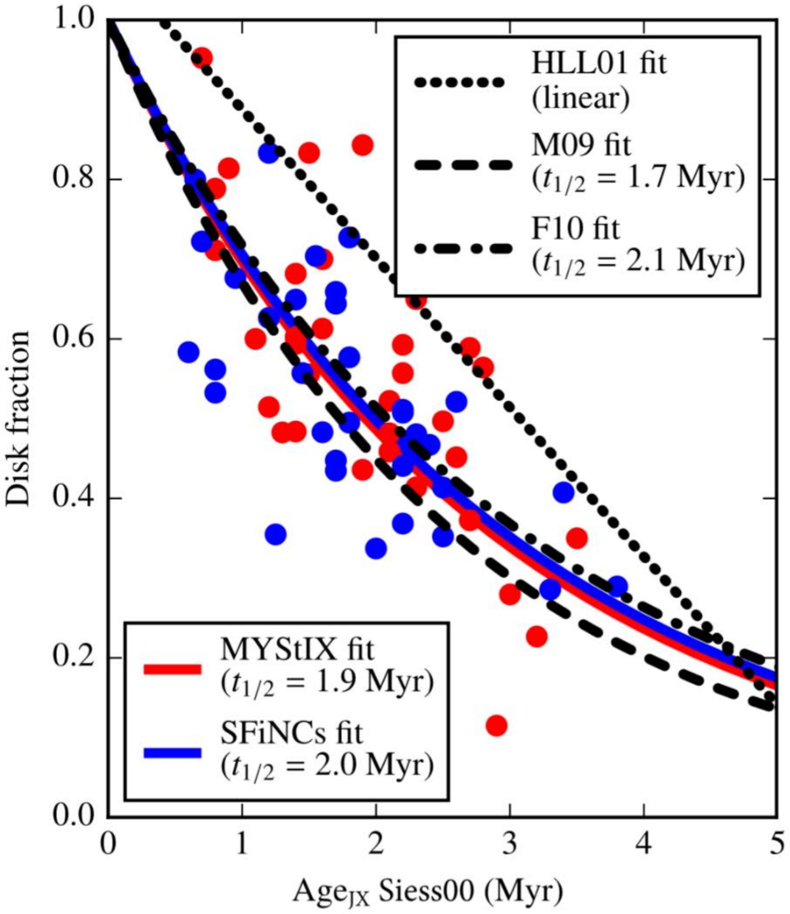

Figure 1.8 A comparison of disk fraction with stellar age. Obervations of disks from the MYStIX (MYStIX, Feigelson et al. 2013) and SFiNCs (SFiNCs, Getman et al. 2017) projects are shown as red and blue points, respectively. Richert et al. (2018) fit my MYStiX and SFiNCs data separately, showsn by the red and blue lines. Results from three previous studies are shown as black dotted lines. Taken from Richert et al. (2018).

circumstellar disks as a whole and not just the measured inner regions. (Haisch, et al., 2001a; Haisch, et al., 2001b; Williams & Cieza, 2011; Richert, et al., 2018).

Haisch et al. (2001) found that almost all very young, <1 Myr old stars have disks. However, by ~3 Myr half of stars do not have a disk, and almost no stars older than ~5 Myr have disks. This therefore implies that the upper limit to the timescale for planet formation is ~5 Myr and that planet formation must begin within less than 0.1-1 Myr of star formation, so that they have time to form (Concha-Ramírez, et al., 2019).

These oberations have since been expanded upon, and recent studies find consistent results (Williams & Cieza, 2011). Observations sensitive to dust out to ~5 AU have found that only ~20% of stars have disks in clusters with ages of ~5 Myr, and that less than 5% are able to retain their disks up to ages of ~8 – 10 Myr (Williams & Cieza, 2011). For example, Richert et al. (2018) use observations of 69 young clusters in 32 star-forming regions, with ages less than ~5 Myr. They find that the choice of pre-main sequence evolutionary model that is used to estimate the stellar ages can cause the results to vary significantly[2], as they obtain disk half lives of ~1.3-2 Myr and ~3 Myr for different evolutionary models. However, their results are consistent with previous work, as summarised in Figure 1.8, which also includes the fit from Haisch et al. (2001) and two other previous studies (Mamajek, 2009; Fedele, et al., 2010). These fits are shown as black dashed lines.

Furthermore, recent ALMA observations suggest that planet formation has already begun at the Class I stage of star formation (Segura-Cox, et al., 2020), when the protostar is ~0.1 Myr old, and may have progressed significantly by <1 Myr (Alves, et al., 2020). Alves et al. (2020) and Segura-Cox et al. (2020) have both observed ring-gap structures, which may be indicative of planet formation, in the dust components of disks around forming stars. Segura-Cox et al. (2020) find that the structures in disks around <0.5 Myr sources are consistent with dust grains growing in the early stages of planet formation, whilst Alves et al. (2020) find that a gap in the disk around a <1 Myr old star is consistent with having been carved out by a 4-70 M_{Jup} planet.

---

[2] Age estimates of pre-main sequence stars are not currently accurate, due the complexity and large number of physical processes that can vary between stars and populations (Jeffries, 2017).

One consequence of the relatively short timescale for planet formation discussed in this subsection is that, since it is often necessary to model star and planet formation as happening instantaneously due to computational constraints (Kouwenhoven et al., 2016), it is not wholly unreasonable to do so (e.g. Parker & Quanz, 2012).

1.3.4 Properties of Planets

The majority of stars are thought to have planets (Winn & Fabrycky, 2015).

Since the discovery of 51 Peg b, the first exoplanet found orbiting a main sequence star by Mayor & Queloz in 1995, our understanding of planets and their properties has broadened far beyond those in our own Solar System. There are now thousands of planets in the ‘exoplanet zoo’, and their unexpectedly diverse properties continue to expand and constrain our understanding of planet formation (Deleuil, et al., 2020; Zhu & Dong, 2021).

It can be challenging to derive the statistics of the overall exoplanet population (Zhu & Dong, 2021). However, it is now thought that the majority of stars host one or more planets (Winn & Fabrycky, 2015), with the average being at least one planet per star (Cassan, et al., 2012).

Exoplanets have been observed on an incredibly wide range of orbits, from those with orbital periods measured in hours (K2-137 b; 4.3h, 0.006 AU orbit; Smith et al., 2018), to planets orbiting as far out as 1000’s of AU (GU Psc b, ~2,000 AU orbit, Figure 1.9, Naud et al., 2014). It is often not possible to measure the eccentricities and inclinations of exoplanets with the current detection methods (Zhu & Dong, 2021). However, ~30-150° inclinations between exoplanets have been found by combining data from multiple missions (Damasso, et al., 2020; De Rosa, et al., 2020; Xuan & Wyatt, 2020; Zhu & Dong, 2021). In addition, many exoplanets are on retrograde orbits, where the planet is orbiting in the opposite direct to its stars rotation (WASP-17b, Anderson et al., 2010). All of these orbital properties provide key clues to the formation and dynamical evolution of planetary systems (Zhu & Dong, 2021).

Figure 1.10 (Zhu & Dong, 2021) shows the mass-semimajor axis relationship for the known exoplanet population, as of September 2020 out to 100 AU, and compares them to the Solar System planets. The exoplanet markers are coloured based on the method that was used to

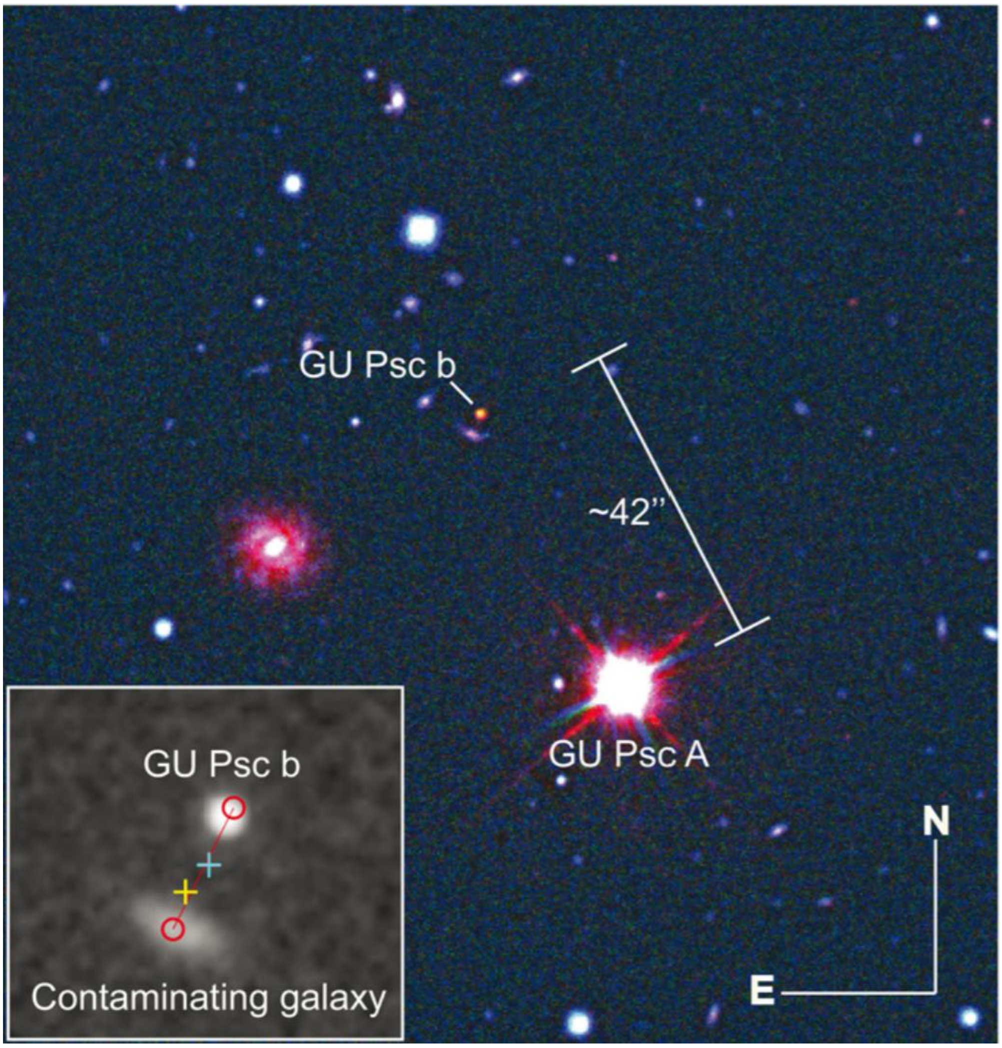

Figure 1.9 Image of the star GU Psc A, and its planet GU Psc b, an infrared composite of *i*-band (blue) and *z*-band from Gemini-South; and *J*-band (red) from WIRCam. The inset image shows what is likely an edge on galaxy which contaminates some of the GU Psc b signal. Naud et al. (2014) separate this from the planet's signal. Figure from (Naud, et al., 2014).

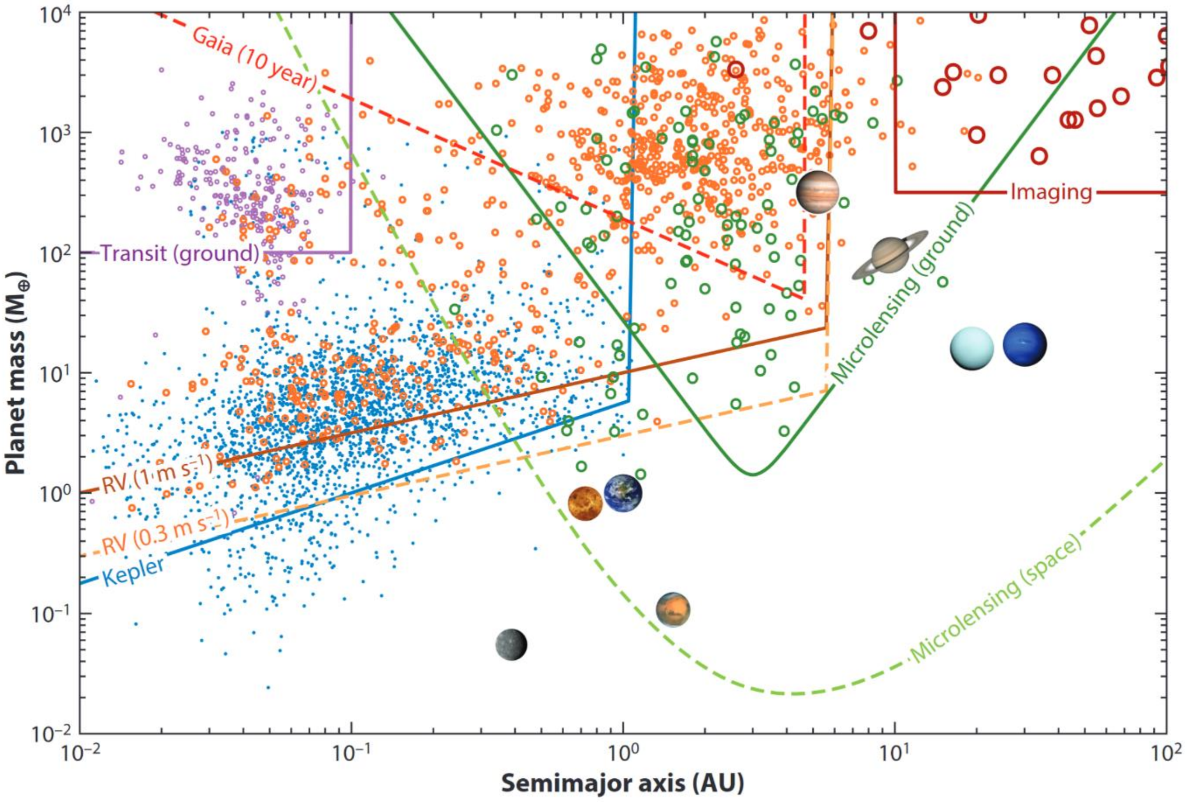

Figure 1.10 The mass vs semimajor axis distribution for known exoplanets and the Solar System planets, which have images of them as markers. The marker for each exoplanet is coloured based on the way that it was detected. Approximate sensitivity curves for each detection method are shown as solid or dotted lines, in a colour matching their respective planet marker. The estimates sensitivity curve for the Gaia 10-year survey, for which planet detections are expected in the future, is also shown as a red dotted line. Taken from Zhu & Dong (2021), the exoplanet data is up to date as of September 2020.

detect them: ground-based transit (purple), Kepler transit (blue), radial velocity (orange and brown), microlensing (green), and direct imaging (red). The transit detection method measures the dimming of a host star's light when a planet passes in between the star and the observer. This has been the most successful detection method so far, detecting around ¾ of confirmed exoplanets to date. Radial velocity exoplanet searches measure the Doppler effect on a host star's spectra, as caused by one or more planets, and was the method used by Mayor & Queloz (1995) to discover 51 Peg b. In detection by gravitational microlensing, an exoplanet is detected during a microlensing event between itself and a more distant object, or when a planet that is orbiting a lens star affects the microlensing signal in a measurable way (Gaudi, 2012). Finally, exoplanets have also been discovered through direct imaging, where the host star is blocked from the image, allowing the signal from an orbiting exoplanet to be detected. In the future, Gaia is also expected to discover exoplanets through astrometry, which detects a host stars movement around the centre of gravity of its planetary system compared to other nearby reference stars (Brown, 2021). The estimated sensitivity limit for these Gaia detections, as well as the other detection methods are shown as lines and labelled by detection method in Figure 1.10 (Zhu & Dong, 2021).

Each method of exoplanet detection has its own sensitivity limit and biases. This leads to planets with different properties being preferentially detected by different techniques, causing the grouping together of planets discovered by the same detection mechanism in Figure 1.10. Groups of exoplanets that are of particular interest to this thesis are hot Jupiters and directly imaged exoplanets. This is because it is likely not possible for these exoplanets to have gathered enough mass and formed at the distances from their stars that they are currently observed. This means that directly imaged exoplanets and hot Jupiters (Dawson & Johnson, 2018) probably require a dynamical explanation for their formation. As the sensitivity limits improve over time, for example with JWST, detecting exoplanets on wider orbits beyond the ice line will become less challenging (Deleuil, et al., 2020). This will lead to new insights into the formation of the ice giants in our own Solar System (Deleuil, et al., 2020), as well as the formation and dynamical evolution of planets on orbits that have formed dynamically. JWST is also expected to detect and characterise exoplanet atmospheres (Lustig-Yaeger, et al., 2019; Lin, et al., 2021), which will expand the study of exoplanet properties.

Also of particular interest to this thesis, but not shown in Figure 1.10, are the free-floating planets that have been discovered. These are planets that are not orbiting a host star, and are discussed further in Sections 1.3.5 and 1.5.3.

Hot Jupiters

Hot Jupiters are planets that have a mass ≥0.25 M_{Jup} and an orbital period of less than 10 days[3] (Dawson & Johnson, 2018). Despite having a low occurrence rate of ~0.5% to ~1.5% for Sun-like stars (Zhu & Dong, 2021), hot Jupiters have and continue to play a significant role in our understanding of giant exoplanets because of the relative ease with which they are detected through transit and radial velocity surveys, due to their high mass and close orbits (Dawson & Johnson, 2018).

There is no consensus on how hot Jupiters end up on their very close orbits, however there is strong evidence that their orbits are created dynamically, after the planet has already grown to a Jupiter mass (Dawson & Johnson, 2018). Hot Jupiter multiplicity statistics provide further evidence for the dynamical formation of hot Jupiter orbits. Only one out of the 49 hot Jupiters included in the Figure 1.10 (Zhu & Dong, 2021) sample has a close-in, small companion planet. This low multiplicity for hot Jupiters is likely a signature of the disruptive dynamical evolution that has formed their close-in orbits (Dawson & Johnson, 2018). Possible dynamical formation mechanisms begin with a hot Jupiter initially forming further out in a disk, so that Jupiter-masses can be achieved. In these models the hot Jupiter then migrates due to either secular interactions within its own disk/ planetary system, or due to interactions with other passing objects in the star formation environment. Secular interactions are discussed in Section 1.3.5, and dynamical interactions with cluster members are introduced in Section 1.5, before being further discussed and investigated throughout this thesis.

---

[3] This is significantly closer in than Mercury's orbit, which has a period is 88 days. For example, 51 b Peg orbits ten times closer to its star than Mercury does at 0.39 AU (Dawson & Johnson, 2018).

Directly Imaged Exoplanets

Direct imaging favours planets that are massive and young, when they are detectable in the infrared, and far away from their star, increasing the likelihood that the planet's luminosity can be detected (Winn & Fabrycky, 2015). Indeed, GU Psc b was discovered orbiting at ~2,000 AU using imaging. These observations of Gu Psc b and its star are shown in Figure 1.9 (Naud, et al., 2014).

Some directly imaged exoplanets that are on wide orbits, but still well within the intial extent of the protoplanetary disk, may have formed through disk fragmentation. However, similarly to hot Jupiters, the very wide orbits of many directly imaged exoplanets must be explained by secular interactions within the planet's original system or by external dynamical interactions with passing objects. This is something that we investigate in Chapter 4, where we compare the observed star-planet separation distribution for directly imaged exoplanets to those formed through external dynamical interactions in our simulations.

1.3.5 Secular Evolution of Planetary Systems

Secular interactions occur when a planet's orbit is changed by interactions with the protoplanetary disk or other planets in its own system (Kley & Nelson, 2012; Kouwenhoven, et al., 2016; Dawson & Johnson, 2018). This can happen throughout a planet's lifetime, including during its formation when the planet is still embedded within its protoplanetary disk (Kley & Nelson, 2012), and is in contrast to external dynamical interactions which are caused by bodies outside of the planet's own system. Sometimes, secular interactions can be severe enough to fully eject planets, and simulations show that this may have happened to a 5th giant planet during the early evolution of the Solar System (Nesvorný, 2011).

Planet-Disk Interactions

Viscous interactions between a planet and its disk can cause both inward and outward migration and is expected to be a major factor in the final architecture of planetary systems (Kley & Nelson, 2012). This migration is caused by non-axisymmetric features in the protoplanetary disk, such as spiral density waves, which can cause torques on the planet or protoplanet (Kley & Nelson, 2012).

Planet-disk interactions affect all orbital elements. However, changes in eccentricity and inclination are usually quickly damped, leaving only changes in the semimajor axis as the major outcome (Kley & Nelson, 2012). In particular, it is usually a decrease in semimajor axis that is caused by planet-disk interactions. For example, hot Jupiters may have formed through inward planet-disk migration (Dawson & Johnson, 2018).

Planet-Planet Scattering

Dynamical interactions between planets within a system can either act to stabilise or destabilise their orbits. In some cases, planets can reach mean motion resonances, where their orbits are mutually stabilised (Zhu & Dong, 2021). However, it's also possible for planets to destabilise each other's orbits, leading to changes in their orbital elements, or the ejection of planets. This is particularly the case for lower mass, inner planets, whose orbits are particularly susceptible to being disrupted by any giant planets in the same system (Huang, et al., 2017; Pu & Lai, 2021). However, the presence of a Jupiter analogue, which is massive enough for its orbit to remain stable despite interactions with outer giant planet, will tend to 'shield' the inner planets from disruptive scattering interactions (Hao, et al., 2013).

In general, the more planets that are in a system, the more frequently they are destabilised or ejected. For example, Hao et al. (2013) find that, when a planet is in a multiplanet system within an open-cluster, it is almost always more likely to be ejected compared to if it was the only planet orbiting it's star. In these simulations Hao et al. (2013) investigated both secular dynamical interactions and those with external bodies in the open cluster. Their results highlight how secular interactions can be triggered by external dynamical encounters, and then act to further destabalise the planetary system (Kouwenhoven, et al., 2016).

1.4 Formation Environments

As discussed, the majority of stars and their planets appear to form in filamentary structures within giant molecular clouds, where the stellar density exceeds that of the galactic field (Lada & Lada, 2003; Gieles, et al., 2012; André, et al., 2014). This means that the majority of stars form in regions with over 100 other stars (Lada & Lada, 2003; Porras, et al., 2003; Gieles, et al., 2012).

The exact fraction of stars that form in these environments is unclear (Gieles, et al., 2012). This is partly because the definition of a cluster that is used can significantly affect results. For example, Lada & Lada (2003) define clusters based on a surface density threshold. The minimum surface density threshold that is chosen for star-forming regions to be defined as clusters can therefore significantly affect estimates of how many stars form in clustered environments (Bressert, et al., 2010; Gieles, et al., 2012). Furthermore, studies tend to focus on relatively nearby star formation, meaning that the fraction of stars in clusters and groups could be different beyond ~1 kpc from the Sun (Bressert, et al., 2010; Porras, et al., 2003). However, the majority of stars do appear to form in relatively dense star-forming regions. And, since these regions tend to disperse on timescales of 10's of Myr, even stars and planets that are currently observed in isolation are likely to have formed within groups of other stars (Parker & Goodwin, 2007; Gvaramadze & Bomans, 2008).

The far-reaching impacts that these relatively dense environments can have means that understanding them is critical to our understanding of star and planet formation. For example, the properties of giant molecular clouds, such as their density and turbulence, directly impact the star formation rate (Girichidis, et al., 2011), and stars and their planets are thought to inherit the structure of the gas from which they formed (Elmegreen, 2000). The high densities in star-forming regions can also have a significant impact on the evolution of cluster members, and has the potential to both destroy and add new members to planetary systems. This is the case for both planets in general as well as our own Solar System – which is thought to have been partly shaped by the effects of its natal star cluster (Pfalzner, et al., 2018).

1.4.1 Definitions

The word ‘cluster’ is often used very generally to refer to groups of stars, including those which may host star formation. However, different studies choose different criteria to define a cluster, and the physical significance of these criteria is often unclear (Krumholz, et al., 2019). This is especially the case for young star-forming regions, as their hierarchical structure means that it is often not appropriate or possible to divide them into distinct groups of stars in a meaningful way.

In this thesis we therefore use ‘cluster’ to refer to a group of stars that are gravitationally bound, including open clusters and globular clusters, while an association is an unbound group of stars. We then use the phrase ‘star-forming region’ to refer to either a cluster or an association of stars within which star formation in taking place. It may also refer to regions in which star formation is less than a few Myr old and are highly substructured and embedded such that it would not be appropriate to divide them into distinct groups. One star-forming region may, therefore, evolve into several clusters or associations.

1.4.2 Planet Formation in Star-Forming Regions

As discussed in Section 1.3.3, observations of protoplanetary disks suggest that planets tend to form early on in a star’s lifetime, within the first few Myr (Richert, et al., 2018), or sooner (Alves, et al., 2020). Since star-forming regions disperse on timescales of 10 Myr, it then follows that planets formation occurs within the same environment as star formation.

Young star-forming regions are often embedded in molecular clouds of gas and dust, making observations of planets in these regions more challenging than that of stars (Lada & Lada, 2003). This means that young open clusters – which have remained bound after their initial star-forming evolutionary phase – are in many ways the ideal places to study planet formation and evolution (Mann, et al., 2017). For example, the properties of exoplanets can be studied statistically while controlling for host star metallicity. It is then disappointing that searches for planets in these environments tend to find fewer than expected (Mann et al., 2017; Quinn et al., 2012). However, this may be at least in part due to the small sample size, as well as difficulties in detecting these planets (Mann et al., 2017; Quinn et al., 2012).

Meanwhile, even fewer planets have been found in globular clusters, with none detected in a search of the globular cluster 47 Tucanae (Masuda & Winn, 2017). However, due to observational constraints and the relatively small sample size, there remains a ≈15 % probability that no planets would have been found if the planets in 47 Tucanae had the same occurrence rate, mass, and radius distributions of the Kepler planets (Masuda & Winn, 2017). Therefore, the possibility that longer-lived clusters contain planets similar to those in the field cannot be ruled out. More research is therefore needed into planet populations in clusters, as well as what might cause them to differ from those in the field, including external dynamical interactions (Masuda & Winn, 2017).

Nevertheless, there is direct evidence of planets having formed in star-forming regions. This includes observations of two Hot Jupiters orbiting main sequence stars in the Beehive open cluster (Quinn, et al., 2012), and exoplanet B1620-26b, which orbits a pulsar within M4 – a 12.7 Gyr old globular cluster (Sigurdsson, et al., 2003). This means that the study of star-forming regions is critical to the understanding of both star and planet formation.

1.4.3 Properties

Mass

The mass of young clusters ranges from ≈10 to $\gtrsim 10^5$ $M_\odot$. More massive clusters are less common (Lada & Lada, 2003; Portegies Zwart, et al., 2010). The initial mass function for groups of stars can be described by Equation 1.10, where $\beta = -2 \pm 0.2$. Although this is referred to as the initial cluster mass function, it also includes unbound associations, as well as bound clusters (Krumholz, et al., 2019).

$$\frac{dN}{dM} \propto M^{\beta} \qquad 1.6$$

There is no strong evidence that β varies more than ± 0.2 between different galaxies and environments. Where $\beta = -2$ then the slope of the distribution is such that the less common high-mass clusters produce the same mass of stars as the more numerous low mass clusters. There appears to be an upper limit to cluster masses of ~10^5 $M_\odot$ (Gieles, et al., 2006), with the limit in any given galaxy likely being dependant on the conditions (Krumholz, et al., 2019).

Density

Density is either measured for a region as a whole, within the half-mass radius, or for individual 'clumps' and areas of substructure. The density of both the whole star-forming region and areas and substructure within them has a significant effect on the formation and evolution of the stars and planets withing them.

Even the least massive and dense star-forming regions have stellar densities of a few stars per cubic parsec, for example Taurus has ≈5 stars pc^{-3}, compared to 0.1 stars pc^{-3} for the field (Korchagin, et al., 2003; King, et al., 2012). Conversely, massive star-forming regions can have densities as high as thousands of stars per cubic parsec, with the Orion Nebula Cluster having a stellar density of ≈5000 pc^{-3} (King, et al., 2012).

The initial density range of star-forming regions is thought to be ~10-1000 $M_\odot$ pc^{-3} (Parker, 2014). *N*-body simulations of young star-forming regions find that the initial density can peak quite rapidly. For example, a region of 1500 stars can reach peak densities of ~1000 $M_\odot$ pc^{-3} in its central regions (Parker & Quanz, 2012; Portegies Zwart, et al., 2010). However, this is followed by a decline, meaning that a region that peaked at ~1000 $M_\odot$ pc^{-3} can have densities of ~10 $M_\odot$ pc^{-3} after 10 Myr (Parker & Quanz, 2012).

Despite this decrease, the effects of temporarily high densities can be significant for planetary systems, as will be discussed in Section 1.5.

Effect of Redshift

Stars that are currently the same age as the Sun formed 4.6 Gyr ago, at a redshift of z~1. The star formation rate appears to peak at around $z = 1.9$ and has exponentially decreased thereafter (Madau & Dickinson, 2014). The star formation rate therefore appears to be much higher at the time that the Solar System formed compared to the rate that is observed at more recent times.

This means that, in the past, stars likely formed in much denser environments (Madau & Dickinson, 2014). The main evidence for this is from observations within the Milky Way, which find that star-forming regions tend to have higher stellar densities in areas that have higher star formation rates. It is then inferred that this would also be the case for earlier star formation. Star-forming regions in the past were therefore likely to be denser and more dynamically active on average.

Stellar Velocities

Observations suggest that stars within young star-forming regions have a low velocity dispersion. Pre-stellar cores in the NGC 1333 star-forming region are observed to have velocity dispersions of 0.5 km s^{-1}, which increases to 0.92 ± 0.12 km s^{-1} for young stars that are 1-2 Myr of age (Foster, et al., 2015).

In general, stars in young clusters tend to have velocity dispersions of ~0.1 to ~1 km s^{-1} (Table 1 in Portegies Zwart et al., 2010; Table 1.3 in Binney & Tremaine, 2008). This is lower than in the field, where stars have velocity dispersions ranging from ≈30 to ≈60 km s^{-1} depending on their age (Table 1.2 in Binney & Tremaine, 2008). This increase with age is likely due to a mix of factors, including dynamical interactions within the substructured star-forming regions and older stars having picked up higher velocity dispersions due to interactions with the galactic disk (Binney & Tremaine, 2008; Foster, et al., 2015). This lower velocity dispersion at early times has the effect of prolonging encounters with respect to the field and older clusters, meaning that they will tend to be more disruptive for the planetary systems that experience them.

Within star-forming regions the velocity dispersion is substructured and correlated with the size of the regions and areas of substructure. The Larson relation (Larson, 1981), which applies to molecular clouds, shows that the velocity dispersion of a region is proportional to its size:

$$\sigma = 1.1L^{0.38} \tag{1.7}$$

where σ in the velocity dispersion, in km s^{-1}, and L is the size of the region, in pc. This relation applies to whole molecular clouds of different sizes. However, the same trend of corelated velocity distributions is also seen for individual regions and cores within a given molecular cloud (Lada, 1987; Hacar, et al., 2013). The stellar velocity substructure is therefore inherited from the giant molecular cloud, in the same way as it's spatial substructure.

The stellar velocities, when combined with the mass of a star-forming region, determine its virial ratio, which is a measure of the dynamic state of a group of stars. The virial ratio, α, is given by Equation 1.8:

$$\alpha = \frac{T}{|\Omega|} \tag{1.8}$$

where T is the kinetic energy of the system, and Ω is its potential energy. The viral ratio of a group of stars is <0.5 when it is bound and collapsing under its own gravity, or sub-virial, and equal to 0.5 when it is in virial equilibrium. A group of stars with a virial ratio >0.5 is, then, unbound and expanding, or super-virial. This corresponds to a region that either formed unbound, or has become unbound e.g., due to tidal forces or gas expulsion (Tutukov, 1978; Goodwin, 1997; Baumgardt & Kroupa, 2007).

The virial ratio of a star-forming region can vary both over time, and across different areas within the same region. For example, 'clumps' of substructure with a region may collapse on local scales even if the region as a whole is not sub-virial.

Spatial Distribution

As previously discussed there is evidence that star-forming regions inherit substructure from their giant molecular clouds, and that this substructure is present both initially and for a time during their evolution (Cartwright & Whitworth, 2004; Sánchez & Alfaro, 2009; André, et al., 2010; André, et al., 2014; Kuhn, et al., 2014; Jaehnig, et al., 2015; Arzoumanian, et al., 2019; Ballone, et al., 2020).

The spatial substructure observed in star-forming regions may be fractal in nature (Elmegreen, 2000; Elmegreen & Elmegreen, 2001; Bastian, et al., 2007). Mathematically, a fractal is a never-ending pattern that is self-similar on all scales (Fractal Foundation, 2021). In this way, no matter how much you 'zoom in' on a fractal it will appear the same. However, physically, the self-similarity of fractal structures does end on some scale.

The initial spatial distribution can be quickly wiped out by dynamical interactions. This is shown by simulations and observations that show younger clusters tend to be more substructured than older ones. This effect is discussed in the following subsection.

1.4.4 Global Evolution

The evolution of a star-forming region can be intensely dynamic, and will vary significantly depending on its initial dynamical state. Loosely bound clusters and unbound associations tend to form within the least dense regions of a hub-filament structure. These regions will still be unstable to gravitational collapse, such that they form bound clumps that fragment into stars, but they may be super-viral and therefore not collapsing on a global scale. Bound clusters, then, form within the densest regions of the hub-filament structures. These regions are more rapidly collapsing, and will tend to produce a higher number of stars that are closer together. Then, during its subsequent evolution, a more massive cluster will tend to dynamically evolve more rapidly as it is more likely to be sub-virial. In this way, the properties of mass, density, and virial ratio of a region are closely linked both each other and the fate of the region.

Sub-virial Regions

After a few Myr, once the gas has cleared, individual clusters and associations begin to emerge from the giant molecular cloud. By this point, in regions or areas of regions that are sub-virial, some of the initial substructure may have already been wiped out as the system begins to undergo dynamical interactions and tends towards equilibrium.

As the system tends towards equilibrium, there are important relaxation mechanisms that occur on the scale of the motion of individual bodies. Within bound clusters, and bound clumps of substructure, this ‘relaxation’ towards equilibrium can occur through violent and two-body relaxation. This is because these regions tend to be dense enough that dynamical interactions between bodies are common and have a significant effect on the evolution of both the system as a whole and the individual bodies within it. Systems such as this are known as collisional systems.

Both violent and two-body relaxation result in dynamical interactions which ‘mix’ the bodies in the star-forming region and dilute the initial substructure (Goodwin & Whitworth, 2004; Allison, et al., 2010). Violent relaxation (Lynden-Bell, 1967) occurs when a system is out of equilibrium with its own large-scale gravitational potential. For example, when a star-forming region is substructured, the areas of substructure will likely not be in equilibrium with the global potential of the system. The movement of individual bodies that is caused by this, and the changes in the global properties of the regions as a whole, mean that the gravitational potential varies over time. This cycle, where the potential causes the movement of bodies within the system, and that movement in turn affects the potential, continues until the bodies and their potential reach equilibrium. Meanwhile, in two-body relaxation (Spitzer, 1987), kinetic energy is exchanged between individual passing bodies within the star-forming region. This has the effect of transferring energy between them, such that the velocity of the slower body will tend to increase and the velocity of the faster body will tend to decrease during the encounter. Over time, the velocities of the bodies within a cluster will therefore tend towards the average value.

If a star-forming region forms with substructure, the substructure be erased over several dynamical timescales. Star-forming regions that are still substructured are, therefore, seen as dynamically young, and groups of stars that have a smooth spatial distribution are seen as dynamically old (Sánchez & Alfaro, 2009). This dynamical evolution can happen very quickly, over timescales of $\lesssim 1$ Myr (Jaehnig, et al., 2015; Sills, et al., 2018).

The implications for the individual stars and planets within a cluster that undergoes a virial collapse can be profound, and sometimes detrimental. This is the focus of Section 1.5.

Super-virial Regions

Relaxation towards equilibrium occurs differently for super-virial, unbound systems as these tend to initially expand. This happens because the individual bodies are out of equilibrium with the global potential, in the same way as violent relaxation. This can happen to associations of stars which have formed unbound, or to star-forming regions which have become unbound over time. The expansion can happen either quickly or very slowly, with the stars in low-mass associations simply slowly drifting apart with individual motions that do not form a coherent movement with the other members of the association. It is important to note, however, that local areas of substructure can still be sub-virial in such regions. These areas can collapse to local densities that are high enough for encounters to become more frequent, therefore causing dynamical interactions even if the region as a whole is expanding. However, the region as a whole will not have undergone significant dynamical mixing.

Dispersal

Groups of stars that form unbound inevitably disperse over time. However, this is also the fate of the majority of bound star clusters. Over the course of a star-forming region's dispersal, stars may slowly drift apart, or be more rapidly ejected from the region by dynamical interactions.

It is the more massive star-forming regions that will tend to be longer-lived, potentially evolving to become open and globular clusters (Portegies Zwart, et al., 2010). However, the majority of star-forming regions disperse on timescales of 10's of Myr and are therefore sources of stars in the field (Lada & Lada, 2003; Goodwin & Bastian, 2006). At ages of 30 Myr, 10% of stars remain in bound clusters (Krumholz, et al., 2019).

1.5 Environmental Effects on Stars and Planets

The most significant factor that determines the extent to which a star and its planets are affected by external mechanisms is the density of the star-forming region (Parker, 2020). And, as we have discussed, star-forming regions can be very dense. Furthermore, relatively high global densities can be increased on local scales by the substructured nature of star-forming regions as well as their collapse on global and local scales. In this section, I discuss the dynamical evolution of stars and planets within star-forming regions, including how our current understanding can begin to explain the unexpected characteristics of some observed exoplanets.

1.5.1 Stars

As a star-forming region evolves, so too do the bodies within it. The positions of the stars within a region can change dramatically as they travel around the region following dynamical interactions with other members and the potential of the region as a whole. In particular, stars can be ejected from a region, or 'sink' towards its centre through mass segregation.

Ejection produces runaway and walkaway stars, and can be caused by dynamical interactions (Poveda, et al., 1967) or when the binary companion of the ejected star undergoes a core-collapse supernova (Blaauw, 1961). Many candidate runaway and walkaway stars have been discovered, including from the ONC using Gaia data (Schoettler, et al., 2020).

In mass segregation, more massive stars evolve towards the centre of the region over ~10 Myr (Parker, et al., 2016). Recent result shows that this happens in young clusters through Spitzer's instability (Spitzer, 1969), where the high mass stars do not meaningfully interact with the much more numerous lower mass stars (Parker, et al., 2016; Spera, et al., 2016). Instead, the high mass stars will tend to form a sub-system of their own in the centre of the region, which is decoupled from the lower mass bodies (Allison & Goodwin, 2011).

1.5.2 Planet Formation

As discussed in Section 1.3.1, the size and mass of protoplanetary disks can be affected in any environment through mechanisms such as photoevaporation by the central star and truncation of the disk by a stellar binary companion. It is also possible for mechanisms that are external to the star-planet system to affect protoplanetary disks, and therefore the formation of planets. These external mechanisms can be common in star-forming regions because of the relatively proximity of objects in denser environments.

Two external mechanisms that affect protoplanetary disks are encounters with other objects in the region and photoevaporation by a nearby massive star, both of which act to remove or truncate the disk, thereby reducing the maximum distance from the central star at which a planet could form (Scally & Clarke, 2001; Williams & Cieza, 2011; Vincke & Pfalzner, 2016; Winter, et al., 2018b). For the ONC and ONC-like clusters with 4000 stars, simulations show that the combined effect of these two mechanisms is to cut down the average disk size to 10's of AU (Scally & Clarke, 2001; Adams et al., 2006).

Photoevaporation

Figure 1.11 shows disks within the ONC that are in the process of being photoevaporated. "Proplyds" can be seen around these stars, which are the thin shell-like ionisation fronts of material from the evaporating disks (O'dell, et al., 1993; Haworth, et al., 2021).

Photoevaporation by massive stars is the primary mechanism that depletes the outer region of protoplanetary disks. It happens when ultraviolet radiation heats material near the surface of the disk, such that gas at the surface is no longer gravitationally bound (Armitage, 2020). This increased temperature causes a build-up of pressure, and a pressure gradient within the disk, which launches winds through which the unbound material is lost, thereby causing significant mass loss (Facchini, et al., 2016).

Regardless of the density of a star-forming region, if a least one massive star is present then the protoplanetary disks of the other stars will be affected by its external photoevaporation (Nicholson, et al., 2019). However, disks that are closer to the massive star will receive a higher

Figure 1.11. Protoplanetary disks within the ONC. The disks closest to the massive star Theta Orionis C are being photoevaporated and appear bright as a result. The topmost protoplanetary disk is instead seen as a dark silhouette against the background as it is not currently being illuminated by the massive star. Credit: ESA/Hubble, under Creative Commons Attribution 4.0 license.

flux. So, the effects of external photoevaporation are more severe for denser star-forming regions where other stars will be closer to the photoevaporating massive star (Concha-Ramírez, et al., 2021).

Disks can be photoevaporated down to distances that are relatively close to their central star, which means that the planet forming region can be depleted or destroyed (Adams, et al., 2004). This includes distances where the formation of giant planets in the Solar System would have been significantly hampered (Adams, 2010). For example, Adams et al. (2004) found that over ~10 Myr, disks can be truncated down to ~10 to ~20 AU depending on the mass of the central star and density of the region. An implication of this is that star-forming regions that contain B or O stars, such as those comparable to the ONC, may have significantly supressed giant planet formation as the disks may have already lost a significant amount of gas before giant planets have had time to fully form through core accretion (Armitage, 2000; Nicholson, et al., 2019; Concha-Ramírez, et al., 2019). This is especially the case for giant planets because it is primarily the gas component of the disk that is evaporated, while the dust component remains mostly intact provided that the particles have grown to ~1cm in size such that they decouple from the gas (Adams, et al., 2004).

The two types of radiation that are most destructive to disks are far ultraviolet (FUV, $hv =$ 6 to 13.6 eV) and extreme ultraviolet (EUV, hv >13.6 eV) (Fatuzzo & Adams, 2008). These two types of radiation account for a significant amount of the luminosity produced by high mass stars. For example, a 10 $M_{\odot}$ star will emit an FUV flux of ~10^{37} erg s^{-1}, and an EUV flux of ~10^{35} erg s^{-1} (Armitage, 2000). Although both FUV and EUV radiation can photoevaporated disks, it is the FUV flux that is the most destructive (Adams, et al., 2004). And the FUV flux will be high enough to affect protoplanetary disks in any region that contains a massive star (Nicholson, et al., 2019).

The FUV flux dominates the destruction of protoplanetary disks despite being of lower energy than the EUV radiation because the FUV radiation is unable to penetrate as far into the disk (Fatuzzo & Adams, 2008). Its effects therefore become concentrated in the least dense outer regions of the disk, where thermal pressure builds up, causing more outflows through which the disk material is lost to the surroundings and interstellar medium (Armitage, 2000). An ionisation front, such as those shown in Figure 1.11, forms where the outflows meet the EUV radiation and prevent EUV radiation from penetrating the disk (Johnstone, et al., 1998; Störzer & Hollenbach, 1999). This results in the FUV radiation being significantly more destructive.

FUV photoevaporation primarily happens through FUV pumping followed by the collisional de-excitation of H_2 molecules (Johnstone, et al., 1998). In this mechanism, H_2 molecules are excited by FUV photons. They may then decay to a vibrational ground state, when the vibrational energy is converted to heat through collisional de-excitation with other hydrogen atoms and molecules (Adams, et al., 2004).

Encounters

Encounters with other stars, planets, and binary systems also have the potential to truncate or entirely destroy protoplanetary disks. The frequency of encounters between planetary systems and passing bodies is heavily dependent on density which, as we have seen, can vary both spatially and over time within a cluster (Spurzem, et al., 2009; Parker & Quanz, 2012).

Simulations show that dynamical interactions tend to truncate disks at ≈⅓ of the distance of closest approach (Clarke & Pringle, 1993; Adams, et al., 2006). Close encounters within these distances are necessary to truncate disks, as even the cumulative effect of distant interactions does not significantly truncate protoplanetary disks (Winter, et al., 2018a). However, for the densest and most massive of star-forming regions, such as those similar to the 32,000-star NGC 6611, close encounters can cause the average disk size to be truncated down to ~50 AU (Vincke & Pfalzner, 2016).

Nevertheless, this still leaves the planet-forming regions within 30 AU intact for the majority of systems, even within the densest of star-forming regions. Photoevaporation is therefore the primary form of protoplanetary disk destruction in star-forming regions, especially with respect to negative effects on planet formation (Winter, et al., 2018b).

1.5.3 Dynamical Evolution of Planetary Systems

Planets that do successfully form in star-forming regions may experience further environmental effects in the form of dynamical encounters that affect the orbits of the planets themselves, and not just the disk. Most often, studies focus on encounters between a planetary system and another star or pair of binary stars. However, it is also possible for other bodies, such as free-floating planets, to interact with planetary systems (Wang, et al., 2015).

In relatively dense star-forming regions, with densities of ≥ 100 M$_\odot$ pc^{-3}, it is not uncommon for encounters to significantly affect the dynamical evolution of the planets within the region. These effects can range from smaller disruptive changes in the structure of a planetary system to the ejection, and even addition, of planets (Fregeau, et al., 2006). This means that dynamical interactions in star-forming regions have the potential to explain the unexpected orbits that are observed in some exoplanets.

Disruption

One outcome of external encounters with other objects in the star-forming region is for a planet's orbit to be changed. For example, Winter et al. (2020) argue that hot Jupiters are mostly likely formed though external dynamical interactions, which alter their semimajor axis, rather than through secular migration or planet-planet scattering.

The definition of a disrupted planetary system can be somewhat arbitrary. In particular, in multi-planet systems, it is possible for a seemingly small perturbation to a planet's orbit to trigger long-term secular evolution which can eventually results in the destabilisation of the system. However, this does not mean that any small change should be seen as genuine disruption. Parker & Quanz (2012) choose to define a planet as having been disrupted if its eccentricity is raised above 0.1, or its semimajor axis is changed by more than 10%. This is because if an innermost giant planet is disrupted in this way, it will tend to destabilise any terrestrial planets in its system, therefore having caused a genuine wide-scale disruption to the planetary system.

Planetary orbit disruption is significant in environments with stellar densities of >100 M$_\odot$ pc^{-3} (Parker, 2020). For example, Parker & Quanz (2012) find that, in regions with 3000 stars and peak densities ~3420 M⊙ pc^{-3}, between 10-20% of planets are disrupted for initial semimajor axes of 5 and 30 AU, respectively.

Earlier simulations found that only the densest of clusters, with densities of >1000 M⊙ pc^{-3}, would lead to a significant number of planetary systems being disrupted (Bonnell, et al., 2001). However, these studies simulated clusters using smooth distributions, such as Plummer spheres (Plummer, 1911) or King profiles (King, 1962) for the spatial distribution, and uniform velocity dispersions of ~1 kms^{-1}. These are accurate models to use for groups of stars that are dynamically old. However, as discussed throughout this Chapter, young star-forming regions are highly substructured in terms of their spatial and velocity distributions and are therefore more dynamically active.

A planetary system can be disrupted either by a single strong encounter, or by several weaker encounters (Spurzem, et al., 2009). Factors that determine whether an encounter is weak or strong include the distance of closest approach, the mass and speed of the incoming body, and the eccentricity of the incoming body's trajectory. In terms of the planet's orbit, a planet with a smaller binding energy is more likely to be disrupted. The binding energy is given in Equation 1.9 where E_b is the binding energy of a planets orbit, M_s is the stellar mass, m_p is the mass of the planet, and a_p is the semimajor axis. This means that planets on wider orbits, of lower mass, or orbiting a lower mass star are more easily disrupted. These factors can be summarised as an encounter being stronger when the energy of the interaction is higher, or the binding energy of the planetary system is lower.

$$|E_b| = \frac{\text{G}M_\text{s}m_\text{p}}{2a_\text{p}} \tag{1.9}$$

For a planet that is disrupted, the likely change to its orbit can be understood in terms of the Heggie-Hills Law (Heggie, 1975; Hills, 1975a; Hills, 1975b). The Heggie-Hills Law describes the behaviour of a binary system after an encounter, as determined by the binding energy of the binary system and the Maxwellian energy[4] of the surrounding bodies. In this case, the binary

---

[4] In this treatment, the stars in a star-forming region are analogous to molecules of gas that are in thermal equilibrium.

system is a star-planet binary, and the Maxwellian energy is a measure of the average energy of the stars in a star-forming region. The Maxwellian energy is given by Equation 1.10, where $\langle m \rangle$ is the average mass of a star in the region, and σ is the velocity dispersion.

$$E_{\mathrm{Max}} = \langle m \rangle \sigma^2 \tag{1.10}$$

If the binary's binding energy is smaller than the Maxwellian energy, then the semimajor axis is likely to decrease. If the binding energy is larger than the Maxwellian energy, then the semimajor axis is likely to increase. In this way, planets that are tightly bound with respect to the Maxwellian energy of the region tend to get more tightly bound following an encounter, and loosely bound systems tend to become more loosely bound. This can cause an increasingly disruptive cycle for loosely bound planets that experience multiple encounters, as they will tend to become more loosely bound after each encounter, potentially leading to their ejection from the system.

Ejection and the Creation of Free-Floating Planets

One possible outcome of encounters is the creation of free-floating planets that have been ejected from their planetary system. Parker & Reggiani (2013) find that a binary system, including that of a planet and star, will be broken up by an encounter if the kinetic energy of the incoming body is greater than ~10 times the binding energy.

Despite being challenging to detect, the existence of free-floating planets has been confirmed by various observations using gravitational microlensing (Sumi, 2011; Mróz, 2020), direct imaging (Zapatero Osorio, et al., 2000), and radial velocity surveys (Clanton & Gaudi, 2017). However, their abundance remains unclear (Zhu & Dong, 2021). Gravitational microlensing observations by the MOA & OGLE Collaborations (Sumi et al., 2011) suggested that free-floating planets may be almost twice as common as main-sequence stars. However, this observed population is likely to be contaminated by bound planets on orbits wider than $\gtrsim$10 AU (Clanton & Gaudi, 2017). Despite this, other observational studies do find that free-floating planets are likely to be approximately as common as main-sequence stars (Clanton & Gaudi, 2017; Mróz, et al., 2019).

The origin of free-floating planets is debated. It can be argued that they form in the same way as stars and brown dwarfs, which would arguably make them brown dwarfs rather than planets (Chabrier, et al., 2014). However, there is clear evidence from simulations that planets can be ejected from their original system as a natural result of secular interactions and the external dynamical interactions that occur in star-forming regions. Some interactions with passing bodies can be strong enough to immediately eject a planet (Parker & Quanz, 2012; Wang et al., 2015; Hao et al., 2013). This is known as prompt ejection. Weaker interactions can create free-floating planets by either triggering long-term secular interactions, or by being part of a string of successive weak encounters with the cumulative effect of ejecting the planet (Parker & Quanz, 2012; Wang et al., 2015; Hao et al., 2013). This is known as delayed ejection.

Parker & Quanz (2012) found that 10% of planets are promptly ejected from their original system for star-forming regions with densities of 1000 $M_\odot$ pc^{-3}; this figure would likely be higher if delayed ejection through secular interactions was included.

Captured Planets

Free-floating planets can be subsequently captured by another star, or even recaptured by their original star (Parker & Quanz, 2012; Perets & Kouwenhoven, 2012; Wang, et al., 2015; Parker, et al., 2017). Within clusters this tends to happen during expansion, as the gravitational influence from other members decreases, but while there is still a significant chance of a free-floating planet approaching close enough to a star to be captured by it (Perets & Kouwenhoven, 2012).

Planets tend to be captured onto highly eccentric, inclined, and wide orbits (Perets & Kouwenhoven, 2012; Parker & Quanz, 2012), with semimajor axes generally between ~100s to $\sim 10^6$ AU (Perets & Kouwenhoven, 2012). Planet capture therefore offers a possible formation mechanism for the extreme orbits observed for some exoplanets (Perets & Kouwenhoven, 2012; Parker & Quanz, 2012).

Stolen Planets

It is also possible for a planet to be directly stolen from another system (Li & Adams, 2016; Mustill, et al., 2016; Wang, et al., 2020). In this scenario, a planet is exchanged between passing systems and goes directly from being bound to one star to the other. Similarly to disruption and ejection, this is more likely to happen to planets that are on wide orbits around their original star, as they are more loosely bound (Parker & Quanz, 2012; Li & Adams, 2016). And, similarly to captured planets, those that have been stolen tend to have large semimajor axes and eccentricities, as well as often being exchanged onto retrograde orbits. I investigate potential differences in the orbits of stolen and captured planets in Chapter 4.

1.5.4 Implications for The Solar System

Where did the Sun form?

It is thought that the Sun formed in a star-forming region which likely consisted of ~1000 to ~10,000 stars (Summarised in table 2 and figure 7 of Adams, 2010); potentially within the M67 open cluster (Önehag, et al., 2011). Arguments for a clustered formation environment include that it would be unlikely for our Sun to have formed in a different environment than the majority of other stars. However, there is also more direct evidence, such as relative overabundances of the daughter isotopes of 26Al and 60Fe in meteorites[5] which suggest that a supernova occurred within close proximity ($\lesssim$ 1 pc) of the young Sun (Parker & Dale, 2016).

26Al and 60Fe are short-lived radioisotopes, defined as having mean lifetimes of less than 100 Myr (Gounelle & Meynet, 2012). And, in the context of a young star-forming region, they are most likely produced by nucleosynthesis within massive stars before being expelled in supernovae (Goswami, 2004). The observed meteoric abundances could then have resulted from the direct enrichment of the Sun's circumstellar disk by a nearby supernova event (Parker, et al., 2014). Or, alternatively, the Solar System could have formed from pre-enriched material as part of a sequential star-forming event (Gounelle & Meynet, 2012). In this scenario the evolution of previous generations of stars in the Sun's star-forming region would have both triggered the Sun's formation and pre-enriched the material from which it formed (Gounelle & Meynet, 2012).

---

[5] More specifically, they are found in the youngest components of meteorites; such as calcium-aluminium-rich inclusions which, when they solidified from molten droplets, would have been the first solids to form in the Sun's protoplanetary disk (Gounelle & Meynet, 2012).

Parker & Dale (2016) find that the direct enrichment scenario may be more likely. Regardless, both observation and theory expect that the Sun formed within a group of stars from, making research into these environments particularly relevant to our own Solar System.

Planet 9

There are many ways that a clustered environment may have affected the Solar System. For example, the Edgeworth-Kuiper belt has an abrupt edge at 50 AU, and some trans-Neptunian objects have high eccentricities and inclinations, characteristics which could be explained by an encounter with a passing star (Kenyon & Bromley, 2004; Pfalzner, et al., 2018).

There is also ongoing research into the existence of Planet 9 – a hypothetical Super-Earth/mini-Neptune that is thought to orbit in the outskirts of our Solar System beyond the Kuiper Belt (Batygin & Brown, 2016; Batygin, et al., 2019). Its existence is proposed in order to explain the observed clustering of several trans-Neptunian objects (Batygin, et al., 2019).

Should it exist, Planet 9 is expected to orbit with a semimajor axis 380^{+140}_{-80} AU, perihelion 300^{+85}_{-60}AU, eccentricity ~0.2, inclination 16±5°, and mass $6.2^{+2.2}_{-1.3}$ $M_{\oplus}$ (Brown & Batygin, 2021).

Some studies find a pessimistic view of the likelihood that Planet 9 exists (Shankman, et al., 2017; Napier, et al., 2021). However, Batygin et al. (2021), find that, should Planet 9 exist, its detection may require further dedicated searches (Batygin, et al., 2019).

If Planet 9 does exist, its current orbit would likely have formed dynamically: not only would it be very hard to form a planet at such large distances from its star because of the lack of material in the disk, but its eccentricity and inclination would also not immediately result from it having formed in the disk with the other planets (Batygin & Brown, 2016). It is then possible that Planet 9 either formed in the Solar System and was scattered out onto a larger orbit, was directly stolen from another system, or was captured after being a free-floating planet.

One issue with scattering a planet onto such a wide orbit is that it tends to be more likely that the planet is simply ejected, as it must lose a significant fraction of its initial binding energy (Li

& Adams, 2016). However, it is still possible that Planet 9 was scattered out onto its current orbit through secular interactions (Batygin & Brown, 2016; Li & Adams, 2016).

It is also possible that Planet 9 is from another planetary system, and that it has been stolen or captured. The probability of Planet 9 being stolen onto its predicted orbit has been found to be of order 0.01 - 1% by Li & Adams (2016) and Mustill et al. (2016). Li & Adams (2016) find that the capture of Planet 9 onto its current orbit its slightly less probable than it having been directly stolen – especially if, in the stolen scenario, it initially had semimajor axis of >100 AU around its original star. However, Parker et al. (2017) find that this probability is even lower – nearly 0 – when evidence suggesting that the Sun formed in a dense cluster is taken into account.

1.6 Summary

In this chapter, I have discussed the environments within which stars and planets form. In particular, I have focussed on the effects that the high densities of these environments can have on the processes of star and planet formation and the dynamical evolution of stars and planets over time.

Motivation for studying the dynamical evolution of stars and planets comes from both observation and theory. For example, numerous exoplanets have now been observed on orbits that cannot be fully explained by the current theories of star and planet formation, whether that be core accretion (Pollack, et al., 1996) or the fragmentation of stellar disks (Boss, 1997; Mayer, et al., 2002). These include dozens of possibly planetary-mass companions that have been observed with unexpectedly high eccentricities and semimajor axes, with some orbiting as far as $\gtrsim$2500 AU from their host star (e.g. Luhman et al., 2011; Deacon et al., 2016). Furthermore, simulations suggest that free-floating planets are likely to be common, and several likely candidates have been discovered (e.g. Zapatero Osorio et al., 2000; Dupuy & Kraus, 2013; OGLE. et al., 2019; Mróz, 2020).

Meanwhile, in our Solar System, should the proposed Planet 9 exist (Sheppard & Trujillo, 2016; Batygin & Brown, 2016; Batygin, et al., 2019; Clement & Kaib, 2020; Downey & Morbidelli, 2020), its orbit is likely to be very wide ($a \sim 400 - 800$ AU), eccentric ($e \sim 0.2$–0.5), and inclined ($i \sim 15$–$25°$) to the plane of the other planets (Batygin, et al., 2019; Fienga, et al., 2020). (However, see also Shankman et al. (2017) and Napier et al. (2021) for a more pessimistic view regarding the likelihood of Planet 9's existence.)

Star-forming regions tend to be relatively dense compared to the galactic field, which has a stellar density of 0.1 stars pc^{-3} (Korchagin et al., 2003). For example, Taurus has a stellar density of ≈5 stars pc^{-3}, and the most massive star-forming regions can have $\gtrapprox$1000 stars pc^{-3}, with the Orion Nebula Cluster having a central density of ≈5000 stars pc^{-3} (King, et al., 2012).

It is these relatively dense environments that can have significant effects on their members. This is because dynamical interactions readily occur in high density environments, where close encounters between systems can be common as the stars are closer together. This is particularly the case for the substructured and filamentary regions in which most stars and their planets form (Lada & Lada, 2003; Cartwright & Whitworth, 2004; André, et al., 2014; Daffern-Powell & Parker, 2020). This is because, the substructured nature of star-forming regions can also further increase the frequency of dynamical interactions, as areas of substructure have higher local densities than the global density of the region as a whole (Cartwright & Whitworth, 2004; Sánchez & Alfaro, 2009; André, et al., 2010; Parker & Meyer, 2012; André, et al., 2014; Kuhn, et al., 2014; Jaehnig, et al., 2015; Arzoumanian, et al., 2019; Ballone, et al., 2020). Furthermore, denser regions will tend to contain a higher percentage of protoplanetary disks that are close enough to experience destructive photoevaporation by nearby massive stars.

Star-forming regions therefore have the potential to truncate and destroy protoplanetary disks through photoevaporation and encounters with other stars (Williams & Cieza, 2011; Nicholson, et al., 2019). Then, as planetary systems evolve, they may be further disrupted by encounters with other members. This can ultimately lead to the destruction of planetary systems and the creation of free-floating planets. However, encounters can also lead to the addition of new members by the capture of these free-floating planets as well as the theft of planets from other systems.

Together, the effects of dynamical interactions can begin to explain the unexpected orbits that are observed in many exoplanets, as well as in our own Solar System. Simulations of young star-forming regions play an important role in investigating these effects because they can happen over long time scales, and it is therefore impossible to directly observe them taking place.

1.7 This Thesis

This thesis focusses on the ways in which the substructured nature of star-forming regions can affect the stars and planets within them. I begin by investigating only gravitational dynamical effects, before moving on to introduce the effects of photoevaporation. I do this by following the evolution of stars, their planets, and protoplanetary disks through N-body simulations of young star-forming regions over 10 Myr.

In terms of the structure of this thesis, I begin by outlining the computational methods used throughout in Chapter 2, Methods. This includes the set-up of the chosen initial conditions that are input into N-body simulations, and an outline of the N-body integrator used. Methods used to analyse the output from the N-body simulations are discussed in the relevant Chapter.

In order to study the effects that substructure can have on stars and planets, the spatial substructure itself needs to be understood and quantified. In Chapter 3, The Dynamical Evolution of Fractal Structures in Star-Forming Regions, I assess the suitability of the commonly used Q-parameter method for quantifying substructure within star-forming regions. I do this by following the global dynamical evolution of simulated star-forming regions that contain only stars. I discuss how well the Q-parameter is able to describe the substructure in these simulated star-forming regions in the context of the observed substructure in the ONC, IC 348, and NGC 1333.

In Chapter 4, Theft and Capture in Star-Forming Regions, I move onto study the effects that dense star-forming environments can have on the dynamical evolution of planets. I investigate the mechanisms of planet theft and capture separately, and discuss their similarities and differences in terms of the outcomes for planets within our simulations.

In Chapter 5, Can Jupiters form before they are ejected?Can Jupiters form before they are ejected?, I build on the work in Chapter 4 and question whether the planets that undergo theft and capture in my simulations would likely have been able to form in such a dense environment. In particular, I question whether the disks from which they form would have been affected by external photoevaporation in a way that is detrimental to planet formation.

Finally, I summarise Chapters 3, 4, and 5 in Chapter 6, Conclusions, and briefly discuss the current outlook of the field.

Chapter 2

Methods

In this Chapter I describe the computational methods that are used in the following chapters to simulate the evolution of substructured star-forming regions. To do this I create synthetic star-forming regions that are populated with point-mass stars, and then evolve these over time through N-body simulations. I begin by describing how the initial conditions of the star-forming regions are set up. Then, I describe how the star-forming regions are evolved over time using N-body simulations. Specific initial conditions, including the inclusion of planets, and the methods used to analyse the simulations are discussed in the corresponding science chapters (Chapter 3 and Chapter 4).

2.1 Initial Conditions

As discussed in Chapter 1, observations show that the distributions of newly formed stars in star-forming regions tends to be substructured, and simulations show that this substructure can have significant effects on the evolution of stars and planets. A relatively simple way of creating a substructured and 'clumpy' star-forming region is to use a fractal to determine the initial spatial and velocity distribution of the particles (Goodwin & Whitworth, 2004).

It is unclear whether the spatial structure of very young star-forming regions is, in fact, fractal in nature. However, they are substructured, and may have a fractal spatial distribution, as discussed in Section 1.4.3,. So, this remains a more accurate initial distribution than the smooth radial density profiles and Plummer spheres that are often used (Plummer, 1911; King, 1962; Kroupa, 2008).

In the following subsections I describe the box-fractal method which was introduced by Goodwin & Whitworth (2004). The box-fractal method is commonly used to set up the spatial and velocity structure in *N*-body simulations (e.g. Goodwin & Whitworth, 2004; Allison et al., 2010; Parker & Quanz, 2012; Parker & Meyer, 2014; Daffern-Powell & Parker, 2020) and is used throughout this thesis.

2.1.1 Spatial Distribution

First, the star-forming region is generated, using the method outlined in Goodwin & Whitworth (2004):

(i) A cube with sides of length $N_{\rm div} = 2$ is defined. It is within this cube that the star-forming region is generated. The first 'parent' particle is placed at the centre of the cube.

(ii) The cube is divided into sub-cubes, each with length 1. So, here, there are ${N_{\rm div}}^3 = 8$ sub-cubes. A 'child' particle is placed at the centre of each sub-cube.

(iii) The probability that a child particle now becomes a parent itself is ${N_{\rm div}}^{D-3}$, where D is the chosen fractal dimension.

(iv) Child particles that do not become parents themselves are removed as well as all of the previous generation of parent particles. In order to prevent a gridded appearance, children that do become parents have a small amount of noise added to their distribution.

(v) Each new generation of parent particles is treated in the same way as the initial parent particle, and their sub-cubes are treated as the initial cube. In this way, each new parent's sub-cube is divided into ${N_{\mathrm{div}}}^3 = 8$ as the process is repeated until there is a generation created that has significantly more particles than is needed.

(vi) Any remaining parent particles are removed so that only the last generation of particles is left.

(vii) The region is pruned so that the particles sit within a spherical boundary, rather than a cube.

(viii) If there are more particles than the chosen number of stars, particles are removed at random until the chosen number is reached. Removing stars at random maintains the chosen fractal dimension as closely as possible.

The mean number of children that become parents is ${N_{\mathrm{div}}}^D$ (Goodwin & Whitworth, 2004). This means that, when $N_{\mathrm{div}} = 2$, fractal dimensions of $D = 1.6$, 2.0, 2.6, and 3.0 correspond to the mean number of new parents at each stage being close to an integer. These values, therefore, produce the chosen fractal dimension more accurately (Goodwin & Whitworth, 2004). Lower fractal dimensions lead to fewer children becoming parents, and therefore more substructure. A fractal dimension $D = 1.6$ therefore corresponds to the maximum amount of substructure possible for this method. And a fractal dimension of $D = 3.0$ corresponds to a uniform sphere.

2.1.2 Stellar Masses

The remaining particles are given stellar masses, which are sampled from a Maschberger initial mass function (Maschberger, 2013):

$$m(u) = \mu \left[[u \; G \; m_u \; - G(m_l) \; + G(m_l)]^{\frac{1}{1-\beta}} - 1 \right]^{\frac{1}{1-\alpha}} \tag{2.1}$$

where $\mu = 0.2$ M$_\odot$, u is a random number between 0 and 1, $\beta = 1.4$, and $\alpha = 2.3$. $G(m_\mathrm{u})$ and $G(m_\mathrm{l})$ are calculated using Equation 2.2, where m_u and m_l correspond to the upper and lower stellar mass limits, respectively:

$$G(m) = \left[1 + \left(\frac{m}{\mu}\right)^{1-\alpha}\right]^{1-\beta} \tag{2.2}$$

Here, we adopt stellar mass limits of $m_\mathrm{u} = 50$ M$_\odot$ and $m_\mathrm{l} = 0.1$ M$_\odot$.

Assigning stellar masses randomly in this way results in no initial mass segregation.

2.1.3 Velocity Distribution

Stellar velocity substructure is also included to reflect observations of star-forming regions which suggest that stars that are closer together have more similar velocities, as discussed in Section 1.4.3. The region is then scaled to produce the chosen virial ratio.

The velocity substructure is generated using the method from Goodwin & Whitworth (2004), as follows:

(i) The first parent particle has its velocity drawn from a Gaussian with a mean of zero.

(ii) Every particle after that has the velocity of its parent plus an additional random velocity component. This additional component is drawn from the same Gaussian and multiplied by $\left({}^{1}/_{N_\mathrm{div}}\right)^{g}$, where g is the number of the generation that the particle was produced in. This results in the additional components being smaller on average with each successive generation of particles.

(i) The velocities are then scaled so that the region has the required virial ratio $\alpha = T \,/\, |\Omega|$, where T is the total kinetic energy of the region, and Ω is the total potential energy.

In this thesis, virial ratios of $\alpha = 0.3$, and 1.5 are used. Where regions with $\alpha = 0.3$ are initially sub-virial and in cool-collapse, and regions with $\alpha = 1.5$ are initially super-virial and expanding.

2.1.4 Randomness

The box-fractal method uses probability to build up the stellar spatial and velocity distributions. This means that a fractal that has been initialised with a different random number seed will produce a statistically identical, but visually different, fractal structure. These statistically identical fractals can appear very different visually and lead to statistical variance within the results (Allison, et al., 2010; Parker & Goodwin, 2012).

The statistical variance can be overcome by running multiple simulations of the same initial conditions, but using a different random number seed for each. This random number seed affects both the spatial and velocity fractal structure as well as the mass function sampling. We refer to each of these simulations as a different *realisation* of the same initial conditions. Each realisation is statistically identical in terms of the fractal dimension and input variables e.g. cluster size, number of stars, virial ratio.

The more stars in a simulation, the fewer realisations need to be run in order to build a reliable statistical picture of the results (Adams, et al., 2006). And previous similar studies suggest that it is sufficient to run simulations of 20 realisations of each set of initial conditions (Parker & Goodwin, 2012; Parker, et al., 2014). Each of these simulations are statistically identical, with the same initial conditions but with different random number seeds used to initialise the positions, velocities, and masses of the stars.

2.2 *N*-Body Evolution

Once the initial conditions have been set-up, the simulations are evolved using *N*-body simulations. *N*-body simulations are a class of numerical methods that are used throughout astronomy to study the dynamical evolution of astrophysical systems (Aarseth, 2003). These numerical methods are used because they solve the *N*-body problem, which has no analytical solutions (Aarseth, 2003). To do this, *N*-body simulation propagate the motion of $N > 2$ bodies due to their mutual gravity. In this thesis we evolve clusters for 10 Myr, as this is the timescale over which most dynamical evolution occurs and clusters disperse.

2.2.1 Basic *N*-Body Method

N-body methods simulate the motions of a group of bodies that are moving under the influence of their mutual gravity. To do this, the bodies are treated as point mass particles and their continuous movements are approximated as discrete steps in time. The position, $\boldsymbol{r}$, and velocity, $\boldsymbol{v}$, of each body is calculated after each timestep, dt.

In a basic *N*-body simulation, Equation 2.3 is first used to calculate the total acceleration of body i due to the $j = 1$ to N other bodies:

$$\boldsymbol{a}_i = -\sum_{j=1, j\neq i}^{n} \frac{Gm_j}{\boldsymbol{r}_{ij}^2}\boldsymbol{r} \qquad 2.3$$

where G is the gravitational constant, m_j is the mass of body j, $\boldsymbol{r}_{ij}$ is the distance between bodies i and j, and $\boldsymbol{r}$ is the unit vector in the direction of $\boldsymbol{r}_{ij}$.

Together with the known positions and velocities from the previous timestep, the acceleration (and its first time derivative, if needed) can then be used to calculate the new position, $\boldsymbol{r_1}$, and velocity, $\boldsymbol{v_1}$. This is done using the Taylor expansions in Equations 2.4 and 2.5 for every body in each dimension:

$$\boldsymbol{r}_1 = \boldsymbol{r}_0 + \boldsymbol{v}_0 dt + \frac{1}{2}\boldsymbol{a}_0 dt^2 + \frac{1}{6}\boldsymbol{a}_0 dt^3 + \frac{1}{24}\boldsymbol{a}_0 dt^4 + \cdots \qquad 2.4$$

$$\boldsymbol{v}_1 = \boldsymbol{v}_0 + \boldsymbol{a}_0 dt + \frac{1}{2}\boldsymbol{a}_0 dt^2 + \frac{1}{6}\boldsymbol{a}_0 dt^3 + \frac{1}{24}\boldsymbol{a}_0 dt^4 + \cdots \qquad 2.5$$

where the subscripts 1 and 0 denote the new and previous timestep's values, respectively.

Higher accuracies can be achieved by using both smaller timesteps and calculating Equations 2.4 and 2.5 to higher orders of *dt*. However, this becomes very computationally expensive beyond second order, as higher order derivatives of $\boldsymbol{a}$ need to be calculated. This is problematic, because terms beyond dt^2 are needed to achieve the accuracies that are necessary for large simulations over longer timescales. This basic method is therefore not feasible. Instead, other methods must be used to reach higher levels of accuracy in more efficient ways. Different software packages achieve this using different methods.

2.2.2 Software Packages

There are two main *N*-body software packages currently used in the field of star and planet formation: the `NBODY` series of codes (see Aarseth, 1999, for a review) and the `kira` N-body integrator within `Starlab` (McMillan & Hut, 1996; Portegies Zwart, et al., 1998; Portegies Zwart, et al., 2001). Both use a fourth order, block-time-step, Hermite predict-evaluate-correct scheme to achieve a high accuracy of results in an efficient way (Anders, et al., 2009). This method is broken down and outlined in the following section.

Despite both using the same scheme, there are differences in the implementation of the algorithms between `NBODY` and `Starlab`. Anders et al. (2009; 2012) show that the results from both packages are generally consistent with each other. However, the energy conservation within `NBODY` is significantly worse than that of `Starlab` during the sub-virial collapse of a region's core (Anders, et al., 2009). We therefore choose to use the `kira` integrator within `Starlab`.

2.2.3 The Kira Integrator

N-Body Units

Before the simulation is run, all of the initial conditions are converted into *N*-body units. *N*-body units are a system of units that are used internally within *N*-body programmes across many fields of astronomy (Heggie & Mathieu, 1986). They are used only within the code in order to improve the accuracy and efficiency (Heggie & Mathieu, 1986).

In N-Body units $G = 1$, $M_{\mathrm{tot}} = 1$, and E_{tot} = -1/4, where M_{tot} is the total mass of the system and E_{tot} is the total initial energy of the system (Heggie & Mathieu, 1986). The transformations for the mass, length, and time units are then $[M] = M_{\mathrm{tot}}$, $[L] = -GM_{\mathrm{tot}}^2/4E_{\mathrm{tot}}$, and $[T] = GM^{5/2}/\ -4E\ ^{3/2}$, respectively (Heggie & Mathieu, 1986).

This choice of units means that many repeated operations can be removed from the algorithm, for example, multiplying by G, as this is now simply multiplying by 1. Meanwhile, many other values are now of order 1, which means that their values can be stored to a higher accuracy. This is because numbers are stored on a computer in scientific notation, with each digit of the number and its exponent sorted as binary numbers. So, decreasing the number of digits used for the exponent leaves more space available in memory for extra digits of the number itself. This therefore increases the number of significant figures that a number can be stored to and the accuracy of the code itself.

The Hermite Predictor-Corrector

Once the initial conditions have been converted to N-body units, the simulation is evolved using the Hermite predictor-corrector scheme.

In the Hermite predictor-corrector scheme (Makino & Aarseth, 1992; Anders, et al., 2009), Taylor series expansions are used to predict approximated values of $\boldsymbol{r}$, and $\boldsymbol{v}$ for all of the particles. A mathematical method called Hermite interpolation is then used to correct these values for a subset of particles which need to be evolved more accurately in order to preserve the accuracy of the simulation.

First, at the beginning of each timestep, the Taylor expansions given in Equations 2.4 and 2.5 are used to predict the position and velocity, $\boldsymbol{r}_{1,\mathrm{p}}$ and $\boldsymbol{v}_{1,\mathrm{p}}$ of every particle. This is done using the known values of $\boldsymbol{r}_0$, $\boldsymbol{v}_0$, $\boldsymbol{a}_0$ and $\boldsymbol{a}_0$ from the previous timestep up to the term containing $\boldsymbol{a}$, as shown in Equations 2.6 and 2.7:

$$\boldsymbol{r}_{1,\mathrm{p}} = \boldsymbol{r}_0 + \boldsymbol{v}_0 dt + \frac{1}{2}\boldsymbol{a}_0 dt^2 + \frac{1}{6}\boldsymbol{a}_0 dt^3, \qquad 2.6$$

$$\boldsymbol{v}_{1,\mathrm{p}} = \boldsymbol{v}_0 + \boldsymbol{a}_0 dt + \frac{1}{2}\boldsymbol{a}_0 dt^2. \qquad 2.7$$

This is the predict stage, which is done for all of the stars in the simulation.

The values of $\boldsymbol{a}_1$ and $\boldsymbol{a}_1$ are then calculated directly using Equation 2.8 and 2.9 with the predicted position and velocity values. A softening parameter, ϵ, is used in the denominators of Equation 2.8 and 2.9. This is chosen to be a very small number, and its purpose is to prevent the accelerations from approaching infinity during very close approaches. This is the evaluate stage.

$$\boldsymbol{a}_1 = -\sum_{j=1,j\neq i}^{n} Gm_j \frac{\boldsymbol{r}_{ij,\mathrm{p}}}{\left(r_{ij,\mathrm{p}}^2 + \epsilon^2\right)^{3/2}} \qquad 2.8$$

$$\boldsymbol{a}_1 = -\sum_{j=1,j\neq i}^{n} Gm_j \left[\frac{\boldsymbol{v}_{ij,\mathrm{p}}}{\left(r_{ij,\mathrm{p}}^2 + \epsilon^2\right)^{3/2}} + \frac{3(\boldsymbol{v}_{ij,\mathrm{p}} \cdot \boldsymbol{r}_{ij,\mathrm{p}})\, \boldsymbol{r}_{ij,\mathrm{p}}}{\left(r_{ij,\mathrm{p}}^2 + \epsilon^2\right)^{5/2}}\right] \qquad 2.9$$

The corrector stage then uses a polynomial, given in Equation 2.10, to find $\boldsymbol{a}_0$ and $\boldsymbol{a}_0$.

$$\boldsymbol{a}_1 = \boldsymbol{a}_0 + \boldsymbol{a}_0 dt + \frac{1}{2}\boldsymbol{a}_0 dt^2 + \frac{1}{6}\boldsymbol{a}_0 dt^3 \qquad 2.10$$

Hermite interpolation of this polynomial yields Equation 2.11 for $\boldsymbol{a}_0$ and Equation 1.10 for $\boldsymbol{a}_0$. These require known values of $\boldsymbol{a}_0$ and $\boldsymbol{a}_0$ from the previous timestep, as well as $\boldsymbol{a}_1$ and $\boldsymbol{a}_1$ as calculated in Equations 2.8 and 2.9.

$$\boldsymbol{a}_0 = \frac{-6\ \boldsymbol{a}_0 - \boldsymbol{a}_1\ \ - dt\ \ 4\boldsymbol{a}_0 + 2\boldsymbol{a}_1}{dt^2} \qquad 2.11$$

$$\boldsymbol{a}_0 = \frac{12\ \boldsymbol{a}_0 - \boldsymbol{a}_1\ \ + 6dt\ \ \boldsymbol{a}_0 + \boldsymbol{a}_1}{dt^3} \qquad 2.12$$

The correction values of $\boldsymbol{a}_0$ and $\boldsymbol{a}_0$ are then added to the predicted positions and velocities, giving the final corrected values of $\boldsymbol{r}_1$ and $\boldsymbol{v}_1$:

$$\boldsymbol{r}_1 = \boldsymbol{r}_{1,\mathrm{p}} + \frac{1}{24}\boldsymbol{a}_0 dt^4 + \frac{1}{120}\boldsymbol{a}_0 dt^5 \tag{2.13}$$

$$\boldsymbol{v}_1 = \boldsymbol{v}_{1,\mathrm{p}} + \frac{1}{6}\boldsymbol{a}_0 dt^3 + \frac{1}{24}\boldsymbol{a}_0 dt^5 \tag{2.14}$$

Block Timestep

To consistently achieve the desired levels of accuracy across the simulation, different timesteps must be used for different particles. This is because a particle with a higher acceleration needs a smaller timestep in order to calculate its motion accurately. Ideally, each particle would be assigned its own individual timestep. However, the efficiency of the simulation is improved if particles are grouped together with shared timesteps, and these ‘blocks’ of particles are evolved together (Makino, 1991).

`Kira` uses this block-timestep method (Portegies Zwart, et al., 2001). Within `kira` every particle is assigned to a timestep ‘rung’, illustrated in Figure 2.1 (Dehnen & Read, 2011), based on its predicted acceleration and the level of accuracy needed (Anders, et al., 2009). Particles on the higher rungs have larger timesteps than the particles on lower rungs, where the possible timesteps are factors of two of each other. The particles on the lower rungs, with smaller and more accurate timesteps, also have their motions propagated using higher order Taylor expansions (Anders, et al., 2009), as described in the previous sub-section.

Until the end of the largest timestep, Δt_0 in Figure 2.1, the positions of some of the particles are unknown even though this information is needed to propagate the particles on the lower rungs that have smaller timesteps. In these cases, the unknown positions are estimated using low order Taylor expansion (Makino, 1991). This is where the efficiency is gained with the block-timestep method, as the positions of the other particles only needs to be predicted at times when a whole ‘block’ of particles is evolved (Makino, 1991; Anders, et al., 2009). If every particle had its own individual timestep, this would have to be done for every time that a single particle was evolved.At the end of the largest timestep, the particles are synchronised. However, if necessary, particles can also periodically move between timestep rungs when the timesteps align with each other, shown as red arrows in Figure 2.1 (Dehnen & Read, 2011).

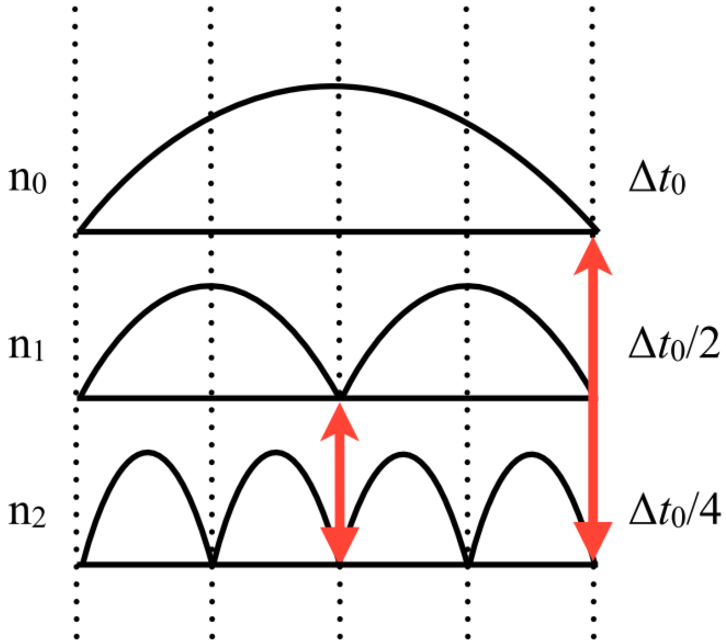

Figure 2.1 Schematic of the block-timestep used within kira (Dehnen & Read, 2011).

Binary Systems

In Chapter 4 we run simulations where half of the stars have planets. Within `Starlab` these are treated the same as star-star binary systems, except that the binary companion is of planetary mass.

The motions of these binary systems are propagated differently than non-binary systems (Portegies Zwart, et al., 2001; Anders, et al., 2009). This is because the use of timesteps small enough to accurately propagate the motion of a binary system would make `kira` infeasibly slow. Such small timesteps would also lead to numerical rounding errors compounding, jeopardising the accuracy if the simulation.

The forces that a particle in a binary system experience can be broken up into two parts: the dominant force from the particle's binary companion, and the smaller, perturbative force from particles in the rest of the system (Portegies Zwart, et al., 2001). This allows binary systems to be categorised based on their 'perturbation ratio' and treated differently to other particles in the simulation. This strategy allows the required accuracies to be achieved without slowing down the simulation an unreasonable amount (Anders, et al., 2009).

The perturbation ratio is a measure of how much a binary companion is perturbed by other local bodies, and is calculated as the ratio of the energy that an external perturbation imparts on the system to the binding energy of the binary itself (Anders, et al., 2009). Most close binary systems are unlikely to be perturbed by a passing star or planet because the binding energy is much larger than the energy added by an encounter. This means that they effectively evolve in isolation (Anders, et al., 2009). These *unperturbed* systems have perturbation ratios of $<10^{-6}$, allowing their motions to be solved analytically as two-body motion using Kepler's equations (Portegies Zwart, et al., 2001; Anders, et al., 2009). *Mildly perturbed* systems, with a perturbation ratio of 10^{-6} to 10^{-5}, are propagated using a different algorithm (Mikkola & Aarseth, 1998), which is more appropriate in this energy regime and involves artificially slowing down the motion of the binary and then compensating for the change in motion (Portegies Zwart, et al., 2001). Finally, for *strongly perturbed* binaries, each particle is treated individually, and their motion is propagated directly using the Hermite method previously described (Portegies Zwart, et al., 2001).

Output of information

Before the simulation is run, a snapshot interval is chosen. It is only at every snapshot interval that information about the bodies in the simulation is output. It is this information that is used for analysis, and for the work in this thesis information is output every 0.01 Myr.

`Kira` is also able to include and output information about stellar and binary evolution throughout the simulation. However, we do not use this feature for the work included in this thesis.

Chapter 3

The Dynamical Evolution of Fractal Structures in Star-Forming Regions

The work in this chapter has been published in the Monthly Notices of the Royal Astronomical Society as Daffern-Powell & Parker (2020).

3.1 Summary

The Q-parameter is used extensively to quantify the spatial distributions of stars and gas in star-forming regions as well as older clusters and associations. It quantifies the amount of structure using the ratio of the average length of a minimum spanning tree, $\overline{m}$ to the average length within the complete graph, $\overline{s}$. The interpretation of the Q-parameter often relies on comparing observed values of Q, $\overline{m}$, and $\overline{s}$ to idealised synthetic geometries, where there is little or no match between the observed star-forming regions and the synthetic regions.

We measure Q, $\overline{m}$, and $\overline{s}$ over 10 Myr in N-body simulations which are compared to IC 348, NGC 1333, and the ONC. For each star-forming region we set up simulations that approximate their initial conditions for a combination of different virial ratios and fractal dimensions. We find that the dynamical evolution of idealised fractal geometries can account for the observed Q, $\overline{m}$, and $\overline{s}$ values in nearby star-forming regions. In general, an initially fractal star-forming region will tend to evolve to become more smooth and centrally concentrated. However, we show that the initial conditions, as well as where the edge of the region is defined, can cause significant differences in the path that a star-forming region takes across the $\overline{m}$-$\overline{s}$ plot as it evolves.

We caution that the observed Q-parameter should not be directly compared to idealised geometries. Instead, it should be used to determine the degree to which a star-forming region is either spatially substructured or smooth and centrally concentrated. Through this, the Q-parameter can be a valuable tool for investigating the substructured nature of star-forming regions, and the effects that this can have on the stars and planets within them.

3.2 Introduction

As discussed in Chapter 1, the relatively high stellar densities in star-forming regions can have significant effects on star and planet formation. In particular, star-forming regions have a hierarchical spatial substructure, that may be fractal in nature. Areas of substructure tend to have relatively high stellar densities compared to the region as a whole, which can cause them to have more of an effect on star and planet formation. It is therefore important to be able to quantify the substructured nature of star-forming regions. This allows simulations to be more usefully compared to observations and each other, and therefore enables a better understanding of the effects that these environments can have.

There are several methods that can be used to measure and quantify substructure. These methods can be used to identify the star-forming regions themselves as well as any substructure that exists on different scales within them (Schmeja, 2011). The most basic method is a stellar density map, where a region is split into bins and the number of stars in each bin is compared in order to identify areas that are significantly over-dense (Schmeja, 2011).

More complex methods include the nearest neighbour density, which estimates the local density around each star (Gutermuth, et al., 2009; Schmeja, 2011; Buckner, et al., 2019); the angular dispersion parameter, which divides a region into segments and compares their stellar densities (Da Rio, et al., 2014; Jaehnig, et al., 2015); the two-point correlation function, which identifies pairs of stars that are closer than average (Gomez, et al., 1993; Larson, 1995; Gouliermis, et al., 2014); and the minimum spanning tree which is used for the work in this chapter.

The minimum spanning tree is a well-established and widely used[6] statistical method (Gower & Ross, 1969), which in astronomy it is commonly used to identify substructure (Cartwright & Whitworth, 2004; Gutermuth, et al., 2009; Kirk & Myers, 2011; Schmeja, 2011). In a minimum spanning tree, all of the stars in a region are connected such that the total length of all the edges (i.e., connections) is minimised and there are no closed loops (Gower & Ross, 1969). Examples

---

[6] Minimum spanning trees have been used throughout at least the past century. Applications are diverse and include evolutionary trees, town planning, and the travelling salesman problem (Gower & Ross, 1969).

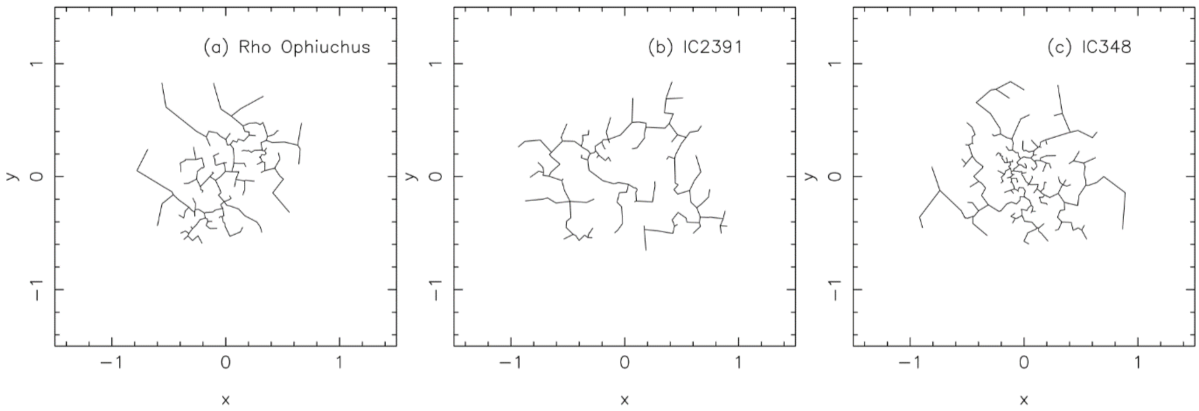

Figure 3.1 Minimum spanning trees for the observed members of Rho Ophiuchus, IC 2391, and IC 348. Taken from Cartwright & Whitworth (2004), their Figure 4. The scale of the axes for each region is such that the mean position of all the stars is centred, and the distance from this centre to the outermost star is 1.

lkmjnof minimum spanning trees for three star clusters are shown in Figure 3.1 (Cartwright & Whitworth, 2004). Sub-clusters and areas of substructure can then be identified by removing edges which are longer than a chosen length (Gutermuth, et al., 2009; Kirk & Myers, 2011; Schmeja, 2011). This leaves islands of stars which can be seen as the sub-clusters or areas of substructure. In terms of quantifying the amount substructure, the mean edge length of all of the connections, $\overline{m}$, can be used to quantify the extent to which a group of stars is substructured or centrally concentrated (Cartwright & Whitworth, 2004).

However, $\overline{m}$ alone is unable to distinguish between substructured and smooth centrally concentrated regions, even though these are dynamically different forms of substructure (Goodwin & Whitworth, 2004). To overcome this, the Q-parameter was introduced by Cartwright & Whitworth (2004), and further developed by Lomax et al. (2011), and Jaffa et al. (2017). The Q-parameter is calculated using Equation 3.1:

$$Q = \frac{\overline{m}}{\overline{s}} \qquad 3.1$$

Where, $\overline{s}$ is the mean edge length of the star-forming region's complete graph, in which edges are drawn from every star to every other star (Cartwright, 2009).

As $\overline{m}$ and $\overline{s}$ are two different measures, they scale differently. This enables the Q-parameter to distinguish between substructured and centrally concentrated regions, as it combines $\overline{m}$ and $\overline{s}$. The Q-parameter therefore both gives a measure of the amount of substructure and distinguishes ‘clumpy’/fractal substructured regions from those that are smooth and centrally concentrated. It does this in in a single dimensionless number, where regions with $Q > 0.8$ have a smooth radial density profile that is more centrally concentrated with higher Q, while regions with $Q < 0.8$ have a larger amount of substructure with decreasing Q. Because of this, the Q-parameter has been used extensively for investigating substructure in both simulated and observed regions (e.g. Schmeja & Klessen, 2006; Bastian et al., 2009; Sánchez & Alfaro, 2009; Delgado et al., 2013; Parker et al., 2014; Parker & Dale, 2015; Hetem & Gregorio-Hetem, 2019).

Cartwright (2009) showed that using a plot of $\overline{m}$ vs $\overline{s}$ provides more information than $\boldsymbol{Q}$ alone. These plots contain more information than a single number, and are therefore more sensitive to distinguishing between different properties. The interpretation of the $\overline{m}$-$\overline{s}$ plot relies on comparing the observed or simulated values to sets of idealised geometries, which are usually either box fractals or centrally concentrated spheres.

However, values of $\overline{m}$ and $\overline{s}$ for observed star-forming regions often do not occupy the same areas of the $\overline{m}$-$\overline{s}$ plot as idealised box fractals and smooth centrally concentrated regions (Lomax, et al., 2018). This is shown in Figure 3.2, where a clear gap can be seen in between the box fractal regions, in purple, and those with a smooth radial density profile, in yellow and green. However, this area is still populated by observed regions, for example, Cha I and Taurus. It has been suggested that this is a shortcoming of the Q-parameter method, as it can be seen to imply that $\overline{m}$ and $\overline{s}$ are not able to characterise observed regions and/or that these idealised geometries are not reasonable approximations for star-forming regions (Lomax, et al., 2018).

In this chapter we therefore use the $\overline{m}$-$\overline{s}$ plot to test whether observed star-forming regions are consistent with having evolved from fractal geometries, or whether there is a problem with the ability of the Q-parameter method to quantify substructure. We do this by simulating the dynamical evolution of IC348, NGC 1333, and ONC analogues with a range of initial conditions. We then investigate their evolution using the Q-parameter method to see whether they evolve into the $\overline{m}$-$\overline{s}$ plot gap over time.

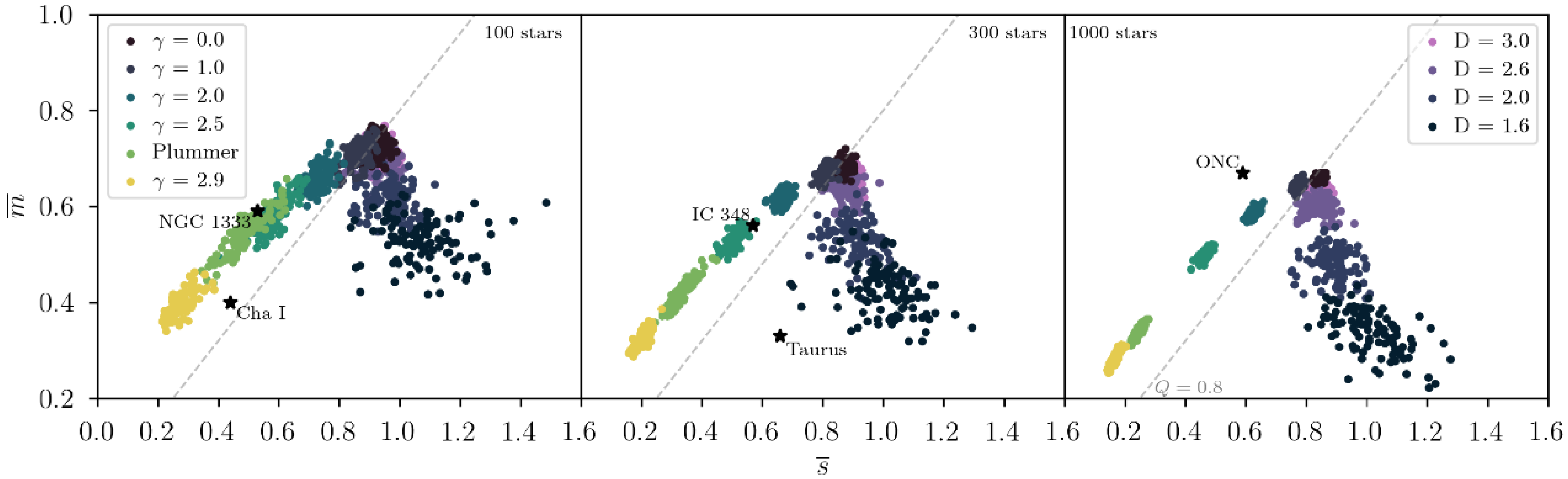

Figure 3.2 A comparison between the areas of the $\overline{m}$-$\overline{s}$ plot that are occupied by observed regions vs. idealised geometries. For the observed regions, values of $\overline{m}$ and $\overline{s}$ for IC 348 (Parker & Alves de Oliveira, 2017), NGC 1333 (Parker & Alves de Oliveira, 2017), the ONC (data from Hillenbrand, 1997), Cha I (data from Luhman, 2007), and Taurus (data from Luhman, 2007), are marked by black stars. For the idealised geometries, box fractal regions and those with a smooth radial density profile are shown as coloured points. 100 different realisations of each type of idealised region are shown. These regions were created with either 100, 300, or 1000 stars, as shown in the 3 panels. The observed regions are therefore shown on the panel that approximately corresponds to their observed number of stars. Fractal dimensions of $D = 3.0$, 2.6, 2.0, and 1.6 are shown, with the regions becoming more substructured with lower values of D. For the centrally concentrated regions, a Plummer Sphere (Plummer, 1911) and regions with radial density profile exponents of $\gamma = 0.0$, 1.0, 2.0, 2.5 and 2.9 are shown, with the regions becoming more centrally concentrated with higher values of γ. A grey dashed line indicates where $Q = 0.8$. A gap can be seen between the box fractals and radial density profiles which is occupied by observed regions, for example Cha I and Taurus, meaning that these idealised geometries do not describe the observed substructure in these regions.

3.3 Methods

We simulate regions that approximate IC 348, NGC 1333, and the ONC using the `kira` N-body integrator, as discussed in Chapter 2 (Portegies Zwart, et al., 1999; Portegies Zwart, et al., 2001). Table 3.1 shows the initial conditions for each set of simulations.

With regards to the number of stars simulated, column 3 of Table 3.1, Q is dependent on the number of points in the distribution (see Parker, 2018, his Fig. A2), and is also significantly affected by the inclusion of foreground and background stars. It is therefore important to only include stars with a high membership probability in the analysis of observational data, and to run simulations using an equal number of stars to this observational sample to allow for a direct comparison.

For example, for the ONC, there are 929 stars with a >90% membership probability (Hillenbrand, 1997; Hillenbrand & Hartmann, 1998; Reggiani, et al., 2011), we therefore run simulations with, $N_* = 929$. Similarly, for IC 348 and NGC 1333, there are respectively 459 and 162 stars with membership confirmed by Luhman et al. (2016). This inevitably means that some genuine members may be excluded from the analysis, with fainter, lower mass members being disproportionately affected. However, it is not expected that Q varies as a function of stellar mass such that it would be affected by this (Parker, et al., 2014). It is therefore a fairer comparison to the data to use the lower values of N_* adopted here, even for clusters which likely have uncatalogued members, as may be the case for the ONC (e.g. Forbrich et al., 2016).

We infer initial radii, R, from comparing the amount of mass segregation in simulations to the observed levels of mass segregation in each of the ONC (Allison, et al., 2010; Allison & Goodwin, 2011), IC 348, and NGC 1333 (Parker & Alves de Oliveira, 2017). Parker et al., 2014 show that the level of mass segregation in a star-forming region is a proxy for the amount of dynamical evolution that has taken place, which in turn places constraints on the initial density (and therefore radius). If future observations add significant numbers of extra stars (i.e. a factor of two more) to the regions' censuses, then our analyses would need to be repeated with new simulations better tailored to the observed numbers of stars.

Table 3.1 The ages and initial conditions used for each set of simulations. Columns 2 and 3 contain the current observed ages and number of stars for IC 348 (Luhman, et al., 2016), NGC 1333 (Luhman, et al., 2016), and the ONC (Hillenbrand, 1997; Hillenbrand & Hartmann, 1998; Reggiani, et al., 2011). Column 4 gives the initial radii, R, as inferred from simulations. Columns 5 and 6 show the combinations of fractal dimension, D, and virial ratio, α, used here.

Name	Age/Myr	N_*	R/pc	D	α
IC 348	~3	459	1.5	1.6	0.3
				1.6	1.5
				2.0	0.3
				2.0	1.5
				3.0	0.3
NGC 1333	~1	162	0.5	1.6	0.3
				1.6	1.5
				2.0	0.3
				3.0	0.3
ONC	≈1-4	929	1	1.6	0.3
				1.6	1.5
				2.0	0.3
				3.0	0.3

These radii are combined with different initial fractal dimensions, D, and virial ratios, α. The stellar masses are sampled from a Maschberger IMF (Maschberger, 2013), with minimum and maximum masses of 0.1 $M_{\odot}$ and 50 $M_{\odot}$ respectively.

For each set of initial conditions in Table 3.1, ten realisations are simulated using different random number seeds. Each simulation is evolved for 10 Myr. We do not include stellar evolution or primordial binaries in the simulations.

3.3.1 Determining *Q*

For each simulation, $\overline{m}$ and $\overline{s}$ are calculated every 0.01 Myr, according to the method in Cartwright & Whitworth (2004). For all calculation methods, $\overline{m}$ and $\overline{s}$ were calculated in 2D, to mimic a projection on the sky, allowing a more direct comparison to observations. This was done for different normalisation methods and cut-off radii, as described in the following subsections.

Cut-Off Boundary

Three different membership criteria were used to determine which stars should be included in the calculation of $\overline{m}$ and $\overline{s}$. The first criterion is simply to include all of the stars in the simulation in the analysis. In the second two, cut-off boundaries are used, beyond which stars are excluded from the analysis as they may not be observationally associated with the region based on their distance from its centre. These cut-off radii were chosen to be 5 pc and 3 pc.

Normalisation

Both $\overline{m}$ and $\overline{s}$ must be normalised with respect to the region's size. For $\overline{s}$, the mean edge length of the complete graph is normalised to the region's radius (Cartwright & Whitworth, 2004). For $\overline{m}$, the mean edge length of the minimum spanning tree is normalised with respect to the region's area (Cartwright & Whitworth, 2004), by dividing by a factor of:

$$\frac{\sqrt{NA}}{N-1} \tag{3.2}$$

where N is the number of points, and A is the region's projected area on the sky.

The characteristic area of a region can either be taken to be that of a circle, or a convex hull - an enclosure drawn around the outermost stars, so that all of the stars are enclosed and the total length of the edges of the enclosure is minimised. Here, $\overline{m}$ and $\overline{s}$ are calculated using both circular and convex hull normalisations for comparison, as the normalisation can have a significant effect on the results (Parker, 2018).

For the standard circular normalisation, the area is that of a circle with radius drawn from the region's centre to its outermost star (Cartwright & Whitworth, 2004). For the convex hull normalisation, we use the method introduced by (Schmeja & Klessen, 2006), where $\overline{m}$ is normalised to the area of the convex hull, and $\overline{s}$ is normalised to the radius of a circle that has the same area as that convex hull.

3.4 Results & Discussion

Our main results are shown in Figure 3.3 and Figure 3.6 to Figure 3.10. These show the evolutionary tracks of our simulations across the $\overline{m}$-$\overline{s}$ plot, along with the current observed values of $\overline{m}$ and $\overline{s}$ for their corresponding regions shown as a yellow star. We discuss these figures in turn in the following subsections.

3.4.1 IC 348

D = 2.0, α = 0.3

Figure 3.3 shows the evolution of each realisation of the IC 348-like $D = 2.0$, $\alpha = 0.3$ simulations, for all three region membership criteria and both normalisation methods.

Panels (a) and (b) show that, when all stars are used in the analysis, the overall evolution of each realisation is a rapid (~0.1 Myr) initial drop in $\overline{m}$, followed by a movement towards lower values of $\overline{m}$ and often s. This movement crosses the gap, shown in Figure 3.2, demonstrating that these regions can populate the $\overline{m}$-$\overline{s}$ plot gap as they dynamically evolve.

A comparison to Figure 3.4, which shows the spatial distribution of one realisation as it evolves over the 10 Myr simulation, demonstrates that the initial drop corresponds to the simulated regions becoming more substructured. This is counter-intuitive, as dynamical interactions erase substructure. However, this phase corresponds to the 'clumps' of substructure collapsing on local scales, before the region as a whole has begun to collapse significantly. The reason why this is seen as an increase in substructure by the Q-parameter is best understood visually. Figure 3.4 shows that between 0 to ~1 Myr the region begins to collapse on local scales, and the clumps appear more pronounced as they become smaller and more centrally concentrated - it is this behaviour that is seen as an increase in the degree of substructure.

The subsequent movement towards lower s corresponds to the region as a whole collapsing. Dynamical interactions wipe out substructure on global scales as the clumps are destroyed and the region as a whole becomes smoother and more centrally concentrated. This is seen in the 1-10 Myr panels of Figure 3.4. During this time, each realisation crosses the Q=0.8 boundary in

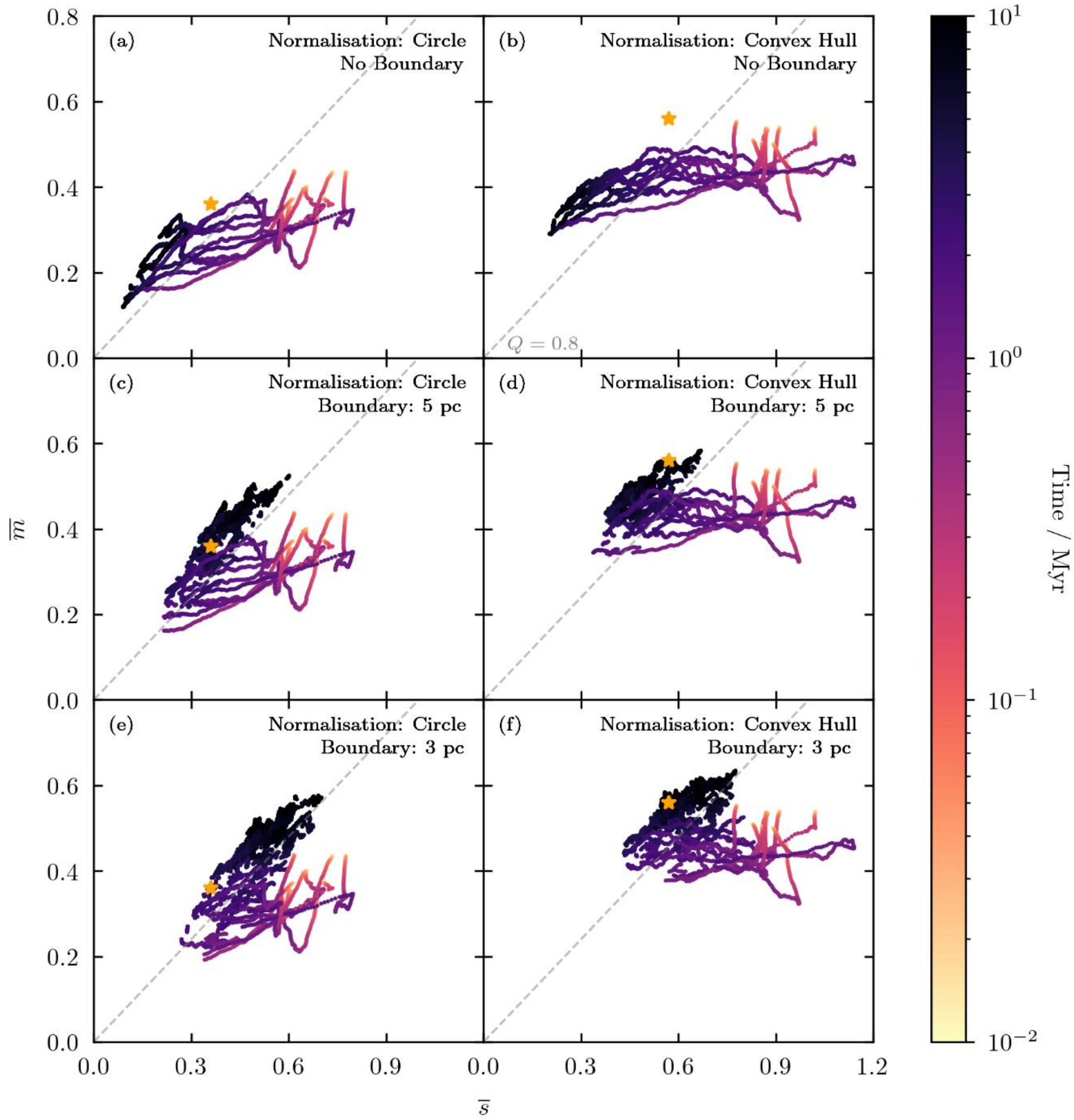

Figure 3.3 Evolution of $\overline{m}$ and $\overline{s}$ over 10 Myr for an IC 348-like star-forming region, with initial D = 2.0 and α = 0.3. Ten realisations of the region are shown for 6 combinations of analysis methods. The observed values of $\overline{m}$ and $\overline{s}$ for IC 348 (age ~3-6 Myr) are shown as a yellow star, and a grey dashed line shows the $Q = 0.8$ boundary between substructured and centrally concentrated distributions. Each realisation crosses the $\overline{m}$-$\overline{s}$ plot gap as they dynamically evolve during the first ~1 Myr.

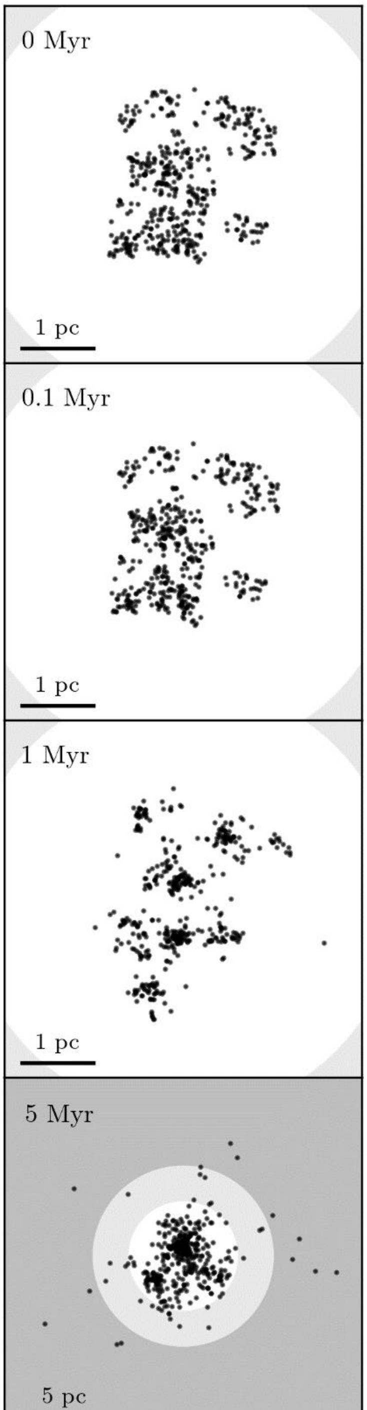

Figure 3.4 The *x*-*y* stellar positions, at five different times, showing the dynamical evolution of one realisation of the IC 348-like star-forming region with initial $D = 2.0$ and $\alpha = 0.3$. Stars are shown as slightly transparent black dots, so that denser areas are more opaque. The area beyond the 5 pc cut-off is shaded dark grey, and the area in between the 5 pc and 3 pc cut-offs is shaded a lighter grey. Initially, between ~0-1 Myr, the individual areas of substructure collapse. This is followed by the region as a whole dynamically interacting, causing it to transition to a centrally concentrated geometry and eject stars.

Figure 3.3, so that all ten ends in the area of the $\overline{m}$-$\overline{s}$ plot that corresponds to a centrally concentrated region with a smooth radial density profile.

When a cut-off boundary is imposed this behaviour changes, as shown in panels (c)-(f) of Figure 3.3. For both a 5 and 3 pc cut-off, each realisation still has an initial drop in $\overline{m}$ up to ~0.1 Myr, followed by a migration towards lower $\overline{s}$. However, this migration stops at ~1 Myr, and the final stage of the regions' evolution is a diagonal increase in $\overline{m}$ and $\overline{s}$. This happens with approximately constant Q, just above the $Q = 0.8$ line, and means that the realisations cross the area of the $\overline{m}$-$\overline{s}$ plot where IC 348 is observed to be. This final stage begins once some of the stars reach the cut-off boundary, as the region expands. This expansion causes $\overline{m}$ and s to increase as the stars within the cut-off get farther apart, and fewer stars are left within it.

Figure 3.5 shows that, after 5 Myr, a 3 pc cut-off begins to exclude some stars which could reasonably be identified as belonging to the region based on their x-y positions, where a 5 pc cut-off does not. However, comparison to Figure 3.3 shows that this does not have a significant effect. For the remaining figures, results are therefore shown with only a 5 pc cut-off.

When the standard circular normalisation is used, compared to a convex hull, each realisation has lower values of $\overline{m}$ and $\overline{s}$. This is because a convex hull will always have a smaller area than the corresponding circle. The area and radius used to normalise $\overline{m}$ and $\overline{s}$ will therefore be higher for the circular normalisation method compared to convex hull normalisation (Parker, 2018).

Effect of Initial Fractal Dimension

Figure 3.6 and Figure 3.7 how the evolution of the IC 348-like simulations differ with fractal dimension. Regions with a fractal dimension of $D = 1.6$ have the maximum amount of initial substructure, and therefore begin clumpier than those with $D = 2.0$ discussed in the previous subsection. A comparison of Figure 3.3 and Figure 3.6 shows that the evolution of the IC 348-like simulations is similar with initial $D = 1.6$ and $D = 2.0$. The $D = 1.6$ realisations begin lower on the $\overline{m}$-$\overline{s}$ plot, due to their larger amount of substructure, but migrate to the same area of the plot before making the upward turn at ~1 Myr.

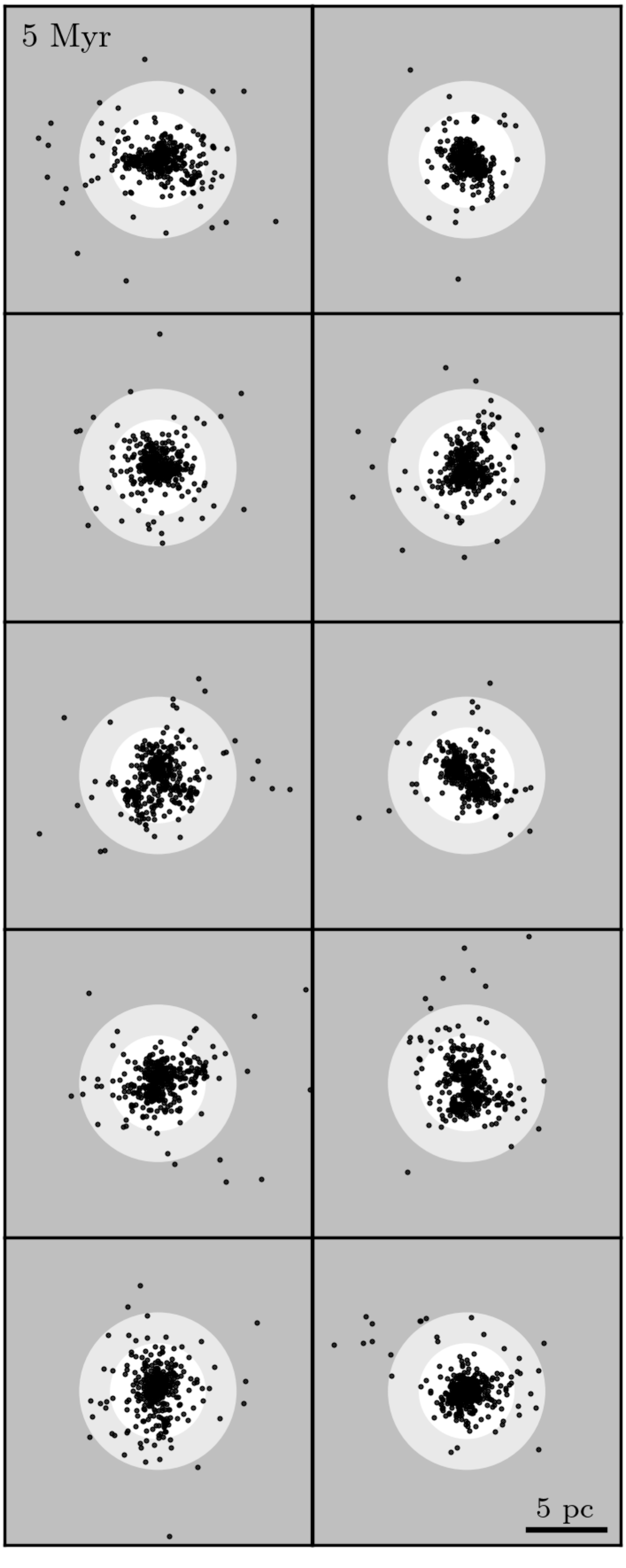

Figure 3.5 The *x*-*y* stellar positions, at 5 Myr, for ten realisations of IC~348-like regions with initial D = 2.0 and α = 0.3. Stars are shown as slightly transparent black dots, so that denser areas are more opaque. The area beyond the 5 pc cut-off is shaded dark grey, and the area in between the 5 pc and 3 pc cut-offs is shaded a lighter grey.

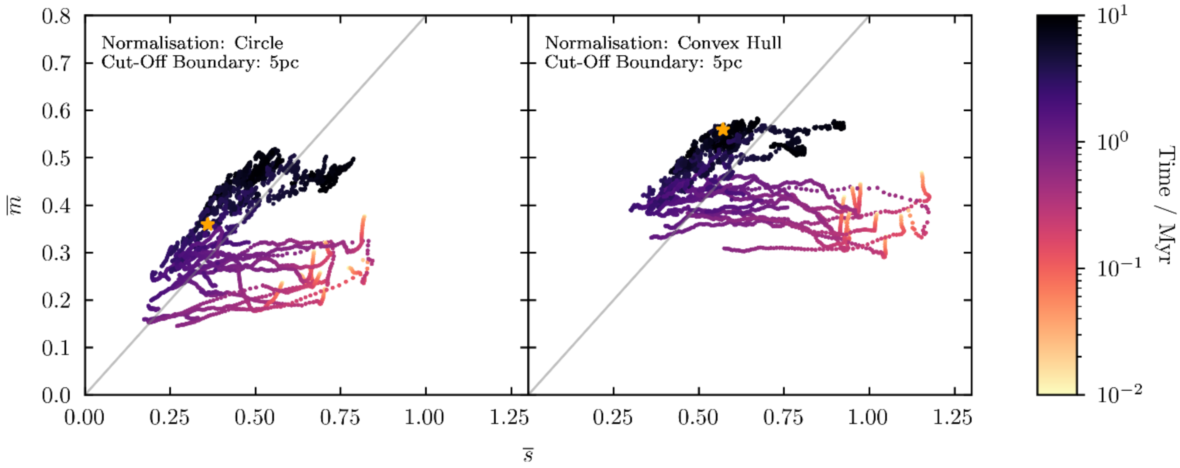

Figure 3.6 Evolution of $\overline{m}$ and $\overline{s}$ over 10 Myr for an IC 348-like region, with initial $D = 1.6$ and $\alpha = 0.3$. Ten realisations of the region are shown for both a circular and convex hull normalisations. The current values of $\overline{m}$ and $\overline{s}$ for IC 348 (age ~3-6 Myr) are shown as a yellow star. The evolution is similar to the corresponding simulations with initial D = 2.0.

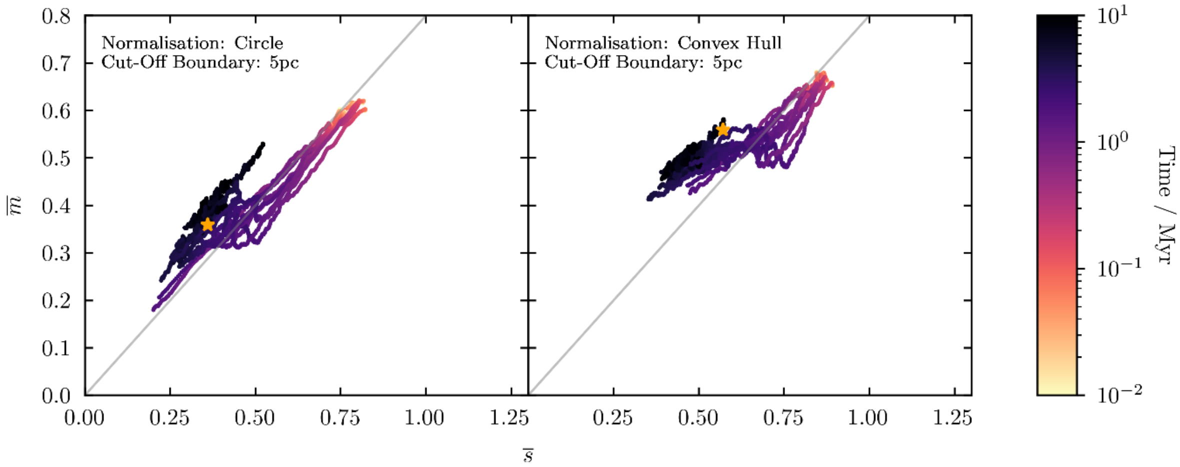

Figure 3.7 Evolution of $\overline{m}$ and $\overline{s}$ over 10 Myr for an IC 348-like region, with initial $D = 3.0$ and $\alpha = 0.3$. Ten realisations of the region are shown for both circular and convex hull normalisations. The current values of $\overline{m}$ and $\overline{s}$ for IC 348 (age ~3-6 Myr) are shown as a yellow star.

Regions with a fractal dimension of $D = 3.0$ are initially smooth and non-substructured. Figure 3.7 shows that these simulations also evolve to the same area of the plot as regions with initial $D = 2.0$ and 1.6, before the upwards turn at ~1 Myr.

In this case, this leads to each realisation initially migrating downward along the $Q = 0.8$ line, corresponding to the regions remaining smooth, but becoming more centrally concentrated up to ~1 Myr as they collapse. They then become less centrally concentrated as they expand past the 5 pc cut-off boundary for the remainder of the simulation.

This means that this set of non-substructured regions do not cross the $\overline{m}$-$\overline{s}$ plot gap during their evolution, and would therefore be unable to explain regions which are observed to lie in the $\overline{m}$-$\overline{s}$ plot gap. However, since IC 348 is currently observed to lie in the smooth and centrally concentrated area of the $\overline{m}$- $\overline{s}$ plot, it is possible that IC 348 had an initially smooth distribution.

Effect of initial virial ratio

Figure 3.8 shows that the evolutionary tracks are a lot less coherent for the initially super-virial $\alpha = 1.5$, $D = 2.0$ IC 348-like simulations. There is still an initial drop in $\overline{m}$ during the first ~0.1 Myr, however there also tends be a significant increase or decrease in $\overline{s}$ during this time which is not seen in the initially sub-virial regions. There is therefore no general trend in the realisations' movements across the $\overline{m}$- $\overline{s}$ plot.

However, these simulations do not significantly cross the $Q = 0.8$ line. This means that the super-virial simulations do not become smooth and centrally concentrated. Instead, they remain substructured throughout the 10 Myr simulated here. This is because these regions immediately expand and therefore there is not enough dynamical mixing to erase the substructure.

Since IC 348 lies above the $Q = 0.8$ line, the $\overline{m}$- $\overline{s}$ plot would suggest that it is not possible for it to have had super-virial initial conditions.

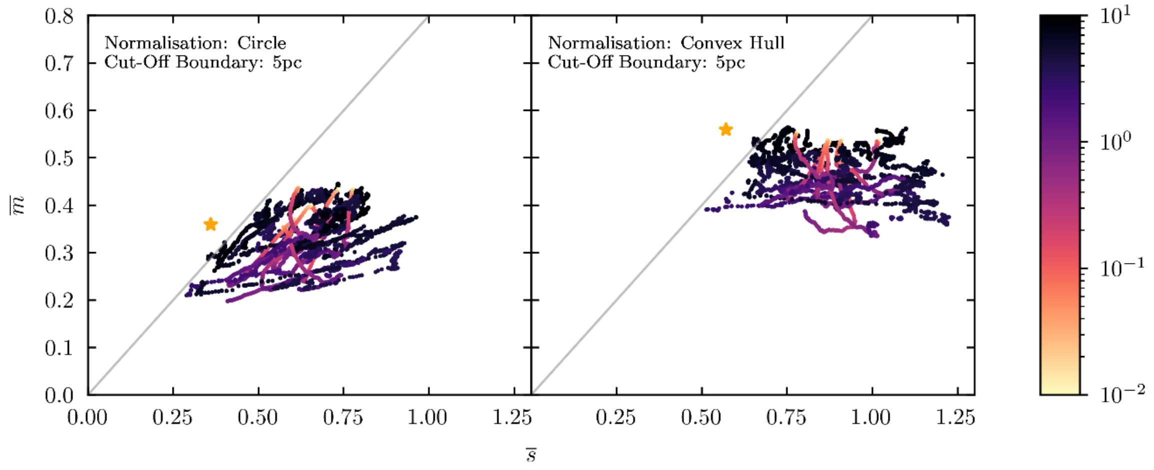

Figure 3.8 Evolution of $\overline{m}$ and $\overline{s}$ over 10 Myr for an IC 348-like region, with initial $D = 2.0$ and $\alpha = 1.5$. Ten realisations of the region are shown for both circular and convex hull normalisations. The current values of $\overline{m}$ and $\overline{s}$ for IC 348 (age ~3-6 Myr) are shown as a yellow star.

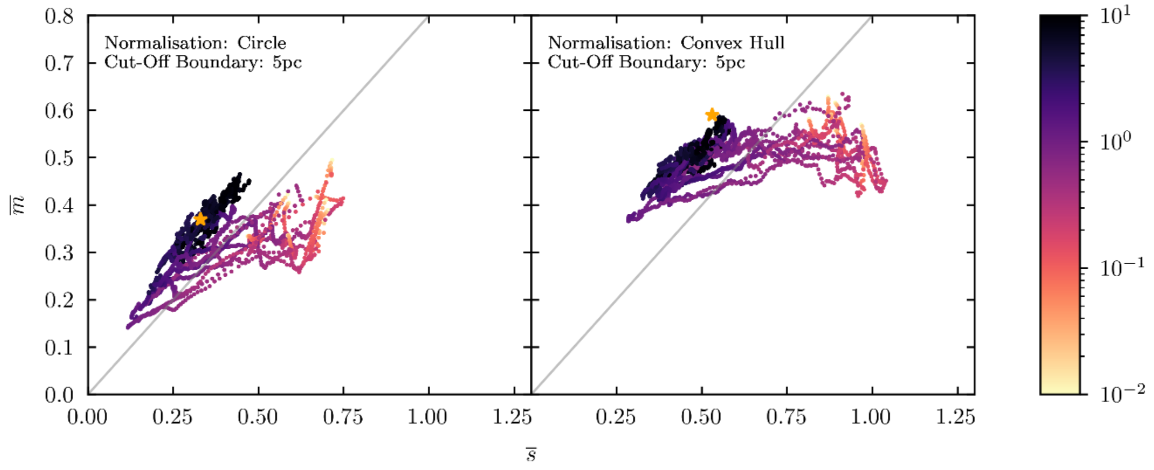

Figure 3.9 Evolution of $\overline{m}$ and $\overline{s}$ over 10 Myr for an NGC 1333-like region, with initial $D = 2.0$ and $\alpha = 0.3$. Ten realisations of the region are shown for both circular and convex hull normalisations. The current values of $\overline{m}$ and $\overline{s}$ for NGC 1333 (age ~1 Myr) are shown as a yellow star. The evolutionary path is similar to the corresponding IC 348 simulations.

Constraints placed on IC 348

All initial conditions with $\alpha = 0.3$ where a cut-off boundary was imposed are consistent with the current observed values of $\overline{m}$ and $\overline{s}$ for IC 348, between ~1-10 Myr.

In terms of initial substructure, both our smooth and substructured initial conditions are consistent with observations of IC 348. However, there is evidence that star-forming regions tend to be initially substructured (Cartwright & Whitworth, 2004; Sánchez & Alfaro, 2009; André, et al., 2010; André, et al., 2014; Kuhn, et al., 2014; Jaehnig, et al., 2015; Arzoumanian, et al., 2019). These results would therefore suggest that IC 348 likely had substructured and sub-virial initial conditions.

3.4.2 NGC 1333

The evolution of each set of NGC 333-like simulations follows the same general migration as their corresponding IC 348-like regions, including an evolution across the $\overline{m}$-$\overline{s}$ plot gap for those that begin substructured. The evolution of the NGC 1333-like region with initial $D = 2.0$ and $\alpha = 0.3$ can be seen in Figure 3.9, which shows the initial drop in $\overline{m}$, followed by a turn-over at ~1 Myr in the same region of the plot as for the IC 348-like regions.

Constraints placed on NGC 1333

Like IC 348, NGC 1333 is observed to lie above the $Q = 0.8$ line. Our simulations are therefore inconsistent with NGC 1333 having been initially highly super-virial ($\alpha = 1.5$) if it formed substructured (Cartwright & Whitworth, 2004; Sánchez & Alfaro, 2009; André, et al., 2010; André, et al., 2014; Kuhn, et al., 2014; Jaehnig, et al., 2015; Arzoumanian, et al., 2019).

Figure 3.9 shows some of the realisations that are substructured and sub-virial to be consistent with the current observed values of $\overline{m}$ and $\overline{s}$ for NGC 1333 at ages greater than ~1 Myr - slightly older than NGC 1333 is thought to be.

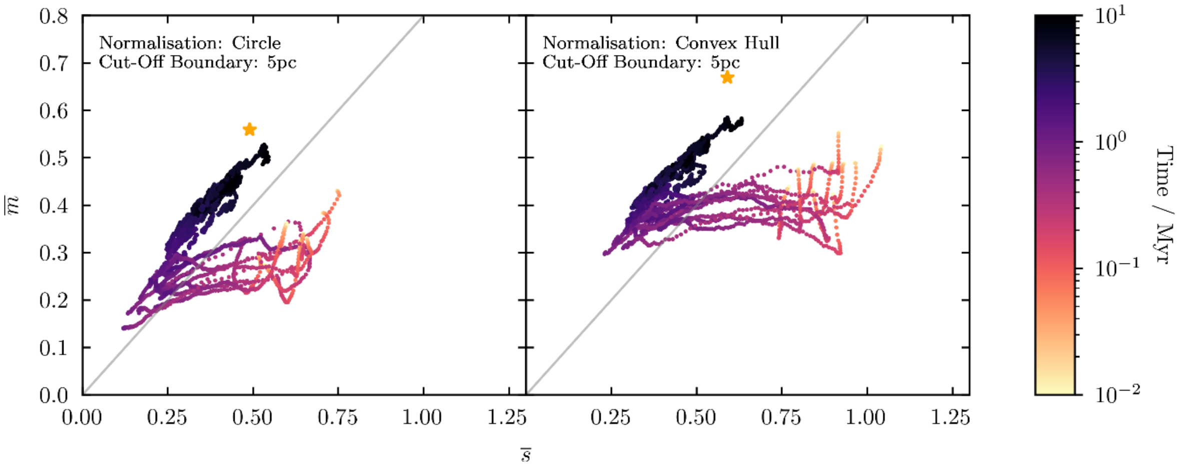

Figure 3.10 Evolution of $\overline{m}$ and $\overline{s}$ for an ONC-like region, with initial $D = 2.0$ and $\alpha = 0.3$. Ten realisations of the region are shown for both circular and convex hull normalisations. The current values of $\overline{m}$ and $\overline{s}$ for the ONC (age ~1-4 Myr) are shown as a yellow star. The evolutionary path is similar to the corresponding IC 348 and NGC 1333 simulations.

3.4.3 ONC

The evolution of our ONC-like simulations also follows the same characteristic evolution as each of their corresponding IC 348 and NGC 1333-like regions. This can be seen for the $D = 2.0$, $\alpha = 0.3$ ONC-like simulations in Figure 3.10.

Constraints placed on the ONC

None of our sets of simulations are in agreement with current observations of the ONC, as no realisations reach a high enough value of $\overline{m}$ at any point in their evolution to be consistent with observations.

This is likely in part due to the lane of dust across the centre of the ONC (shown in Figure 3 of Hillenbrand, 1997), as the Q-parameter can be affected by significant amounts of extinction (Parker & Meyer, 2012). This dust lane likely excludes a significant number of the central stars and gives a false effect of more substructure.

We have tested this by excluding a band of stars for a smooth and centrally concentrated ONC-like region, as shown in Figure 3.11. This tends to increase $\overline{m}$ and $\overline{s}$ by ~0.04 and ~0.08 respectively, moving the simulations closer to the observed values for the ONC.

Finally, we note that the ONC is one component in a much larger star-forming region, and it is often unclear where the edge of this cluster lies in relation to other stars in the Orion region. Determining the Q-parameter in star-forming regions with overlapping populations is very challenging, and is worth bearing in mind when interpreting our results. It is also possible that the dynamical evolution of the ONC has been influenced by its surrounding environment, such as the gravitational potential of the Orion cloud, something not included in these simulations.

3.4.4 Evolutionary Trends

All sub-virial regions simulated here evolved from their initial conditions towards the area of the $\overline{m}$-$\overline{s}$ plot that corresponds to a smooth centrally concentrated region. This transition takes ~1 Myr, which is in agreement with observations of the timescales within which dynamical interactions tend to erase substructure in young star-forming regions (Jaehnig, et al., 2015).

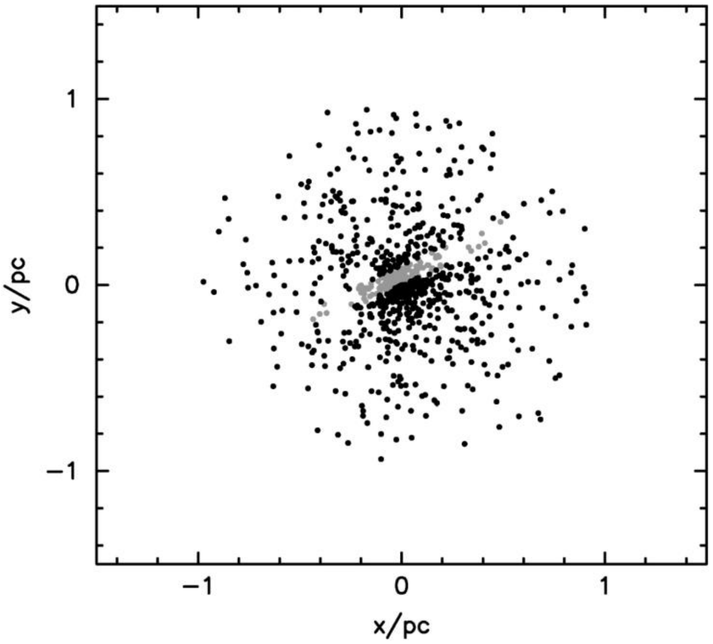

Figure 3.11 The spatial distribution of a smooth centrally concentrated ONC-like region. The band of excluded stars are shown in light grey.

When a cut-off boundary is used in the analysis, after reaching this area of the plot at ~1 Myr, each realisation then evolves up along the $Q = 0.8$ line - becoming less centrally concentrated for the rest of the 10 Myr simulation.

Effect of Initial Substructure

For regions that begin substructured, dynamical evolution takes them across the $\overline{m}$-$\overline{s}$ plot gap as they transition from fractal geometries to smooth and centrally concentrated. However, for regions which begin smooth, with a fractal dimension of $D = 3.0$, this movement takes them downwards along the $Q = 0.8$ line, meaning that they do not cross the $\overline{m}$-$\overline{s}$ plot gap. This suggests that, since only regions that begin substructured evolve to populate the $\overline{m}$-$\overline{s}$ plot gap, star-forming regions which are currently observed to lie in the gap would have been substructured in their past - ruling out smooth initial conditions for regions such as Cha I and Taurus, see Figure 3.2.

Effect of Initial virial Ratio

Our substructured simulations evolve to cross the $\overline{m}$-$\overline{s}$ plot gap for virial ratios of 0.3 and 1.5. This implies that, as long as a star-forming region begins substructured, it will evolve into the $\overline{m}$-$\overline{s}$ plot gap regardless of whether it is initially collapsing or expanding.

However, the virial ratio does affect whether an initially substructured cluster will evolve to become smooth and cross the $Q = 0.8$ line, as our super-virial ($\alpha = 1.5$) simulations remain substructured throughout the 10 Myr of evolution. Since star-forming regions are likely initially substructured (Cartwright & Whitworth, 2004; Sánchez & Alfaro, 2009; André, et al., 2010; André, et al., 2014; Kuhn, et al., 2014; Jaehnig, et al., 2015; Arzoumanian, et al., 2019), this would suggest that super-virial initial conditions can be ruled out for any star-forming region that is observed to be smooth.

3.4.5 Problems with the Q-parameter method

Our results show that, although idealised geometries do not populate all of the same areas of the $\overline{m}$-$\overline{s}$ plot as observed regions, this should not be seen as a problem with either using these as initial conditions or the $\overline{m}$-$\overline{s}$ plot as a method of analysis, because simulated regions move into the $\overline{m}$-$\overline{s}$ plot gap as they dynamically evolve.

However, there are drawbacks to be considered when using the Q-parameter method to analyse dynamical evolution. Some of these affect the interpretation of the results presented here, especially when using an evolutionary track of an $\overline{m}$-$\overline{s}$ plot to infer the likely past or future evolution of an observed region.

Figure 3.8 shows that the path which initially super-virial ($\alpha = 1.5$) regions take across the $\overline{m}$-$\overline{s}$ plot is significantly less predictable than for initially sub-virial ($\alpha = 0.3$) regions. This means that this method may be less able to reliably predict likely future or past evolution of observed regions that were initially super-virial. However, as discussed, it is still able to rule out some initial conditions.

Incomplete or inaccurate observational data can also have a significant effect on the ability to compare simulations analysed using this method to observations. For example, the ages of observed star-forming regions are likely only accurate to a factor of ~2 for those under 10 Myr (Soderblom, et al., 2014). Taking Figure 3.9 as an example, this, combined with the inherent lack of error bars in the Q-parameter method, makes it hard to fully assess whether our simulations are consistent with the observed values of $\overline{m}$ and $\overline{s}$ for NGC 1333.

Values of $\overline{m}$ and $\overline{s}$, and the Q-parameter overall, can also be sensitive to which stars are included or excluded from the analysis. This includes foreground/background stars, extinction and crowding (Parker & Meyer, 2012), as well as the chosen cluster radius. This is shown here in Figure 3.3 where, at later times, the evolutionary tracks are significantly changed once a cut-off boundary is used.

3.5 Conclusion

We have used N-body simulations of young star-forming regions to investigate their dynamical evolution in $\overline{m}$, $\overline{s}$, and the Q-parameter.

Our main results are summarised as follows:

(i) All of our initially substructured star-forming regions move into the $\overline{m}$-$\overline{s}$ plot gap. This happens as they dynamically evolve towards more smooth and centrally concentrated distributions over the first ~1 Myr.

(ii) This suggests that any star-forming region which is observed to lie in the $\overline{m}$-$\overline{s}$ plot gap must have been initially substructured, regardless of whether it was initially super or sub-virial.

(iii) Our initially super-virial substructured simulations do not cross the $Q = 0.8$ line, and therefore never become smooth and centrally concentrated. Since star-forming regions are observed to be initially substructured, this would suggest that a region which is observed to lie above the $Q = 0.8$ line must have been initially sub-virial.

(iv) All of our sub-virial IC 348-like simulations are consistent with IC 348's observed values of $\overline{m}$ and $\overline{s}$, although occasionally at slightly older ages than IC 348 is estimated to be. Our set of simulations suggest that super-virial initial conditions can be ruled out for IC 348. And, since star-forming-regions are likely initially substructured, this would therefore imply that IC 348 was substructured and sub-virial in its past.

(v) Our NGC 1333-like simulations would also suggest substructured and sub-virial initial conditions. However, the evolutionary tracks of each realisation that matches NGC 1333 tend to do so at an age of several Myr, compared to NGC 1333's estimated age of ~1 Myr.

(vi) None of our simulations were consistent with observations of the ONC, as none of them populate the same area of the $\overline{m}$-$\overline{s}$ plot. This is likely, at least in part, due to the ridge of extinction across the middle of the ONC which has the effect of causing regions to appear more substructured.

As with any analysis technique, there are drawbacks with using the Q-parameter and its associated methods. However, our simulations show that box-fractal regions will dynamically evolve into the $\overline{m}$-$\overline{s}$ plot gap - populating the area where some observed star-forming regions lie (e.g. Cha I and Taurus, as shown in). Star-forming regions can therefore be consistent with having evolved from these fractal geometries in terms of their values of $\overline{m}$ and $\overline{s}$.

Our results show that observed values of Q, $\overline{m}$, and $\overline{s}$ should not be directly compared to idealised geometries, as these synthetic box-fractals and smooth, centrally concentrated profiles have not undergone any dynamical evolution, nor are they subjected to the observational biases of real star-forming regions. Instead, Q, $\overline{m}$, and $\overline{s}$ should only be used to determine the degree to which a star-forming region is either spatially substructured or smooth and centrally concentrated.

Chapter 4

Theft and Capture in Star-Forming Regions

The work in this chapter has been accepted for publication in the Monthly Notices of the Royal Astronomical Society as Daffern-Powell, Parker, and Quanz (2022).

4.1 Summary

Gravitational interactions in star-forming regions are capable of disrupting and destroying planetary systems, as well as creating new ones. In particular, a planet can be stolen, where it is directly exchanged between passing stars during an interaction; or captured, where a planet is first ejected from its birth system and is free-floating for a period of time, before being captured by a passing star. It is unclear how the orbits of stolen planets may be different from those of captured planets, as they have both formed dynamically but through different mechanisms.

We perform sets of direct N-body simulations of young, substructured star-forming regions, and follow their evolution for 10 Myr in order to determine how many planets are stolen and captured, and investigate their respective orbital properties.

We show that in high density star-forming regions, stolen and captured planets have distinct properties, which may mean that observed exoplanets could be categorised accordingly. For planets that have formed in dense star-forming regions, the semimajor axis distribution can separate captured planets from those that are stolen and preserved, and eccentricity can then separate stolen planets from those that are preserved. In low-density star-forming regions these differences are not as distinct. However, regardless of the region's initial density, a planet that is orbiting out of the plane of any other planets in its system is likely to have been stolen or captured. And a planet that is observed with a semimajor axis greater than ~500 AU is mostly likely to have been captured onto its orbit

4.2 Introduction

As discussed in Chapter 1, the dynamical interactions that planets are more likely to experience in star-forming regions can be grouped by mechanism. These mechanisms include the disruption of a planet's orbit, where one or more of its semimajor axis, eccentricity, or inclination is altered (Hurley & Shara, 2002; Spurzem, et al., 2009; Parker & Quanz, 2012); the ejection of a planet from its system to become free-floating, where it is no longer gravitationally bound to a star (Fujii & Hori, 2019; van Elteren, et al., 2019; Cai, et al., 2019); the capture of a free-floating planet by either a new star or its original star (Perets & Kouwenhoven, 2012; Wang, et al., 2015; Parker, et al., 2017); and the theft of a planet, where it is directly exchanged between stars as they pass each other, without being free-floating for a significant period of time (Li & Adams, 2016; Mustill, et al., 2016; Wang, et al., 2020).

The result of planet theft and the capture of a free-floating planet is often the same – a planet orbiting a new star. However, the two mechanisms are themselves distinct and the evolution of the planets that undergo them may also differ significantly. For example, a free-floating planet may experience encounters that change its velocity before its subsequent capture (Wang, et al., 2015), something which cannot have happened to a stolen planet. It is therefore unclear whether stolen and captured planets should be expected to share similar orbital properties, or whether they would be distinguishable observationally.

In this Chapter we perform direct *N*-body simulations of dense, substructured star-forming regions, where half of the stars have Jupiter-mass planets placed at 30 or 50 AU. We adopt these orbital distances to facilitate a comparison with our previous work (such as Parker & Quanz, 2012) and because a significant number of exoplanets are observed at these separations. The evolution of all of the planets in each simulation are followed for 10 Myr. We test whether the orbital properties and number of captured and stolen planets differ significantly from that of each other, as well as that of planets that are still orbiting their parent star. We then compare these results to directly imaged exoplanets and the hypothetical Planet 9. We investigate this in the context of the effect of external dynamical interactions, and do not include secular interaction within multi-planet systems.

4.3 Methods

4.3.1 Simulation Set-Up

Direct *N*-body simulations were run using the Kira *N*-body integrator, as described in Chapter 2 (Portegies Zwart, et al., 1999; Portegies Zwart, et al., 2001). These were evolved for 10 Myr, with snapshots of data taken every 0.01 Myr for analysis. We use several sets of initial conditions, all of which contain 1000 stars, N_*, and 500 planets, N_p, which are randomly assigned to the stars. The planets are all Jupiter-mass. The planet mass would not be expected to significantly affect our results, especially with respect to the ejection of a planet from its system, as the interaction cross-section is primarily dependant on the stellar mass (Fregeau, et al., 2004; Fregeau, et al., 2006; Parker & Reggiani, 2013).

For our main collection of simulations, the stars are placed within a 1 pc region and distributed according to the box-fractal method described in Section 2.2. We adopt a fractal dimension $D = 1.6$ which corresponds to the maximum amount of substructure possible. Combined with an initial radius of 1 pc this fractal dimension leads to an initial median density of order $10^4\ \mathrm{M_\odot\,pc^{-3}}$. We also run an additional set of simulations with an initial radius of 5 pc, which corresponds to an initial median density of order $100\ \mathrm{M_\odot\,pc^{-3}}$.

Our combinations of initial conditions are summarised in Table 4.1, which shows the initial planetary semimajor axes, a_p, and virial ratio, α. In this way we investigate the effects of different global motions of the star-forming region with the virial ratio, and different planetary orbits with the semimajor axis.

We use two initial virial ratios of $\alpha = 0.3$ and $\alpha = 1.5$. These two virial ratios are combined with three types of initial planetary orbits: orbiting a star with a semimajor axis of $a_\mathrm{p} = 30$ AU, orbiting a star with $a_\mathrm{p} = 50$ AU, or free-floating. In the context of the Solar System these two semi-major axes correspond to the semimajor axis of Neptune and the outer edge of the Kuiper belt. The star-forming regions that contain free-floating planets are only simulated with a virial ratio of $\alpha = 0.3$ (for simulations with free-floating planets and super-virial initial conditions see Perets & Kouwenhoven, 2012; Parker et al., 2017).

Table 4.1 Summary of the initial conditions. Column 1 indicates whether the planets are initially bound to a host star or free-floating. Column 2 gives the initial radius of the star-forming region. Columns 3 and 4 give the initial virial ratio, α, of the star-forming region, and semimajor axis, ap, of each planetary system.

Planetary Orbit Type	r / pc	α	$a_{\rm p}$ / AU
Bound	1	0.3	30
	1	0.3	50
	1	1.5	30
	1	1.5	50
	5	0.3	30
Free-Floating	1	0.3	-

All planets that are bound to a star initially have zero eccentricity, $e = 0$, and are orientated randomly with respect to the coordinate system of the simulation i.e., they have random inclinations and random argument of latitude.

Twenty realisations of each set of simulation were run and analysed. Each of these simulations are statistically identical, with the same virial ratio and initial semimajor axis, but with different random number seeds used to initialise the positions, velocities, and masses of the stars.

4.3.2 Analysis

The output of the N-body simulation was analysed for every snapshot, in order to follow the evolution of each planet's orbit, and identify which have been stolen and captured by other stars.

Identification of Bound Systems

Planetary systems are found in the output data by identifying planets and stars that are mutual nearest neighbours and have a negative binding energy i.e., are gravitationally bound, using Equation 4.1. Binary systems which contain a planet, and are therefore planetary systems, are distinguished from star-star binaries using the mass of each body.

$$E = m_i m_j \left[\frac{{\boldsymbol{v}_{ij}}^2}{2(m_i + m_j)} - \frac{G}{\boldsymbol{r}_{ij}} \right] \tag{4.1}$$

Triple systems that include a planet are found in a similar way. In this case, all three bodies must be each other's first and second nearest neighbours, the two closest bodies must be gravitationally bound, and the centre of mass of the two closest bodies must be bound to the third body. If a planet is found to be in a triple system, it is logged as such, treated as a binary with its closest companion for the rest of the analysis, then followed up manually if the system is of particular interest.

Planet-planet binaries are found in the same way as star-planet binaries, logged, and followed up manually.

Orbital Parameters

The semimajor axis and eccentricity are calculated for all planetary systems. The absolute inclination, relative to the coordinate system, is calculated for stolen and captured planets. For preserved planets, the change from its original inclination is used.

To calculate the orbital parameters, first, the angular momentum of the system, $\boldsymbol{L}_{\mathrm{tot}}$, and its z component, L_z, are calculated using Equations 4.2 and 4.3:

$$\boldsymbol{L}_{tot} = \frac{m_i m_j}{m_i + m_j}(\boldsymbol{r}_{ij} \times \boldsymbol{v}_{ij}) \tag{4.2}$$

$$L_z = \frac{m_i m_j}{m_i + m_j}(r_{ij,x} \cdot v_{ij,y} - r_{ij,y} \cdot v_{ij,x}) \tag{4.3}$$

where $r_{ij,x}$ is the x component of $r_i - r_j$, and similar for $v_{ij,y}$, $v_{ij,x}$, and $r_{ij,y}$.

Then, the semimajor axis, a, eccentricity, e, and inclination, i, for each planet can be calculated using Equations 4.44.5, and 4.6:

$$a = \frac{G m_1 m_2}{2|E|} \tag{4.4}$$

$$e = \sqrt{1 + \frac{2\ m_1 + m_2}{m_1^3 m_2^3} \frac{\boldsymbol{L}_{\mathrm{tot}}^2 |E|}{G^2}} \tag{4.5}$$

$$i = \cos^{-1}\left(\frac{L_z}{\boldsymbol{L}_{\mathrm{tot}}}\right) \tag{4.6}$$

Classification of Orbital Type

In any given snapshot a planet is classified as either preserved, captured, stolen, or free-floating.

A planet is classified as free-floating if it is not found to be bound to another star or planet in that snapshot. A planet that is bound to a star is classified as preserved, captured, or stolen based on its binary history. A planet is preserved if it is still, and was always, bound to its original star in every prior snapshot. A planet is captured if it was free-floating in the previous snapshot, but is now bound to a star, whether that be its original star or a different one. Finally, a planet is classified as stolen if it is bound to a star in the current snapshot, but was bound to a different star in the previous snapshot. In this way, captured and stolen planets are distinguished based on whether they have been free-floating for a significant period of time. Since we use 0.01 Myr snapshot intervals, the maximum amount of time that one of our stolen planets could have been unbound is <0.01 Myr. We believe that this is a reasonable assumption given that this is much shorter than the ~0.1 Myr crossing time of our star-forming regions, and therefore the characteristic timescale over which stellar interactions tend to occur.

The number of each type of planetary orbit is calculated in each snapshot.

4.4 Results & Discussion

First, we present results for planets in high density ($r = 1$ pc, 10^4 $\mathrm{M}_\odot\,\mathrm{pc}^{-3}$) simulations in Sections 4.4.1 to 4.4.4, before discussing planets in low density ($r = 5$ pc, 100 $\mathrm{M}_\odot\,\mathrm{pc}^{-3}$) simulations in Section 4.4.5.

4.4.1 Number of Stolen and Captured Planets

Over time

Most theft and capture happens at early times, when the region is most dense and the stars and planets are more likely to experience encounters. These mechanisms are therefore most relevant to planets that have formed rapidly. As discussed in Section 1.3.2, planet formation through disk instability would occur earlier and more rapidly than core accretion. Since it is expected that disk instability would tend to create giant planets, our results suggest that theft and capture are most relevant to giant planets that have formed rapidly through disk instability.

For most new planetary systems, the planet is stolen or captured onto an orbit that is either inherently unstable, or is easily destroyed by subsequent interactions. In particular, the same high densities that tend to create more stolen and captured systems at early times also increase the likelihood that they will be destroyed. This leads to an initial peak in the number of stolen and captured planets, which is visible Figure 4.1, as the number of stolen and captured planets increase sharply before decreasing and levelling off at around ≈1 Myr. This is the case for every simulation.

After this levelling off at ≈1 Myr, an average of ≈4% of planets are either captured or stolen for the remainder of the simulations. This change over time can be seen in the first four columns of Figure 4.1.

Effect of Initial Conditions

The average number of stolen and captured planets at 10 Myr, for simulations where the planets are initially bound, is shown in the boxplots of Figure 4.2. As might be expected, there are on average more captured planets at 10 Myr when the planets are initially placed on the wider 50

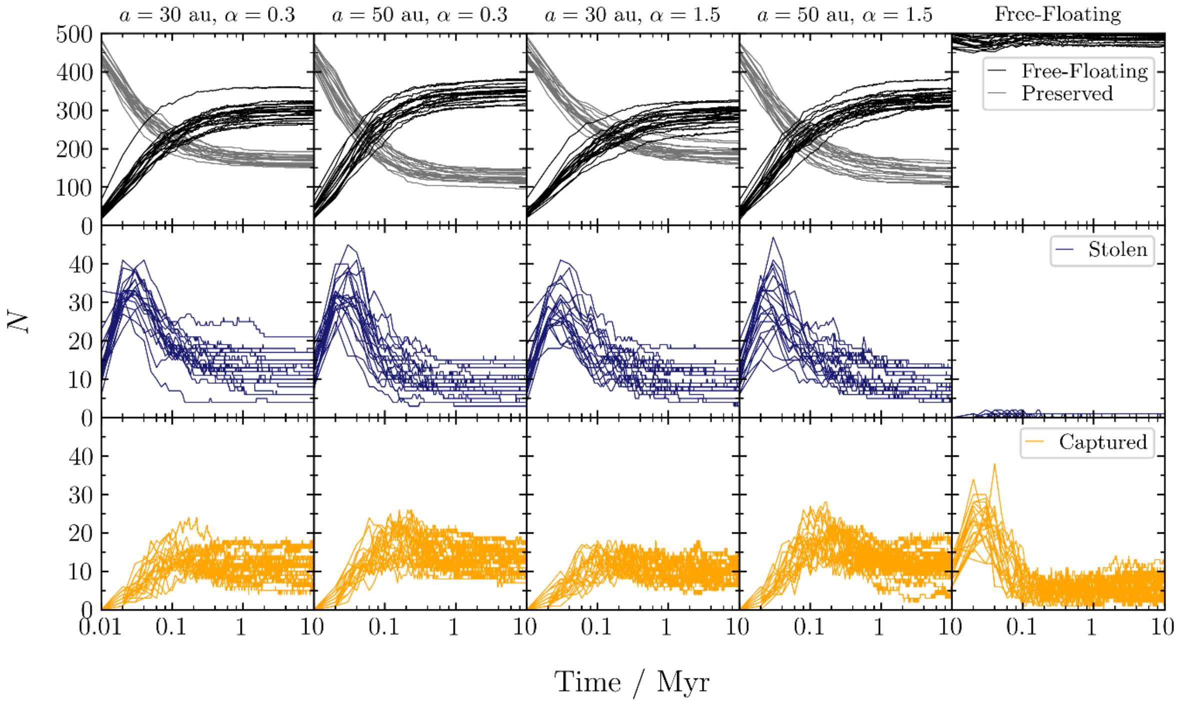

Figure 4.1 The number of each type of planetary orbit, plotted from the first snapshot at 0.01 Myr to 10 Myr for the higher initial density, $r = 1$ pc simulations. Each of the first four columns shows results for one of the four bound-planet initial conditions, with lines plotted separately for each of the 20 realisations. The final column shows the same for initial conditions where all planets are initially free-floating with $\alpha = 0.3$. The number of free-floating, preserved, stolen, and captured planets are shown as black, grey, blue, and orange lines respectively.

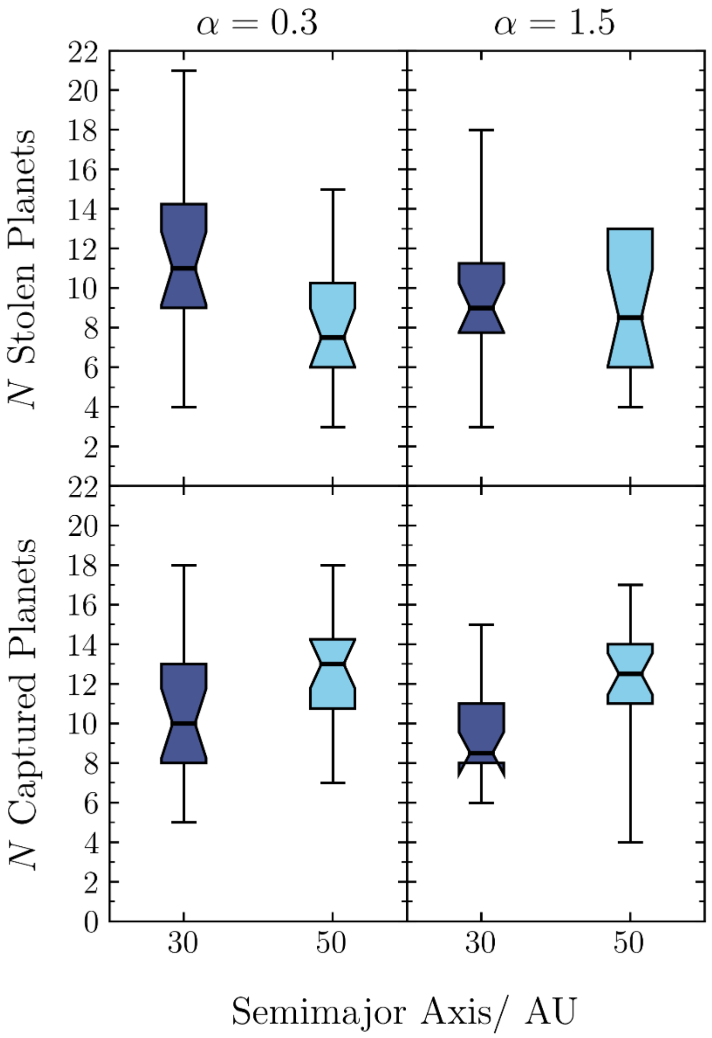

Figure 4.2 The number of stolen and captured planets at 10 Myr, for each of the 4 initial conditions where the planets are initially bound to stars in $r = 1$ pc star-forming regions. These results are shown as a separate notched boxplot for each of the initial conditions. Each median value is shown as a thick black horizontal line, and the notches are the sloped outer edges which angle outwards from each median line. These notches show the 95% confidence limits for their corresponding median, where any part of the box plot that does not have a sloped outer edge is not within the 95% confidence interval. The second rightmost captured planet box plot has a 95% confidence limit that is lower than the lower interquartile range. This means that the lower notches on this boxplot extend further than the box itself, thereby producing the inverted shape. The whiskers show the full range of values. There is no upper whisker for the rightmost stolen planet boxplot because the highest value is equal to the upper quartile. This is possible for sets of discrete data, and happens here because several of the simulations finish with 13 stolen planets, which is the highest value in that dataset.

AU orbits. This is regardless of the initial virial ratio, and is because planets that are initially on wider orbits have a lower binding energy and are more easily ejected from their system during encounters, therefore increasing the number of free-floating planets that are available to be captured.

Figure 4.2 also compares the final numbers of stolen planets across the four sets of bound-planet initial conditions. Unlike with captured planets, the average number of stolen planets is higher when they are initially placed at 30 AU, rather than 50 AU, for a given initial virial ratio. In fact, for the 30 AU initial conditions there are also on average more stolen planets than captured ones. In this way, for larger initial separations, planets are more likely to become unbound rather than being stolen and transferred to the other star. This is consistent with Clarke & Pringle (1993, their Figure 3), who find that this is also the outcome for protoplanetary disk material at different radii during stellar encounters.

The notches on each box plot in Figure 4.2, which are the sloped outer edges that angle outwards from each median line, represent the 95% confidence limits of their corresponding median value. It can be seen from the second panel that the 95% confidence limits for the median number of stolen planets fully overlaps for the 30 AU and 50 AU initial semimajor axes. It should therefore not be concluded that a change in initial semimajor axis affects the final number of stolen planets for the super-virial $\alpha = 1.5$ initial conditions. However, it can be concluded that, for the sub-virial $\alpha = 0.3$ initial conditions, increasing the initial semimajor axis to 50 AU decreases the final number of stolen planets. This is the opposite trend than is seen for captured planets.

This difference in the final number of stolen planets for the sub-virial ($\alpha = 0.3$) initial conditions is likely caused by the increased number of free-floating planets for the 50 AU initial conditions. Although the number of stolen planets is consistent at early times for both the $a_{\rm p} = 50$ AU and $a_{\rm p} = 30$ AU initial conditions, the medians begin to differ with 95% confidence after 0.12 Myr - the same time at which the number of stolen planets begins to decrease in all simulations. It is at this time that the higher number of free-floating planets means that there are fewer bound planets available to be stolen, and also more free-floating planets which are capable of disrupting a stolen planet's orbit.

This is a clear example of captured and stolen planets being affected in not only different, but in this case opposite ways, by certain initial conditions - underscoring that captured and stolen planets are distinct phenomena that are formed through independent mechanisms.

These results also highlight the significant effect that a planet's initial semimajor axis can have on its fate, in agreement with previous studies (Parker & Quanz, 2012; Hao, et al., 2013; Zheng, et al., 2015; Cai, et al., 2019).

Free-Floating Initial Conditions

The initial peak in the number of captured planets is larger for the initial conditions where the planets are initially free-floating, rather than bound to a star, as shown in the bottom right panel of Figure 4.1. This is simply because there are more free-floating planets available to be captured at early times with these initial conditions.

Conversely, however, there are significantly fewer stolen planets in these simulations. The highest number of stolen planets for the free-floating, $\alpha = 0.3$ initial conditions is 2. Several of the 20 simulations reach 2 stolen planets within the first several snapshots, but then subsequently drop to 1 or 0. This is because, in order to be stolen, the planet must first be captured onto an orbit. In this way, the earliest time at which a planet can be stolen is later for simulations with free-floating initial conditions, thereby reducing the initial peak to only < 2 stars. This is an effect that the number of stolen planets does not recover from, as it is at these earlier times when planetary interactions, including theft, are more likely.

This has implications for studies that use free-floating initial conditions to investigate planet capture and theft. For example, Parker et al. (2017) used N-body simulations with free-floating initial conditions to investigate the origin of Planet 9 in the context of it having formed around a star other than the Sun. The choice of free-floating initial conditions will have reduced the frequency of planet theft, thereby also reducing the total number of planets which are orbiting a new star at the end of the simulations. It may therefore have affected how their conclusion, that the likelihood of Planet 9 having originated from another planetary system is almost zero, compares to that of other similar studies such as Mustill et al. (2016) and Li & Adams (2016), who find the chance of Planet 9 having formed via theft to be non-zero. Although, as I will discuss, and is shown in Figure 4.3 and Figure 4.4, we find that planets with semimajor axes in Planet 9's predicted orbital range are most likely to have been captured.

Nevertheless, it is important to be aware that free-floating initial conditions suppress the formation of stolen planetary systems, compared to corresponding simulations in which the planets are initially bound.

We do not discuss free-floating initial conditions further, due to the low number of stolen planets that these initial conditions produce. All further discussion relates to the sets of simulations where the planets are initially bound to host stars.

A Note on Planet-Planet Systems

We identify 5 planet-planet systems across all of our simulations. These planets tend to have very rich dynamical histories. For example, one planet in the $\alpha = 0.3$, $a_\mathrm{p} = 30$ AU simulations has repeated interactions with another star and planet. This leads to it being in a temporary planet-planet system. It is removed and then recaptured by its original star throughout the simulation, and ends the 10 Myr as free-floating, after becoming unbound from its original star a final time.

All of these planet-planet systems are short-lived, and are each only identified in one 0.01 Myr snapshot. Such systems would therefore be very unlikely to be observed, and we do not include them in any formal analysis.

4.4.2 Semimajor Axis

The semimajor axis distributions for preserved, captured, and stolen planets differ significantly, as shown in Figure 4.3 and Figure 4.4. Of the planetary systems that are bound at 10 Myr, Figure 4.3 shows that ~20% of preserved planets have their semimajor axes disrupted such that it is greater than the initial 30-50 AU value. In contrast, between $\sim 60 - 80\%$ of captured and stolen planets have semimajor axes greater than this.

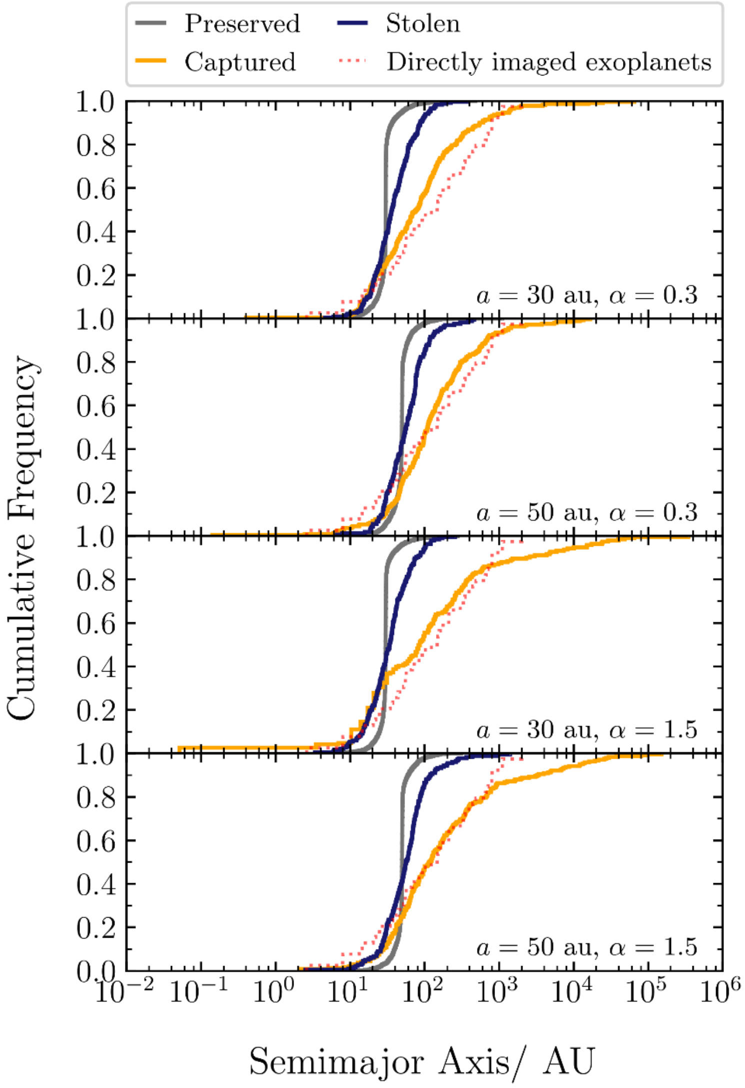

Figure 4.3 The semimajor axis distribution for planets that are bound to a star after 10 Myr, divided into the three types of planetary orbit: preserved, captured, and stolen. Results are summed and shown for all 20 realisations of all 4 sets of bound-planet, $r = 1$ pc initial conditions, which are shown in separate panels. The semimajor axis distribution for directly detected exoplanets is also shown for comparison as a dotted red line in each panel. For the observed exoplanets, the semimajor axis is used where the data is available, otherwise the projected separation is plotted.

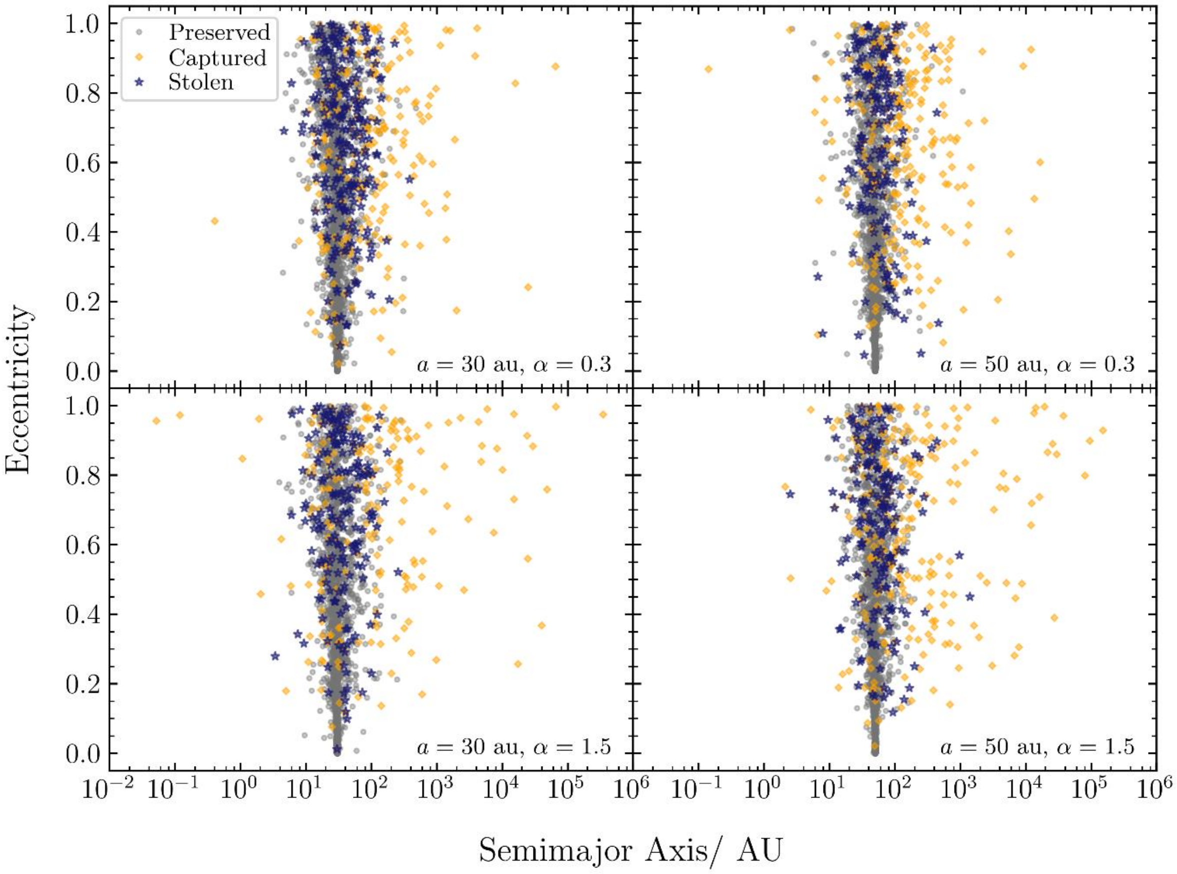

Figure 4.4 Characteristic ‘firework’ plots of the semimajor axis vs eccentricity distribution. Results are shown for planets that are bound to a star after 10 Myr, divided into the three types of planetary orbit: preserved, captured, and stolen. Each planet is shown as a semi-transparent point. Results are summed and shown for all 20 realisations of all 4 sets of bound-planet, $r = 1$ pc initial conditions, which are shown in separate panels.

One of the most noticeable trends in Figure 4.3 and Figure 4.4 is that captured planets tend to be on wider orbits than stolen and preserved planets. This is the case for all initial conditions and for both the average and upper limit values of a. This is a difference that could be seen observationally and used to identify a population of captured planets, as these results suggest that an exoplanet with an observed semimajor axis of $\gtrsim$500 AU has been captured. Comparing this to Planets 9's predicted orbital range of $a \sim 400 - 800$ AU, eccentricity ($e \sim 0.2 - 0.5$), and inclination ($i \sim 15 - 25°$) (Batygin, et al., 2019; Fienga, et al., 2020), these results suggest that, should Planet 9 exist, it is most likely to have been captured.

Captured planets can have these wider orbits because capture tends to happen when the planet and star exit the cluster at the same time and in the same direction (Perets & Kouwenhoven, 2012; Parker & Meyer, 2014). In these cases, the star and planet will tend to be relatively isolated, in areas of relatively lower local density, meaning that gravitational interactions that may interfere with the new orbit are less likely. More loosely bound orbits will therefore tend to remain bound for longer, meaning that there will be more capture overall in these conditions. Importantly, within our substructured simulations, these conditions can be met when a star and planet exit a 'clump' of substructure, as well as when then region as a whole dissolves.

Our own investigation, summarised in Figure 4.5, confirms that planets are often being captured through the mechanism described by Perets & Kouwenhoven (2012) within our simulations. In order to investigate this, Figure 4.5 shows the local number density around stars that capture or steal a planet in the snapshot that the capture or theft occurs.

Figure 4.5 shows that, while planet theft tends to happen within the denser areas of substructure, as expected, planet capture tends to happen in areas of lower local density, compared with both theft and the region as a whole. This is shown in Figure 4.6, which shows the average number density for all stars in our subvirial simulations over time. The characteristic time of capture is ~0.1 Myr (see Figure 4.1). Comparing Figure 4.5 to Figure 4.6 then shows that the average local number density for all stars, when planets are most likely to be captured, is ~10^5, while the local density around stars that capture planets is ~10^2. This result also holds for the supervirial

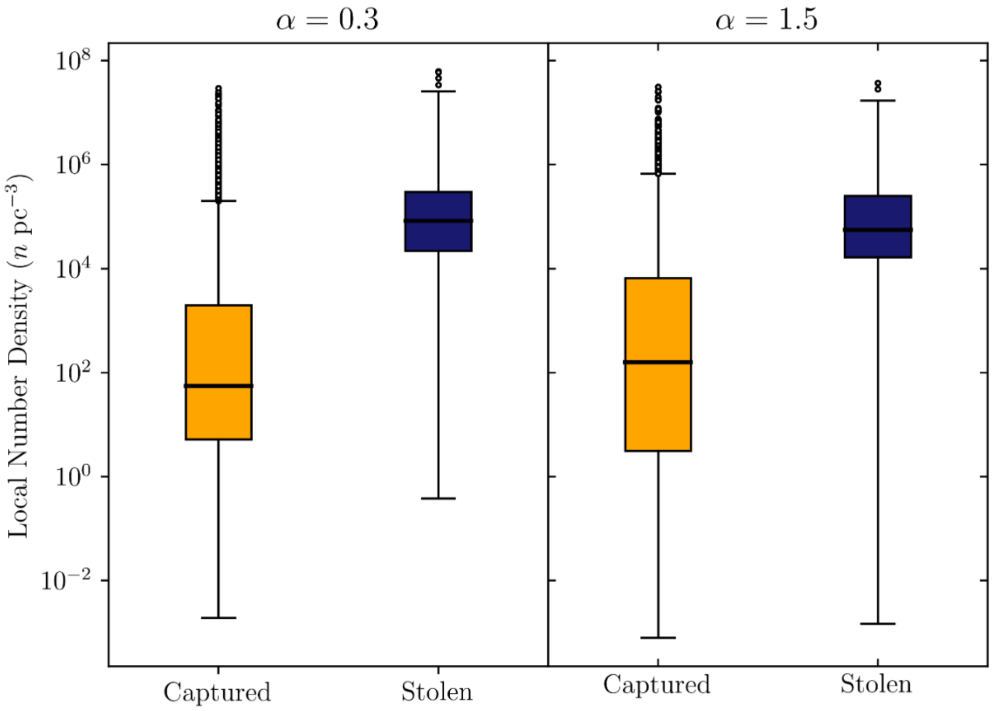

Figure 4.5 The local number density around stars that capture and steal a planet, at the time that the capture or theft occurs. This is shown for both supervirial and subvirial initial conditions, where planets are initially placed at 30 AU. Each median value is shown as a thick black line, and the boxes show the interquartile range of the results. The whiskers extend to 1.5 times the interquartile range, and the points are ‘outliers’ with values beyond 1.5 times the interquartile range.

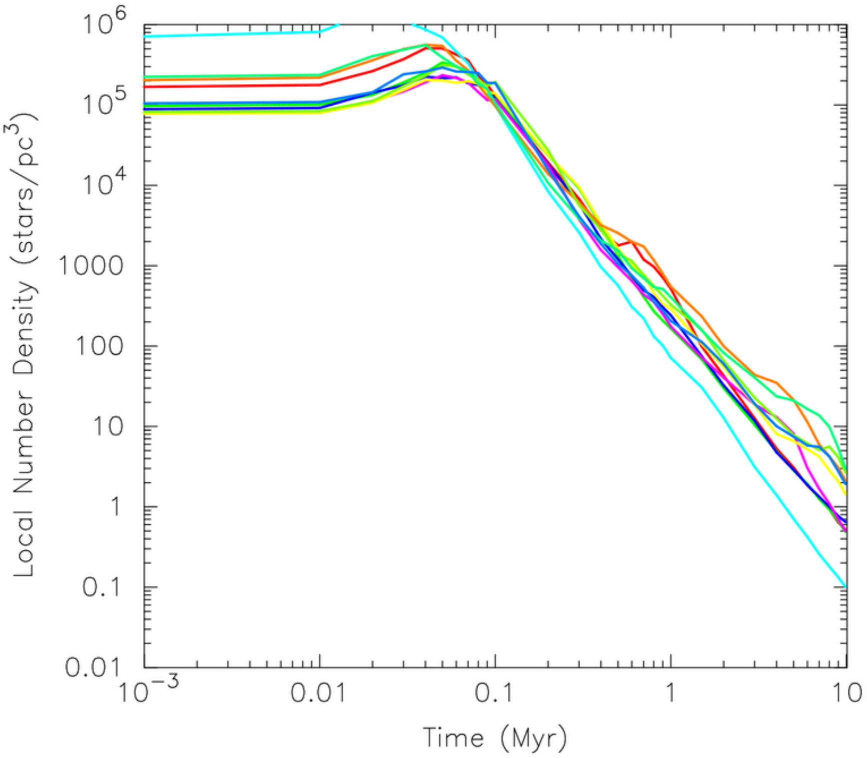

Figure 4.6 The average local number density for all stars in each of our subvirial simulations over time.

simulations, as the average local density in the supervirial simulations only differs significantly from the subvirial regions at later times.

In our simulations this capture mechanism can occur at relatively early times, because as the areas of substructure begin to mix and dynamically evolve immediately, as shown in Figure 3.4. In this way, the cluster as a whole does not need to have begun dissolving for the mechanism described by Perets & Kouwenhoven (2012) to take place.

We demonstrate that the local number density is the most reasonable measure of position within the cluster by also showing these results for distance from the star-forming regions centre of mass. Distance from the centre of mass might be expected to be the most reasonable measure for whether a star or planet is exiting the star-forming region. Indeed, this would be the case for a region with an initially smooth radial density profile. However, for substructured distributions, the centre of mass of a region is not physically meaningful, as it can be in a relatively empty area in between areas of substructure. This means that a star and planet that are exiting a clump together may have a decreasing distance from the center of mass. The mechansism described by Perets & Kouwenhoven (2012) would therefore not be accurately respresented in these cases based on the center of mass distance.

This leads to the distribution shown in Figure 4.7, in which there is no significant difference between the stolen and captured planet distributions for the subvirial simulations, and a small difference for the supervirial simulations. For the subvirial simulations, the median (and interquartile range) values for the captured planets are 1.5 (0.73 – 3.0), and 0.67 (0.51 – 0.85) for the stolen planets. Similarly, for the supervirial simulations the median and interquartile range values are 5.0 (1.3 – 12) and 0.76 (0.56 – 0.97), respectively. The much smaller spread, and lower median, of the stolen planet distribution is predominantly caused by planet theft tending to happen at earlier times, when the region as a whole is smaller.

The semimajor axis distribution of stolen planets is similar to the semimajor axis distribution of preserved planets. It is possible that using a realistic range of initial semimajor axes would add spread to the distributions, thereby causing them to be more similar, and harder to separate. However, comparing previous studies shows that results are consistent between simulations that

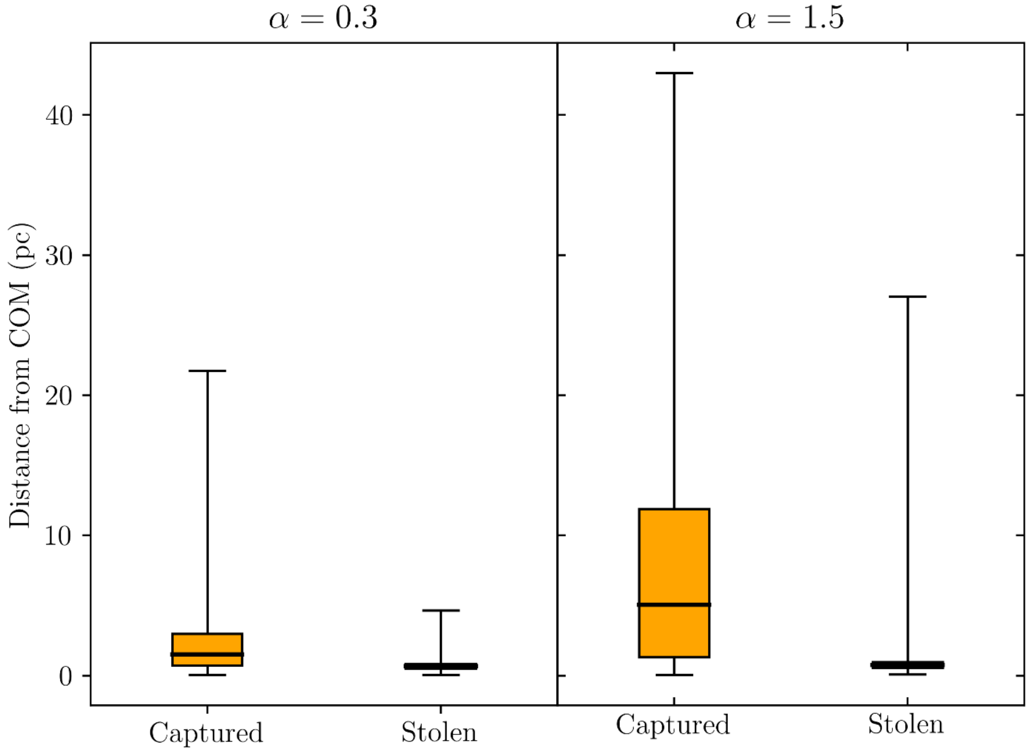

Figure 4.7 The distance from the star-forming regions centre of mass for stars that capture and steal a planet, at the time that the capture or theft occurs. This is shown for both supervirial and subvirial initial conditions, where planets are initially placed at 30 AU. Each median value is shown as a thick black line, and the boxes show the interquartile range of the results.

use single semimajor axis values, and those that either select the semimajor axes from a distribution or use a wide range. For example, results are consistent when a single semimajor axis of 30 AU is used, and when a range of semimajor axes that have been sampled from a distribution that has a median of 30 AU (e.g. Parker & Quanz, 2012; Forgan et al., 2015; Zheng et al., 2015).

Figure 4.3 also shows the projected separation distribution for directly imaged exoplanets[7] (in most cases the projected separation data is used in place of the semimajor axis). We emphasise that the sample of directly imaged exoplanets is likely to be incomplete and affected by statistical biases, and we have no information on whether each planet in the sample formed at its observed separation, or whether some process(es) moved the planets.

It should be noted that in Figure 4.3 we are comparing the known semimajor axis of simulated systems, to the observed separation of exoplanets as projected on the sky, which are not the same thing. However, the semimajor axis of most exoplanetary systems is unknown, so it is common to use the projected separation in its place, and we feel that it is reasonable to do this while bearing in mind the limitations. For exoplanets on circular orbits, the projection on the sky is the lower limit to the semimajor axis, because the orientation of the planet's orbit on the sky will act to reduce the observed separation. For exoplanets on eccentric orbits, as we would expect those on very wide orbits to be, the semimajor axis may be larger or smaller than the observed separation depending on the planets orbital position and orientation on the sky.

Despite these caveats, Figure 4.3 shows that there is general agreement between our captured planet semimajor axis distribution and the projected separations of directly imaged exoplanets. This is the case for all of the high-density initial conditions shown in Figure 4.3 suggesting that, if directly imaged planets on wide orbits are a result of dynamics, they are likely to be captured rather than stolen or preserved. If this is the case, then we might expect to discover more such planets on extremely wide (>1000 AU) orbits, which are present in our simulation data but not

---

[7] This data was taken from the NASA Exoplanet Archive on 18/02/2021.

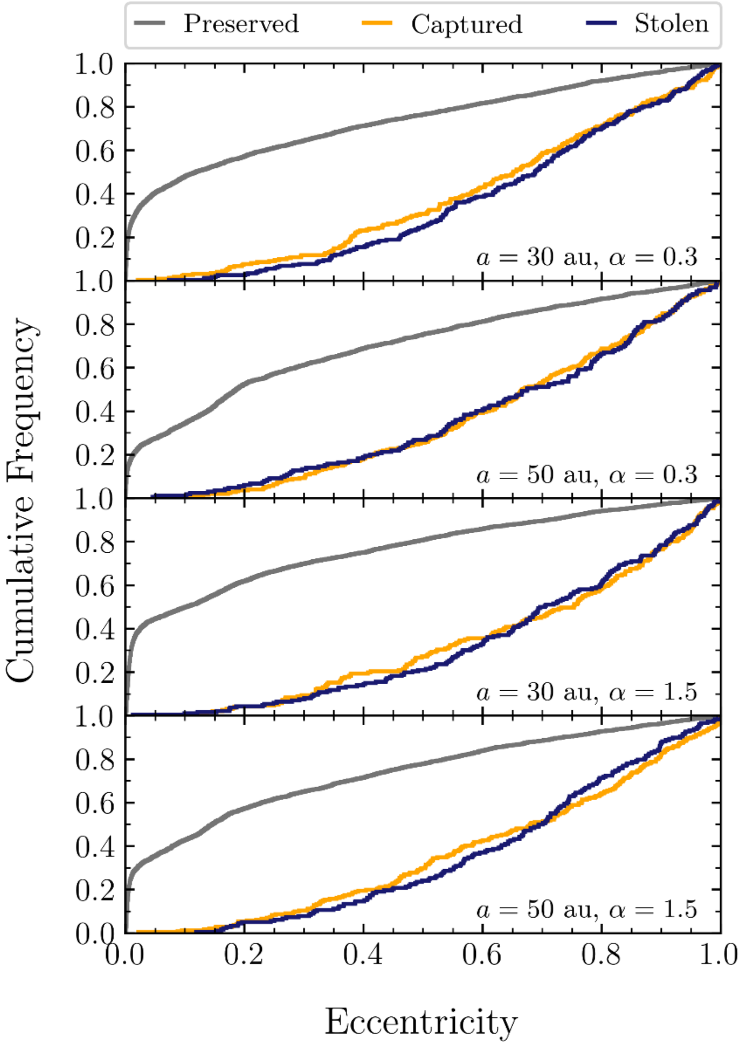

Figure 4.8 The eccentricity distribution for planets that are bound to a star after 10 Myr, divided into the three types of planetary orbit: preserved, captured, and stolen. Results are summed and shown for all 20 realisations of all 4 sets of bound-planet, $r = 1$ pc initial conditions, which are shown in separate panels

yet in the observational data (though see Durkan et al. 2016, for efforts towards this parameter space).

4.4.3 Eccentricity

Figure 4.8 shows that the eccentricity distribution for captured and stolen planets is thermal. This is expected for captured planets as a thermal distribution is seen for binary systems that have formed dynamically (Heggie, 1975).

Meanwhile the preserved planet distribution is produced by the relative readiness with which a planet's eccentricity can be disrupted, compared to its semimajor axis. Using the definition from Parker & Quanz (2012), that a planet is disrupted if its semimajor axis is changed by 10% or its eccentricity is increased above 0.1, we find that where ~20% of preserved planets have their orbits disrupted in terms of semimajor axis, ~40 – 50% are disrupted in terms of eccentricity.

Figure 4.4 shows that it is also possible for some stolen and captured planets to have semimajor axes that are indistinguishable from preserved planets that have not had their orbit disrupted.

The results of K-S tests confirm that the eccentricity distributions for captured and stolen planets are all very similar (K-S statistics < 0.1), to a relatively high confidence (p-values ranging from 0.33 to 0.80). This is the case for all sets of bound-planet, $r = 1$ pc initial conditions. The null hypothesis, that the eccentricity distributions for captured and stolen planets are sampled from the same underlying distribution, therefore cannot be rejected for these simulations.

Eccentricity can therefore not be used to distinguish captured from stolen planets in observations of exoplanets that have likely formed in dense regions. The eccentricity distribution could, however, be useful for distinguishing the planets in a population that are preserved from those that are new systems, which have formed dynamically through either capture or theft.

4.4.4 Inclination

A change in inclination would not be observable in a planetary system without other planets or an observable protoplanetary/ debris disk. However, should the plane of the planetary system be observable, inclination information could be useful in determining if the planet was likely captured or stolen.

Figure 4.9 shows that, as expected, planets are stolen and captured onto orbits with random inclinations. ~20% of preserved planets have their inclinations disrupted by more than 10%.

This is comparable to the percentage that are disrupted in terms of their semimajor axis. As would be expected, this shows that, should a planet be observed in a system with a disk or other planets, the relative inclination could be used to determine whether the exoplanet has likely been captured or stolen from another star.

4.4.5 Effects of Lower Density

For comparison, we have also run a set of simulations using lower density (100 $M_\odot\,pc^{-3}$) initial conditions, with an initial radius of 5 pc. We compare these lower density $\alpha = 0.3$, 30 AU simulations to the higher density $\alpha = 0.3$, 30 AU simulations in Figure 4.10 and Figure 4.11.

Figure 4.10 compares the number of each type of planetary orbit over time, in the same way as Figure 4.1. The first difference that can be seen is that the low-density initial conditions produce fewer free-floating planets than preserved planets after 10 Myr. This is in contrast to the high-density initial conditions which produce more free-floating planets than preserved planets, as more are ejected from their birth system.

It can be seen from the bottom panels of Figure 4.10 that the lower density initial conditions lead to more captured planets after 10 Myr. This is because, in this less extreme environment, although there are fewer free-floating planets available to be captured, captured systems that do form are more likely to survive. There is no significant change to the average number of stolen planets at 10 Myr when the density is lowered. However, there is a smaller spread in the number of stolen planets for the low-density initial conditions.

Both the semimajor axis and eccentricity distributions are affected by the initial density being lowered. This is shown in Figure 4.11, where the higher density results are shown as slightly

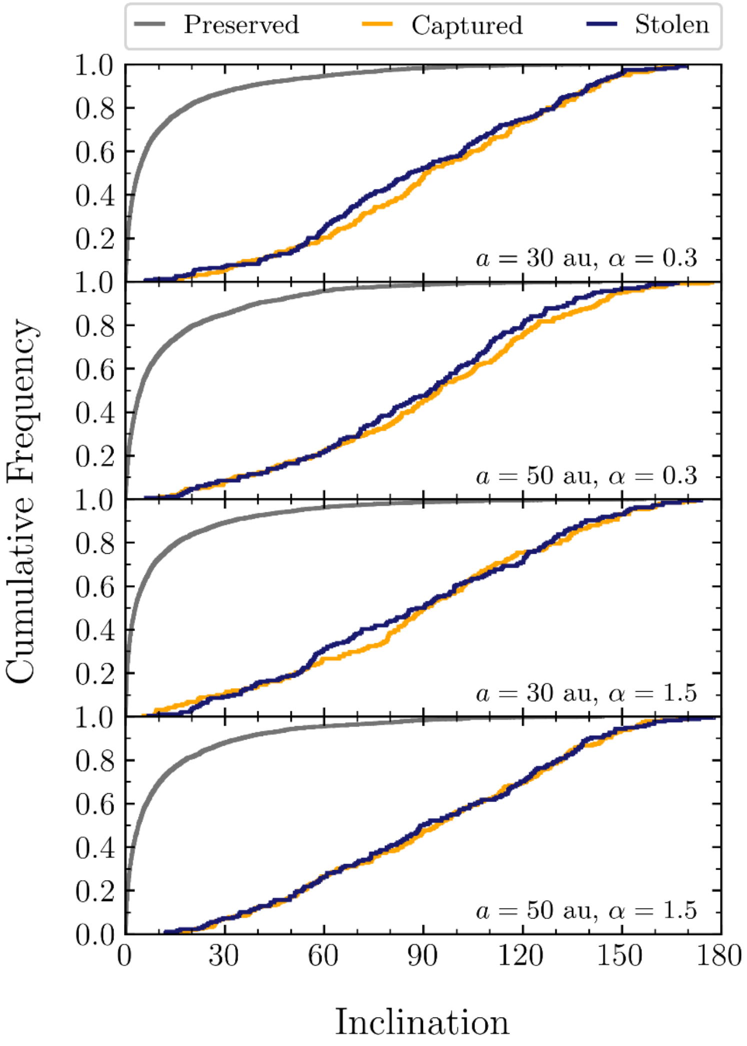

Figure 4.9 The inclination distribution for planets that are bound to a star after 10 Myr, divided into the three types of planetary orbit: preserved, captured, and stolen. Results are summed and shown for all 20 realisations of all 4 sets of bound-planet, $r = 1$ pc initial conditions, which are shown in separate panels

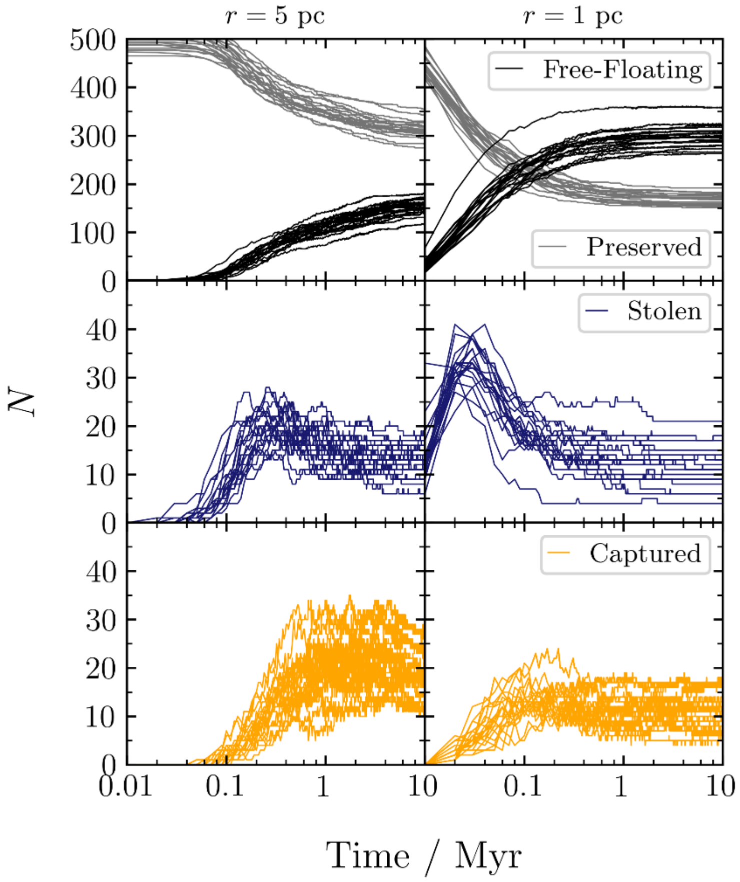

Figure 4.10 The number of each type of planetary orbit over 10 Myr, plotted from the first snapshot at 0.01 Myr to 10 Myr. The first column shows this for the lower density, $r = 5$ pc, $\alpha = 0.3$, $a_{\mathrm{p}} = 30$ AU initial conditions. The second columns shows this for the higher density $r = 1$ pc, $\alpha = 0.3$, $a_{\mathrm{p}} = 30$ AU initial conditions. The number of free-floating, preserved, stolen, and captured planets are shown as black, grey, blue, and orange lines respectively.

transparent dashed lines, and the low-density results are shown as solid lines. More stolen planets are able to stay stable on wider orbits for the lower density initial conditions, therefore broadening the stolen planet semimajor axis distribution. For captured planets, the top ~5% of the semimajor axis distribution is similar, regardless of density. However, the additional number planets that are captured in the lower density simulations tend to preferentially fill the centre of the distribution. This has the effect of making the captured planet semimajor axis distribution more similar to that of the stolen and preserved planets. Nevertheless, it is still the case that a planet on an orbit wider than ~500 AU is most likely to be captured, regardless of the initial density of the star-forming region.

The eccentricity distribution of the stolen planets remains thermal, as shown in the right panel of Figure 8. However, the eccentricity distribution of the captured planets flattens for the low-density simulations. This means that, at these low densities, the eccentricity distribution of the stolen, captured, and preserved planets are all distinct from each other. Eccentricity data could therefore be used to separate populations of stolen, captured, and preserved planets from each other in the exoplanet data, should an estimate of their formation density be available (Winter, et al., 2020; Adibekyan, et al., 2021).

4.4.6 Comparison to previous work

As has already been highlighted by other studies (e.g. that if Craig & Krumholz, 2013, when comparing their results to Parker & Quanz, 2012), differences in the initial conditions and method of simulation can result in large differences in the number of free-floating planets, as well as the numbers of stolen, captured, and preserved planets.

In terms of the number of free-floating planets, we find that $\gtrsim$50% of planets are free-floating at the end of these simulations, depending on the initial conditions. This means that they are of order 10 times more common than stolen and captured planets, and ~1.5–2 times more common than planets that remain bound to their original star. This is higher than the 10% obtained by Parker & Quanz (2012) for simulations where planets are placed at 30 AU, and is likely caused by our use of a fractal dimension of 1.6, rather than 2. This leads to initial densities that are

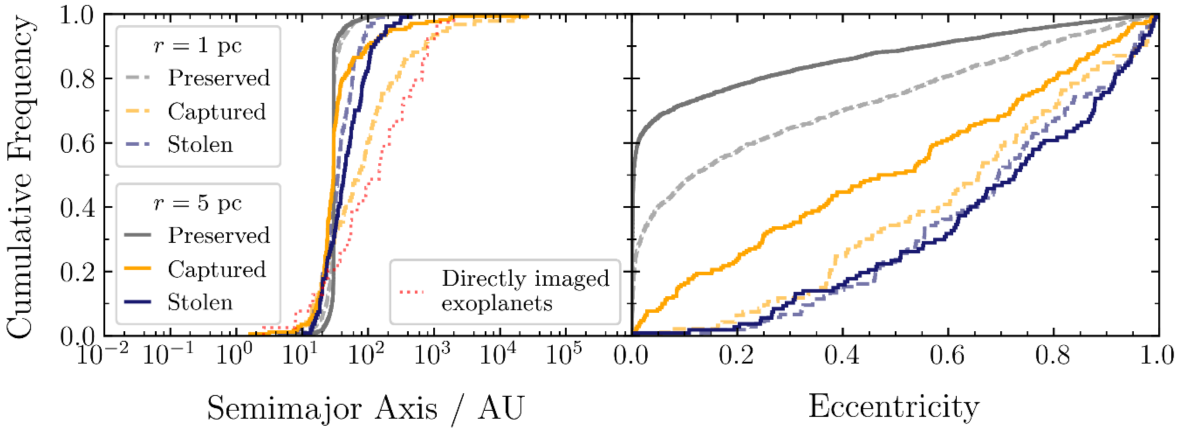

Figure 4.11 The semimajor axis and eccentricity distributions for planets that are bound to a star after 10 Myr, divided into the three types of planetary orbit: preserved, captured, and stolen. Results are summed and shown for all of the lower density $r = 5$ pc, $\alpha = 0.3$, $a_{\mathrm{p}} = 30$ AU initial conditions and the higher density $r = 1$ pc, $\alpha = 0.3$, $a_{\mathrm{p}} = 30$ AU initial conditions. The lower density results are shown as solid lines, and the higher density results are shown as slightly transparent dashed lines.

~10 times higher in our high density, $r = 1$ pc simulations (of order 10^4 M$_\odot$pc^{-3}, compared to 10^3 M$_\odot$pc^{-3}, in Parker & Quanz, 2012). Although it is unclear whether many star-forming regions have initial densities of this magnitude (Parker, 2014), the purpose of this paper is primarily to investigate the orbital properties of stolen and captured planets in the most extreme star-forming environments.

In terms of the frequencies of stolen and captured planets, our ≈4% is an order of magnitude higher than the 0.4% obtained by Parker & Quanz (2012), due to their N-body simulations having initial densities that are an order of magnitude lower than those used in this paper.

Although the frequencies of each type of planet can vary significantly in this way, the orbital ranges and distributions in a—e space are broadly consistent with previous studies.

4.5 Conclusion

We use N-body simulations of planets in star-forming regions to investigate the dynamical evolution of the planets within them. Our star-forming regions are highly substructured initially, with a fractal dimension of $D = 1.6$, and we model star-forming regions with both sub and super-virial initial conditions (virial ratios of 0.3 and 1.5 respectively). There are 1000 stars in each star-forming region, half of which have planets initially placed at either 30 AU or 50 AU.

The dynamical evolution of the star-forming regions is followed for 10 Myr, and we focus on the orbital properties of stolen planets (that have been directly exchanged between stars during an encounter), and how these compare to that of captured free-floating planets and planets that remain bound to their original star.

Our main results are summarised as follows:

(i) We find that planet theft and capture should be seen as two distinct mechanisms, and should therefore be treated and analysed as such wherever feasible. Our evidence for this is twofold. First, we find that the number of stolen and captured planets is a strong function of the initial conditions. In our sub-virial simulations, when the initial semimajor axis is lowered, the number of stolen planets increases, while the number of captured planets decreases. Second, we find that the orbital distributions of stolen and captured planets are distinct. The evidence of these differences is lost when stolen planets are categorised together with captured ones.

(ii) The orbital properties of stolen, captured, and preserved planets are distinct enough that these characteristics could be used to distinguish their formation channel if an estimate of the initial conditions of their star-forming region are known. Although there is overlap between orbital property distributions, combining semimajor axis and eccentricity data could observationally distinguish populations of stolen, captured, and preserved planets that were born in high density star-forming regions. For planets that have formed in such regions, the semimajor axis distribution can separate captured planets from those that are stolen and preserved, and eccentricity can then separate stolen planets from those that are preserved. If available, inclination data would also be useful in distinguishing planets that have been captured or stolen from another system. This analysis could be performed on populations of planets as a whole to estimate the frequency of each type of planet, or on individual systems to estimate the probability that a planet is stolen, captured, or has remained orbiting in its original system.

(iii) Regardless of the initial conditions, we find that a planet with a semimajor axis of $\gtrsim$500 au is mostly likely a captured planet. And comparing our orbital property results to Planet 9's predicted orbital range of a $\sim$ 400 – 800 AU and e $\sim$ 0.2 – 0.5 suggests that, should it exist, Planet 9 is most likely to have been captured, rather than stolen.

(iv) The projected separation distribution of exoplanets found by direct imaging is most consistent with our captured planets in terms of their semimajor axis distribution (although the direct imaging data are likely to be biased and incomplete). There is debate about the formation mechanism of exoplanets, especially those on wide orbits, and our results suggest that they may be captured planets, as has been suggested by previous studies (Perets & Kouwenhoven, 2012).

(v) We find that theft and capture are relatively common, with ~2% of planets being in stolen systems, and ~2% in captured systems at 10 Myr. The likelihood of planet theft and capture should therefore not be seen as negligible, especially for star-forming regions which may have had relatively dense initial conditions, as simulated here.

(vi) Smaller (30 AU) initial semimajor axes lead to more stolen planets than captured ones after 10 Myr, whilst larger (50 AU) initial semimajor axes lead to more captured planets than stolen ones. This suggests that the outcome of dynamical interactions has a strong dependence on the planet's semimajor axis.

(vii) In simulations where all of the planets are initially free-floating, rather than bound to a star, the incidence of planet theft is negligible. This can give the false impression that planet theft is very rare, and negligible compared to capture, when this is not the case in simulations where the planets are all initially bound to stars.

(viii) In general, comparing our results to that of other papers illustrates the significant effects that initial conditions can have on young planetary systems. These interactions can be not only destructive, but also lead to the creation of new and unique planetary systems.

Chapter 5

Can Jupiters form before they are ejected?

The work in this chapter is in preparation for submission to the Monthly Notices of the Royal Astronomical Society Letters as Daffern-Powell & Parker (2022).

5.1 Summary

External photoevaporation by nearby massive stars within a star-forming region can truncate and destroy protoplanetary disks. Where this happens rapidly, giant planet formation can either be hindered or stopped entirely, such that some planets may grow to be super-Earth cores rather than gas-giants. And some may not grow to planet-mass at all in cases where severe photoevaporation destroys the disk almost immediately, before the dust grains decoupled from the gas, meaning that they may also be dispersed along with the gas.

In this Chapter, we investigate the effects that the photoevaporation of protoplanetary disks may have on the results of dynamical simulations of planets in star-forming region, such as our own in the previous Chapter. We do this by running *N*-body simulations of planets in star-forming regions, where we include protoplanetary disks and the effects of photoevaporation in a post-processing analysis.

We find that the majority of stars that are disrupted, captured, stolen, or free-floating after 10 Myr may not have been able to fully form, as their disks have already been truncated to distances smaller than their semimajor axis at the time that they were first disrupted. Furthermore, some captured, stolen, and free-floating planets may not have been able to form at all, as their disks are significantly truncated almost immediately.

5.2 Introduction

In the previous chapters we have discussed how the high local densities in massive star-forming regions leads to dynamical interactions that are destructive to planets and their protoplanetary disks. These massive star-forming regions are also likely to contain massive stars, whose ultraviolet radiation can heat protoplanetary disks enough to truncate and destroy them through photoevaporation.

As discussed in Section 1.5.2, photoevaporation is the primary destruction mechanism of protoplanetary disks in star-forming regions that contain at least one massive star (Winter, et al., 2018b), and this destruction can happen rapidly, with most disks in star-forming regions being destroyed within a few Myr (Williams & Cieza, 2011; Richert, et al., 2018). This rapid and intense destruction can have significant effects on planets that are forming around nearby stars. In the most extreme cases, a protoplanetary disk may be destroyed almost immediately, before the dust grains have decoupled from the gas, meaning that they may also be dispersed (Adams, et al., 2004). The formation of planet-sized objects may then be prevented entirely in these disks. In other cases, planet formation may be halted or stunted, leading to less massive planets without a gaseous envelope, where gas giant planets may have otherwise been able to form. This means that the process of external photoevaporation can be a central aspect of the evolution of some planetary systems.

The processes of photoevaporation and dynamical evolution are closely linked by the star-forming environments. It is the same high densities that cause the sometimes extreme dynamical evolution of planetary systems that also make photoevaporation more likely. Although young star-forming regions contain a high level of extinction which could shield disks from photoevaporation, Dale et al. (2012) show that massive stars quickly clear out large-scale cavities.

There is a significant assumption in the previous chapter, which is that the gas giant planets would have been able to form on orbits of 30-50 AU. However, if the protoplanetary disks were already significantly depleted through photoevaporation, there is a question of whether these exoplanets could have formed to begin with.

Despite this, studies that investigate the dynamical evolution of planets often only include dynamical evolution within their simulations. This is in part in order to isolate the effects that are being studied, but is also due to constraints of the *N*-body method. However, it is possible to run either hybrid *N*-body simulations which include the hydrodynamic evolution of protoplanetary disks (Rosotti, et al., 2014), or a concurrent analysis of disk evolution by photoevaporation alongside dynamical evolution (Scally & Clarke, 2001; Adams, et al., 2004; Winter, et al., 2018b; Concha-Ramírez, et al., 2019; Nicholson, et al., 2019; Parker, et al., 2021a). When a concurrent analysis is used, the effects of photoevaporation on protoplanetary disks can be run as a post processing calculation. The photoevaporation analysis can then be used to add context to the results that are obtained at the end of the *N*-body simulation.

In this Chapter we follow the evolution of planets that are free-floating, captured, stolen, or disrupted at the end of 10 Myr simulations, in the same way as we did in the previous Chapter. However, we now run analysis of disk evolution through photoevaporation concurrently. We then investigate whether the planets that have been disrupted would likely have been able to form, or if their protoplanetary disks are truncated by photoevaporation to the extent that there is no disk remaining at the distance where the planet orbits.

5.3 Methods

5.3.1 *N*-Body Simulations

Similarly to the previous Chapter, we run simulations that contain 1000 stars within a radius of 1 pc. Half of the stars initially have Jupiter-mass planets placed at 30 AU. During the post processing analysis, each planet-hosting star initially has a protoplanetary disk with radius, $r_{\mathrm{disk}} = 50$ AU. We use a fractal dimension of $D = 1.6$ for all of the simulations here.

The two sets of simulations discussed in this Chapter differ by only their virial ratio in terms of their initial conditions; the first set is initially sub-virial with $\alpha = 0.3$, and the second is initially super-virial with $\alpha = 1.5$. These will be referred to as the sub-virial and super-virial simulations, respectively. 20 realisations of each simulation are run.

Snapshots of *N*-body data are output every 0.01 Myr, as before.

5.3.2 Photoevaporation

The photoevaporation post-processing analysis is calculated every 0.001 Myr, which is sufficient to accurately follow the evolution of the protoplanet disks, as found by Parker et al. (2021) (their Appendix A). The subroutine that performs the photoevaporation post-processing was written by Richard Parker, and follows the method in Parker et al. (2021). This is described as follows.

The FUV and EUV luminosities for each massive star in the snapshot are taken from Armitage (2000) who use the stellar wind and atmosphere models of Schaller et al. (1992) and Buser & Kurucz (1992), and assume an age of 1 Myr for the massive stars. This age assumption is seen as reasonable due to the rapid main sequence evolution of the massive stars that dominate the UV radiation field within star-forming regions (Armitage, 2000). The luminosities are summarised in Armitage (2000) their Figure 1.

For every star with a disk, the disk mass loss due to EUV photoevaporation, $\dot{M}_{\mathrm{EUV}}$, is then calculated using Equation 5.1 from Johnstone et al. (1998):

$$\dot{M}_{\mathrm{EUV}} \cong 8 \times 10^{-12} r^{\frac{3}{2}} \sqrt{\frac{\Phi_j}{d^2}}\ \mathrm{M_{\odot} yr^{-1}} \qquad 5.1$$

where d is in units of pc, r in units of au, and Φ_j is the total EUV ionising photon luminosity from all of the massive stars. Values of Φ are from observations presented in Vacca et al. (1996) and Sternberg et al. (2003).

To calculate the disk mass low due to FUV, the FUV flux is summed across j=1 to N massive stars, as in 5.2. This is done for both FUV and EUV emission according to equation 5.2:

$$\sum_{j=1}^{N} F_{\mathrm{FUV,}} = \frac{L_{\mathrm{FUV}}}{4\pi d^2} \qquad 5.2$$

The mass loss due to FUV photoevaporation is then calculated using the `FRIED` grid, presented in Haworth et al. (2018). The `FRIED` grid contains disk mass loss rates for discrete combinations of stellar mass, disk mass, disk radius, G_0 (background flux), and disk surface density, Σ. The nearest values of stellar mass and disk radius are chosen, and then the values of mass loss are interpolated over the disk radius using linear interpolation. This interpolation is done with respect to the disk mass before it has been photoevaporated in the current timestep.

There is currently no consensus on the radial distribution of disk surface densities (Miotello, et al., 2022). This includes in what ways the radial structure would be affected and vary between disks that have undergone different amounts of photoevaporation. In order to reduce the disk mass in accordance with the mass loss rate obtained from the `FRIED` grid, we therefore follow the standard prescription that was introduced by Haworth et al. (2018) as part of the FRIED grid method and is used throughout other studies (e.g. Haworth & Clarke, 2019; Parker, et al., 2021a; Parker, et al., 2021b).

In this prescription (Haworth, et al., 2018), a truncated power law profile is used to describe the surface density, as given in Equation 5.3:

$$\Sigma(R) = \Sigma[1\mathrm{AU}] \left(\frac{R}{\mathrm{AU}}\right)^{-1} \qquad 5.3$$

where,

$$\Sigma[1\mathrm{AU}] = \frac{1}{2\pi(1\mathrm{AU})}\frac{M_{\mathrm{disk}}}{R_{\mathrm{disk}}} \qquad 5.4$$

In this way, mass is assumed to be lost from the outer edge of the disk, and the disk radius is then reduced by the same factor as the decrease in mass (as in Haworth et al., 2018; Haworth & Clarke, 2019).

Viscous spreading is not yet included in the analysis. The likely effects of this are discussed in Section 5.4. We also do not include disk truncation by stellar fly-bys. However, photoevaporation is generally the dominant form of disk truncation. And disk truncation would not be expected to have a significant effect below stellar densities 10 $M_{\odot}$ pc^{-3}, over timescales of at least ~3 Myr, which are conditions that our simulations do not reach these densities.

Figure 5.1 shows the G_0 value that stars/ protoplanetary disks in our simulations experience over time. This shows the average G_0 value experienced by all disks (thick solid black line), the interquartile range (dashed black lines), the upper and lower limit G_0 values (dotted lines), and the G_0 values experienced by 20 random stars (coloured lines), for three random realisations of our initial conditions.

The FRIED grid has an upper limit G_0 value of 10^4. Figure 5.1 shows that the average G_0 value, the G_0 experienced by the 20 random stars, and the upper interquartile range is below this limit for the majority of the time during our simulations. However, the G_0 that individual stars experience in our simulations can exceed this. The highest G_0 value experienced by any star is $\gtrsim 10^{10}$ across or simulations. However, the highest G_0 value is usually set by a star that enters a close binary with a massive star, and is therefore not generally representative of the G_0 field across the region as a whole.

In cases where the G_0 value experienced by a disk exceeds the limits of the FRIED grid we use the largest value from the FRIED grid. This is in line with other studies (e.g. Parker, et al., 2021), and means that the amount of photoevaporation experienced by the disks in this study is a lower limit.

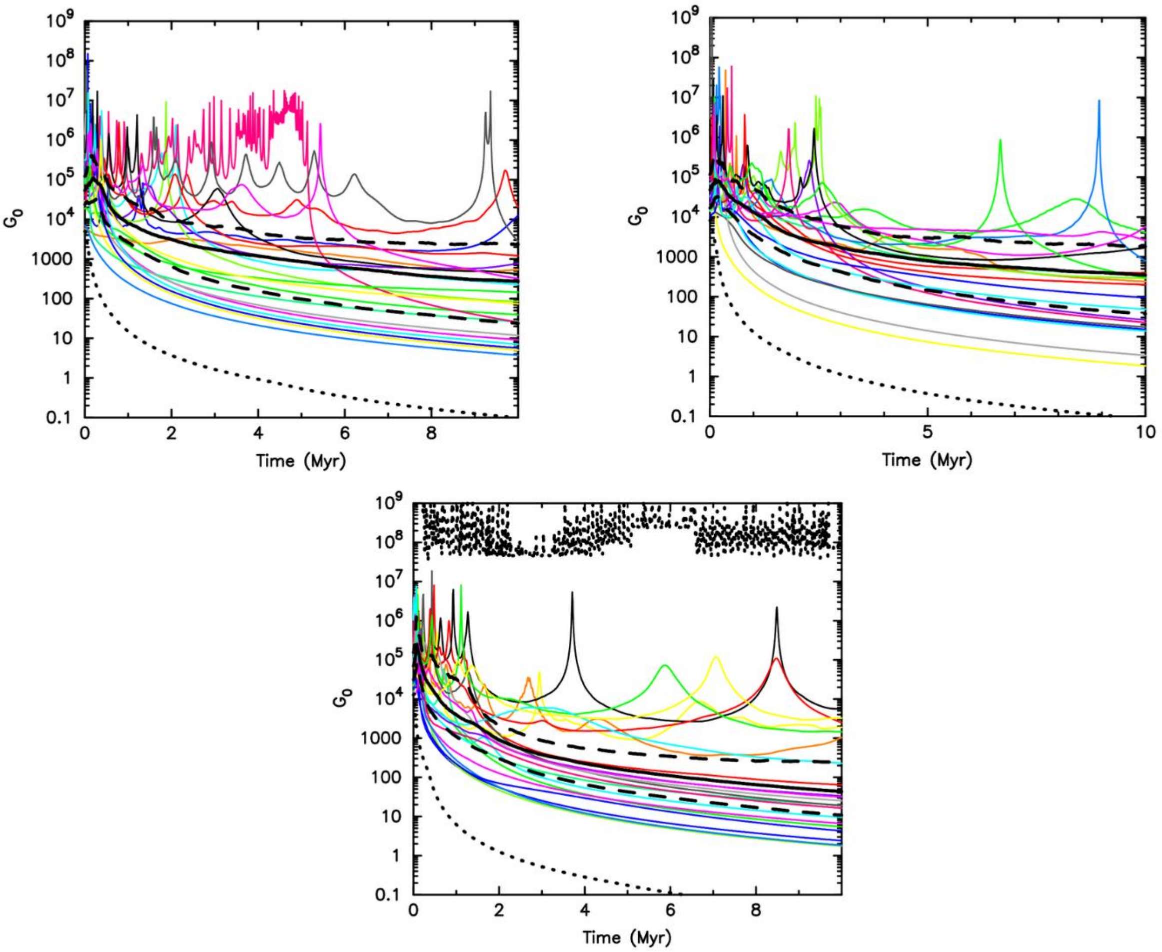

Figure 5.1 The G_0 value experienced by stars over time in 3 (chosen at random) realisations of our simulations. The G_0 values for 20 individual stars (also chosen at random) are shown as the coloured lines. The average G_0 value is a thick black line, the interquartile ranges are shows as dashed lines, and the upper and lower limit values of G_0 are dotted lines.

5.3.3 Analysis

Following the *N*-body simulation and photoevaporation post-processing, I analyse the dynamical evolution of each planet and the evolution of each disk due to photoevaporation.

I then investigate the disk evolution for planets that have been dynamically disrupted during the 10 Myr *N*-body simulation. Disruption is again defined according to the definition adopted in Parker & Quanz, 2012 (a change in semimajor axis of more than 10%, or eccentricity increased above 0.1). Some of these disrupted planets become stolen, captured, and free-floating. So, I identify the final orbit type of each planet in my analysis by following each planet in the same way as in the previous Chapter. The orbit types analysed for this project are stolen, captured, free-floating, and disrupted, where disrupted planets are those that remain bound to their original star but have had their orbit disrupted in terms of semimajor axis or eccentricity.

In particular, I find the snapshot and time at which the planet's orbit is first disrupted and the disk radius at that snapshot. The planets semimajor axis and disk radius at this time are also compared. This is not the end of the orbit disruption for each of these planets, and their orbits may continue to be disrupted and change over time during the simulations. However, we are interested in planets whose orbits have been disrupted in any way, so we plot data corresponding to the beginning of their orbit disruption.

5.4 Results & Discussion

5.4.1 Disk Truncation Over Time

Figure 5.2 shows the time that planets first have their orbit disrupted compared to the radius of their protoplanetary disk at that time, for the sub-virial initial conditions. These results are shown for 20 realisations in four separate panels for planets that are disrupted, captured, stolen, and free-floating at the end of the 10 Myr simulations. Figure 5.3 shows the same for the super-virial initial conditions.

As expected, the majority of planets that have their orbits disrupted are initially disrupted early on in the simulations, within the first 0.1 Myr. This is consistent with the findings of previous studies (e.g. Jaehnig et al., 2015; Sills et al., 2018), as well as that of our own in Chapter 3 and Chapter 4, where we find that the majority of the dynamical mixing occurs at early times.

The later on in the simulation that a planet is disrupted the more likely its disk is to have been more severely truncated. However, even the majority of planets that are disrupted at early times, before 1 Myr, have truncated disks. In some cases, planets that are disrupted in the first 0.1 Myr already have disks that are truncated down to only a few AU, or have been destroyed entirely, by the times that they become disrupted. These planets, especially, may not have been able to fully form in order to become observable disrupted, captured, stolen, or free-floating giant planets, because their parent disks are severely truncated or destroyed at such early times.

This is of relevance to studies, such as our own in Chapter 4, which investigate populations of planets that have had their orbits significantly changed. For example, some of the planets that are free-floating at 10 Myr, in the bottom panels of Figure 5.2 and Figure 5.3, have had their disks entirely destroyed within <0.1 Myr. These planets would not have had time to fully form into giant planet mass object, and may not have been able form at all.

Meanwhile, planets for which this happens but at later times, would most likely have formed a planet sized object, but not had time to accrete enough mass to become a gas giant before the gas component of their disk was depleted. These planets may therefore be free-floating, but not as the Jupiter-mass planets that are simulated. Such super-earth, or low mass free-floating

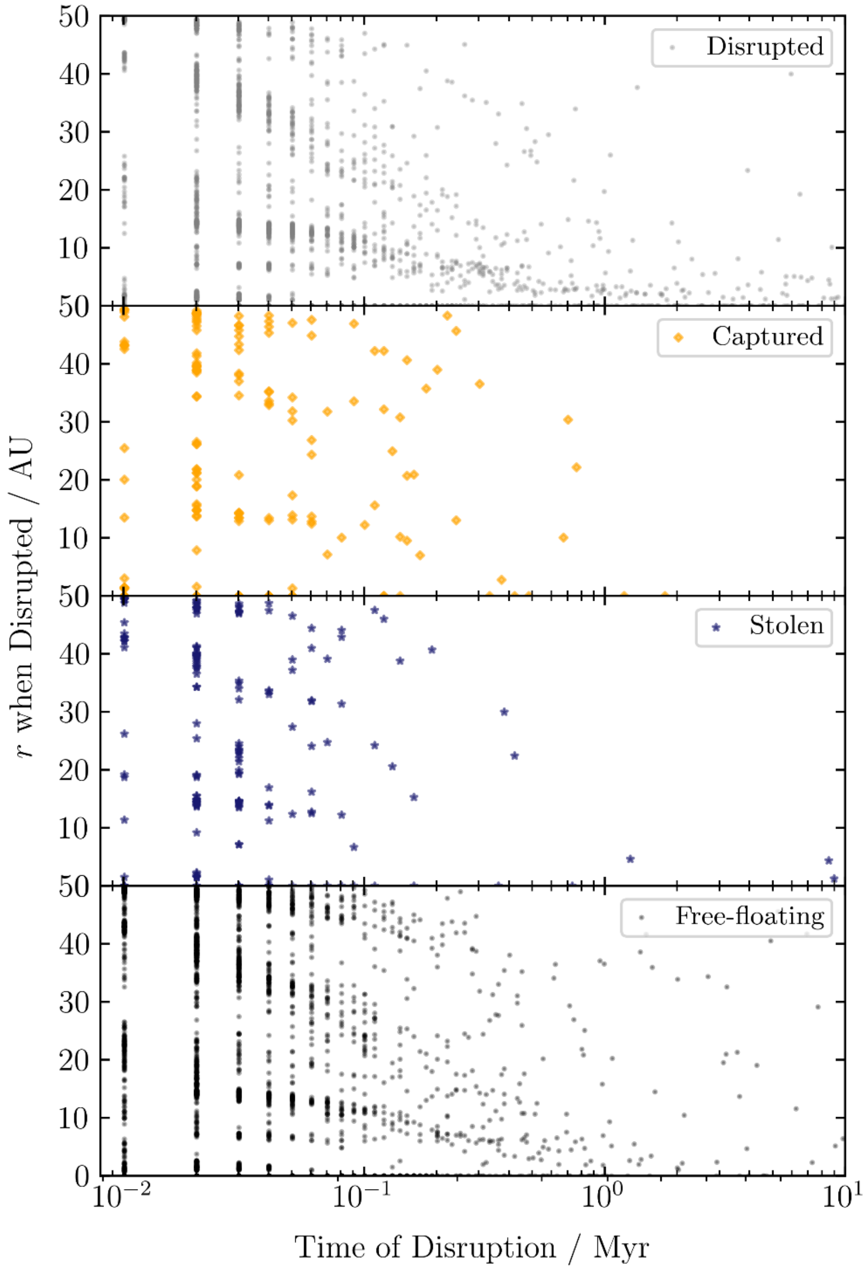

Figure 5.2 The radius of the protoplanetary disk when a planet's orbit is first disrupted, versus the time at which this happens. Results are plotted for planets which are disrupted, captured, stolen, or free-floating at the end of the 10 Myr simulation in grey, orange, blue, and black, respectively. These are shown for 20 realisations of the initially sub-virial $\alpha = 0.3$ simulations.

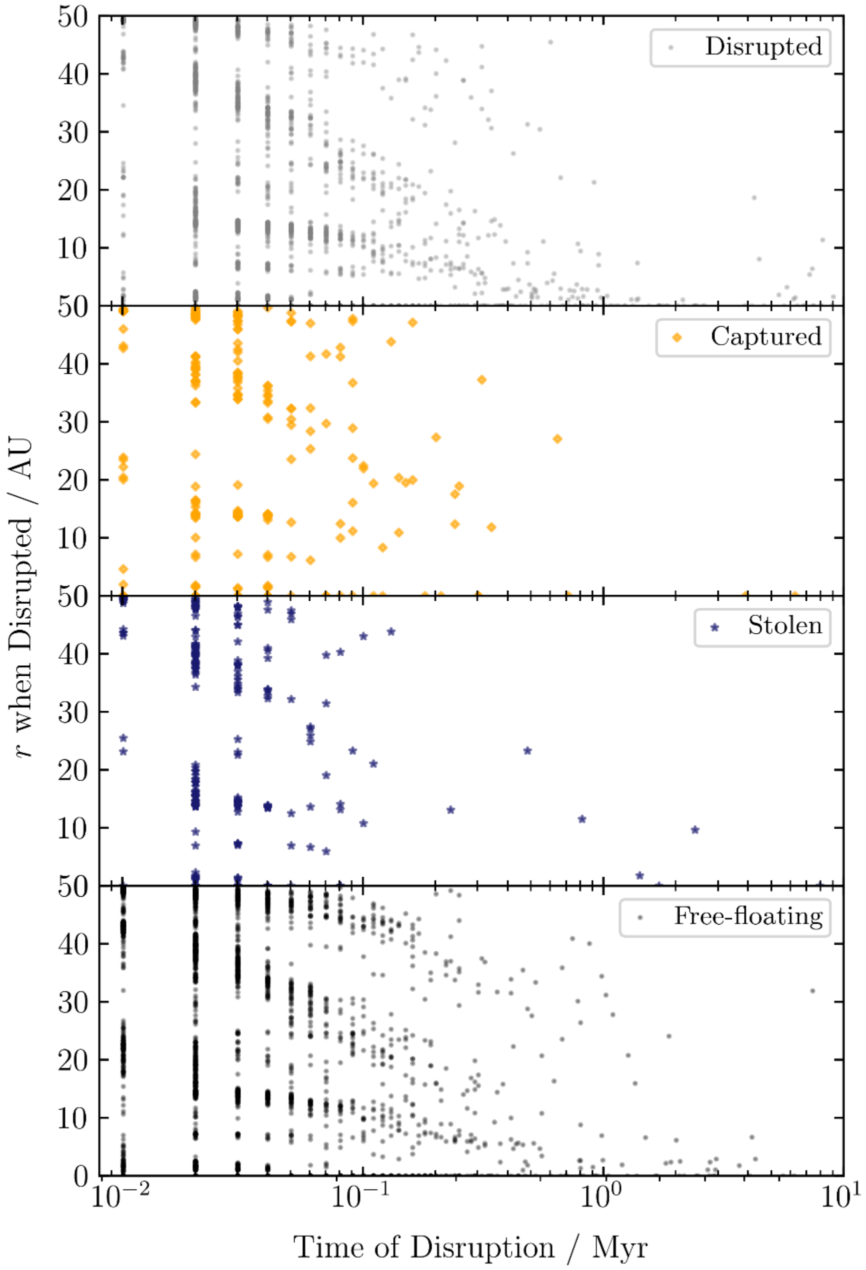

Figure 5.3 The radius of the protoplanetary disk when a planet's orbit is first disrupted, versus the time at which this happens. Results are plotted for planets which are disrupted, captured, stolen, or free-floating at the end of the 10 Myr simulation in grey, orange, blue, and black, respectively. These are shown for 20 realisations of the initially super-virial $\alpha = 1.5$ simulations.

planets would likely need to be discovered through gravitational micro-lensing, as direct imaging is biased towards detecting higher mass objects.

A comparison of Figure 5.2 and Figure 5.3 shows that the initial virial ratio does not have as significant an effect on the results as might be expected. This implies that whether the region as a whole is initially expanding or contracting does not have a significant effect, and it is instead the initial density and substructure that primarily determines the proportion of planets whose disks are already truncated at the time that they become disrupted. This is consistent with previous results (Nicholson, et al., 2019; Parker, et al., 2021a).

5.4.2 Disk radius compared to semimajor axis

Figure 5.4 compares the disk radius and semimajor axis at the time that a planet is first disrupted for the sub-virial initial conditions. The planets shown are again divided into their final orbit type, as shown by different markers. Figure 5.5 shows the same for the super-virial initial conditions. Planets that are plotted as disrupted but lie around the $a = 30$ AU value have been disrupted in terms of eccentricity but not semimajor axis in the snapshot shown. Both figures include black/grey lines, showing where the disk radius and semimajor axis values are equal.

The majority of planets have already had their disks truncated below their semimajor axis ($r < a$) in the snapshot that they first become disrupted. For the sub-virial initial conditions this is 73.8% of planets that are disrupted, captured, stolen, or free-floating at 10 Myr. For the super-virial initial conditions this is 75.5%. This remains the case for all types of final planetary orbit; whether a planet is disrupted, captured, stolen, or free-floating at 10 Myr, its likelihood of having $r < a$ at the time that it first becomes disrupted is between 73-76% for the sub-virial initial conditions, and between 66-80% for the super-virial initial conditions. These planets would likely have not had time to finish fully forming before being disrupted, since the majority of orbit disruption happens within the first Myr.

For the super-virial initial conditions, it is the captured planets that are most likely (80%) to have $r < a$ in the snapshot that they become disrupted, and the stolen planets that are the least likely (66%). This may be due to differences in the mechanisms through which theft and capture

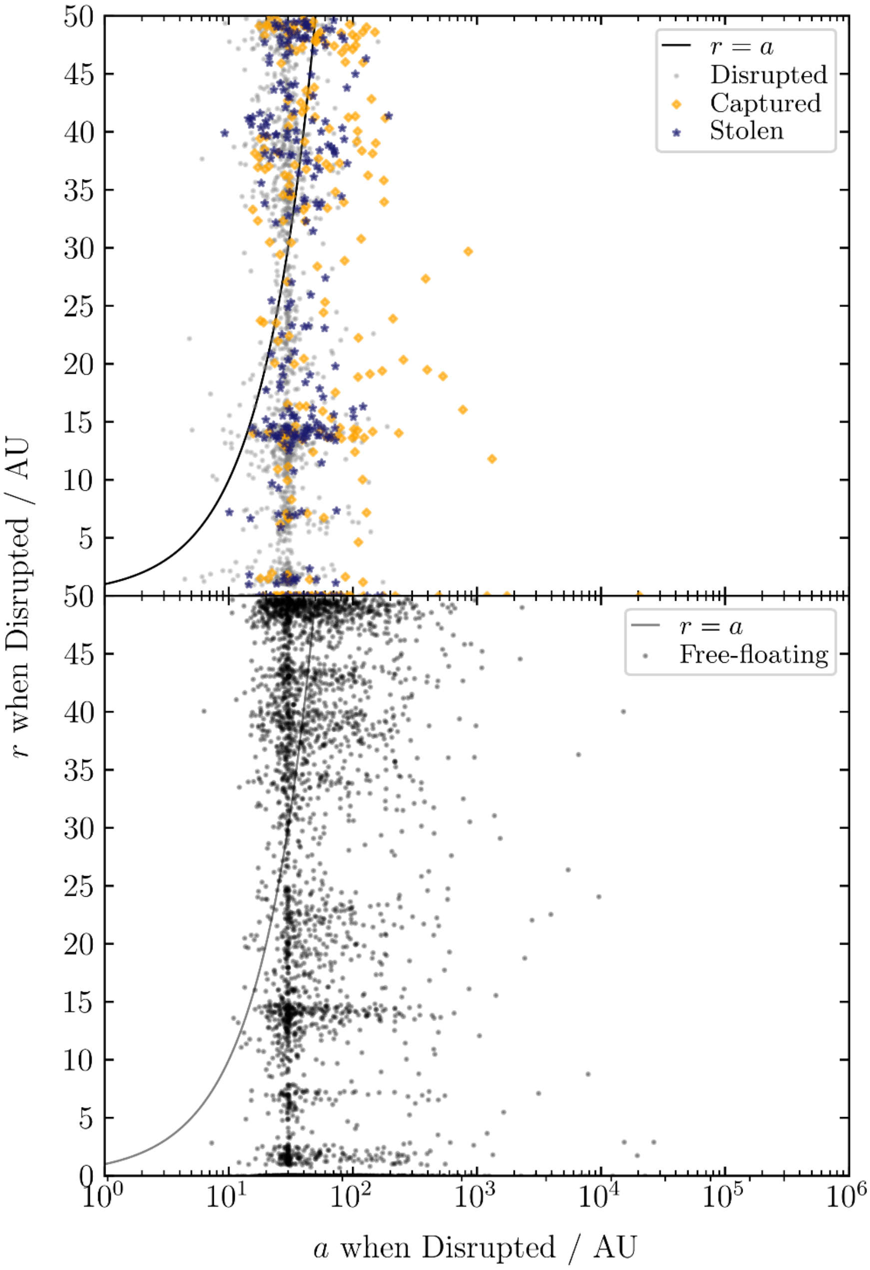

Figure 5.4 The radius of the protoplanetary disk when a planet's orbit is first disrupted, versus its semimajor axis at that time. The $r = a$ line is shown as a black line in the top panel, and a grey line in the bottom panel. Results are plotted for planets which are disrupted, captured, stolen, or free-floating at the end of the 10 Myr simulation in grey, orange, blue, and black, respectively. These are shown for 20 realisations of the initially sub-virial $\alpha = 0.3$ simulations.

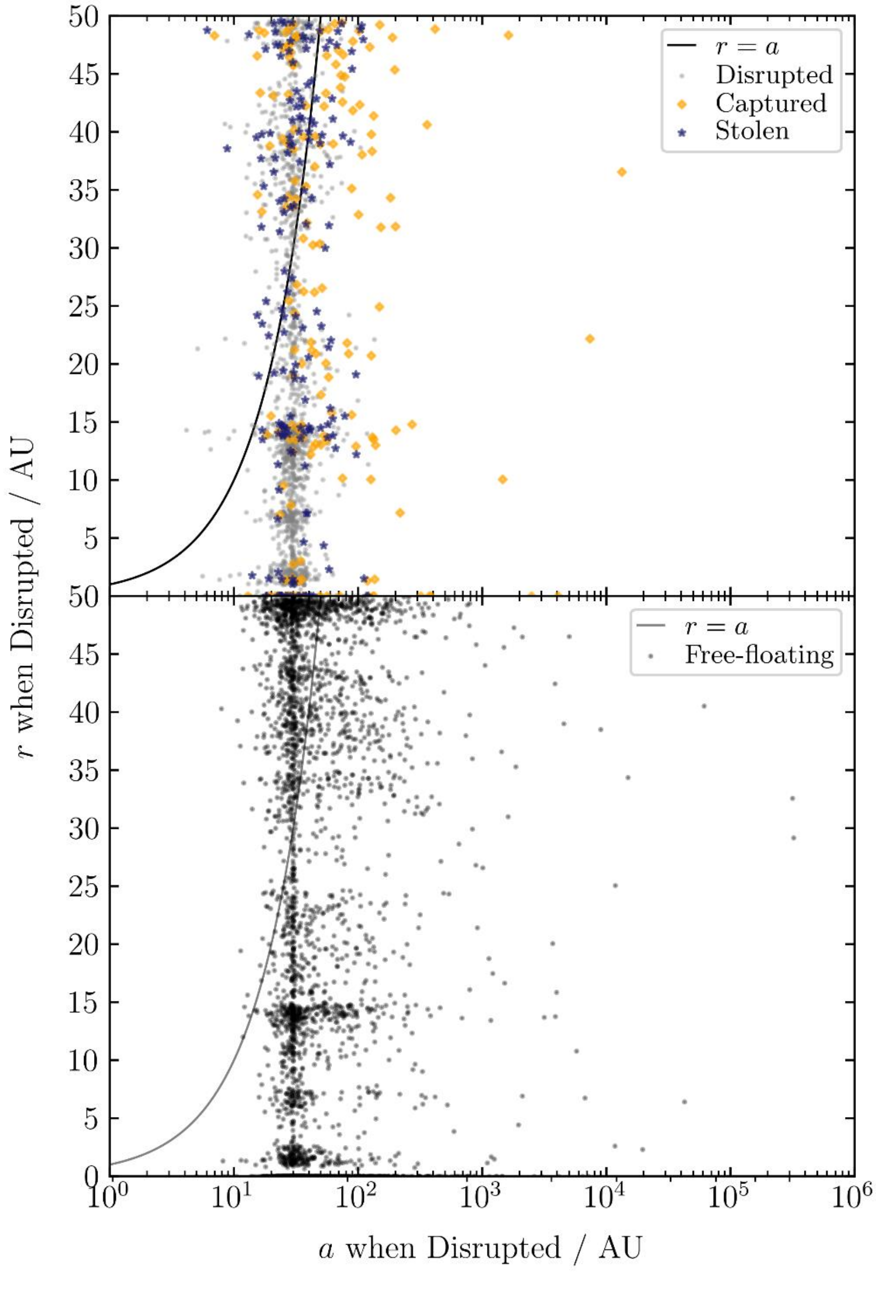

Figure 5.5 The radius of the protoplanetary disk when a planet's orbit is first disrupted, versus its semimajor axis at that time. The $r = a$ line is shown as a black line in the top panel, and a grey line in the bottom panel. Results are plotted for planets which are disrupted, captured, stolen, or free-floating at the end of the 10 Myr simulation in grey, orange, blue, and black, respectively. These are shown for 20 realisations of the initially super-virial $\alpha = 1.5$ simulations.

occur, and that planets can be stolen at earlier times than they can be captured. Stolen planets therefore have an earlier time of first disruption than captured planets, on average, when the disks are less likely to have been as truncated.

In reality, the edges of the disk are less dense, especially after experiencing photoevaporation, which means that planet formation is unlikely in the outer edges of the disk. However, the $r = a$ line remains a useful guide for judging whether a disk has been truncated to an extent that would be detrimental to planet formation, as it can be seen as a lower limit for the point at which disk truncation would be detrimental.

The data in both Figure 5.4 and Figure 5.5 are grouped around certain values of disk radius. This is caused by 'pile-ups' when the disk mass, and therefore radius, is initially reduced very rapidly due to photoevaporation. For example, if a 100 AU disc initially loses 88% of its mass, its radius will be reduced to 12 AU. Because the FRIED grid contains discrete rather than continuous values, the library of discs with radii of 10 AU will be used. The 10 AU disks have larger surface densities, because surface density is proportional to the inverse square of the disk radius, and will therefore be more resistant to photoevaporation. The subsequent photoevaporation of the disc then proceeds much more slowly than when the disk was 100 AU. This causes the disks to gather around certain values for longer, thereby causing the grouping in Figure 5.4 and Figure 5.5.

Together, these results show that some of the giant-mass planets that N-body simulations find to be stolen, captured, free-floating or on wide orbits that are consistent with some observed exoplanets, may not have been able to grow to gas giant masses or form at all. This directly affects the numbers of stolen, captured, and disrupted planets that are formed, and may also affect the distributions of their properties.

This is not an entirely separate effect from the dynamical interactions that produce these extreme orbits, but is a direct result of the same high densities that cause the dynamical interactions which produce them. This shows the mixed and complex effects that high density star-forming regions can have on the planet formation within them.

If viscous spreading had been included in these simulations the disks would be destroyed faster. This is because the disk radii would be increased, for the same mass, thereby reducing their surface density and making them even more susceptible to photoevaporation. This would likely cause more of our simulated planets to have $r < a$ in the snapshot that they first become disrupted.

5.5 Conclusion

We have used a combination of N-body simulations and photoevaporation post-processing using the `FRIED` grid method to investigate the effects that photoevaporation may have on the formation of giant planets which go on to have their orbits significantly changed.

Our main conclusions are summarised as follows:

(i) The same high densities that lead to the disruption of planetary orbits and the creation of free-floating, stolen, and captured planets can also be detrimental to planet formation. This means that the giant-mass planets that other studies, such as our own in the previous Chapter, identify as having their orbits altered may not have been able to form. Alternatively, they may have had their formation stunted, and therefore be super-Earth mass giant planet cores rather than gas giants.

(ii) We find that, at the time that a planet first becomes disrupted, its likelihood of having a semimajor axis within its protoplanetary disk is ~25%. Since the time of first disruption tends to be very early (before 0.1-1 Myr), this implies that a significant amount of planets would not be able to fully form before becoming identifiable as disrupted, both in simulations and observations.

(iii) Those planets that would not be able to form at all would not to contribute to the observed populations of exoplanets that are free-floating, or orbiting at very large separations.

(iv) For planets that go on to be free-floating, after having their formation stunted, this means that they would likely require gravitational lensing to be detected, as direct imaging is biased towards more massive planets.

(v) Planets that are stolen at 10 Myr are more likely to remain within the extent of their disk at the time that they are first disrupted than those that are captured planets at 10 Myr. This is likely due the average time of theft being earlier than that of capture.

(vi) The virial ratio of a star-forming region does not appear to have a significant effect on our results, suggesting that the initial densities are the primary factor that determines the amount of disk destruction and truncation by photoevaporation. This is consistent with previous results (Nicholson, et al., 2019; Parker, et al., 2021a).

Chapter 6

Conclusions

We have performed and analysed N-body simulations of young, substructured star-forming regions. The main aim of this thesis has been to investigate the effects that dynamical interactions in star-forming regions can have on the bodies within them.

6.1 The Dynamical Evolution of Fractal Structures in Star-Forming Regions

It is necessary to be able to quantity substructure in star-forming regions in order to be able to study the effects that their substructured nature can have on young stars and planets. It is therefore important to understand the limitations of the methods that are used to quantify the spatial distributions of stars, and when it is appropriate to use them.

The Q-parameter method is used extensively to quantify the substructure of stars and gas in star-forming regions, as well as older clusters and associations. The interpretation of the Q-parameter often relies on comparing observed values of Q, $\bar{m}$, and $\bar{s}$ to idealised synthetic geometries. However, some observed star-forming regions do not correspond to either centrally concentrated or box-fractal synthetic geometries in terms of their values of $\bar{m}$ and $\bar{s}$. This disparity is highlighted by Lomax et al. (2018) who conclude that there is either a problem with the Q-parameter method, synthetic regions, or both, because some areas of the $\bar{m}$ vs $\bar{s}$ plot are populated by observed star-forming regions but not synthetic geometries. This would have implications for many studies as centrally concentrated and box-fractal initial conditions are commonly used as initial conditions in N-body simulations.

In Chapter 3, *The Dynamical Evolution of Fractal Star-Forming Regions*, we perform N-body simulations of young star-forming regions. We use a range of box-fractal initial conditions that correspond to the estimated initial conditions of IC 348, the ONC, and NGC 1333. These synthetic star-forming regions are evolved for 10 Myr in order to investigate whether the disparity between observed star-forming regions and synthetic ones can be explained by their dynamical evolution.

We find that, although the initial conditions of our synthetic star-forming regions do not correspond to the $\bar{m}$ and $\bar{s}$ values of the observed regions, they do evolve to populate the same areas of the $\bar{m}$ vs $\bar{s}$ plot over time as they dynamically evolve. Star-forming regions can therefore be consistent with having evolved from fractal geometries in terms of $\bar{m}$ and $\bar{s}$. In this way, the disparity highlighted by Lomax et al. (2018) can be seen as being due to comparing observed star-forming regions, which are a few Myr old, to unevolved synthetic regions, which correspond to younger and less dynamically evolved star-forming regions, and may not exist in nature.

We therefore conclude that the lack of correspondence between some observed star-forming regions and unevolved synthetic geometries should not be seen as a problem with the Q-parameter method. However, observed values of Q, $\bar{m}$, and $\bar{s}$ should not be directly compared to idealised geometries that have not undergone any dynamical evolution.

6.2 Theft and Capture in Star-Forming Regions

Gravitational interactions in star-forming regions are capable of disrupting and destroying planetary systems, as well as creating new ones. This is especially the case for relatively dense and substructured star-forming regions, where the ‘clumps’ of substructure have higher local densities than that of the region as a whole. In particular, a planet can be stolen, where it is directly exchanged between passing stars during an interaction; or captured, where a planet is first ejected from its birth system and is free-floating, before being captured by a passing star.

In Chapter 4, *Theft and Capture in Star-Forming Regions*, we use N-body simulations of planets in dense, substructured star-forming regions. We follow the dynamical evolution of each planet to investigate the orbital properties of stolen and captured planets, and how these compare to the orbital properties of each other, as well as planets that continuously orbit their original star (preserved planets).

We find that, although there is overlap between the orbital property distributions of stolen, captured, and preserved planets, combining semimajor axis and eccentricity data could distinguish these three populations. Semimajor axis can distinguish captured planets from those that are stolen and preserved, and eccentricity can then distinguish stolen from preserved planets. In principle, these differences could be used to determine whether observed exoplanets have likely formed in situ or have been stolen or captured.

6.3 Can Jupiters form before they are ejected?

The same high densities that can cause planets to be captured, stolen, disrupted, or ejected, can also lead to increased external photoevaporation of their protoplanetary disks. This photoevaporation can cause disks to be truncated and destroyed to an extent that planet formation can be hindered or halted. Of particular interest here, is whether the gas-giant planets that have their orbits significantly changed in Chapter 4 would have been able to fully form, or whether photoevaporation would have been detrimental to their formation. This is also of relevance to other studies, as dynamical simulations of planetary orbits in star-forming regions do not generally include the effects of photoevaporation.

In Chapter 5, *Can Jupiters form before they are ejected?*, we perform *N*-body simulations of substructured star-forming regions in order to follow the dynamical evolution of the planets within them. We then follow the evolution of each star's disk due to the effects of external photoevaporation in a post-processing analysis.

We find that ~75% of the planets that have their orbit significantly changed by dynamical interactions already have a semimajor axis greater than their disk radii at the time of first disruption. Their orbits tend to be first disrupted very early on, within the first 0.1-1 Myr. This therefore implies that the majority of planets that have their orbits disrupted or destroyed likely would not have been able to fully form, or form at all, before this disruption occurs. Those that have their formation hindered by photoevaporation may form as super-Earth-mass cores, rather than gas giants. Planets that have their formation hindered before being ejected to become free-floating, would likely need to be discovered through gravitational microlensing, as direct detection is biased towards more massive exoplanets.

6.4 Future Work

The work in this thesis could be both furthered an improved by future research.

Parker & Wright (2018) demonstrate that, although the box-fractal method incorporates velocity substructure, it does not follow Larson's relation for every chosen fractal dimension. In Larson's relation, the velocity dispersion scales with the size of a local region as $\sigma \propto L^{0.38}$. However, in the box fractal method, the velocity dispersion scales as $\sigma \propto L^{3-D}$. This means that, for fractal dimensions of 1.6, 2.0, and 2.6, the velocity dispersion sclaes as $L^{1.4}$, L, and $L^{0.40}$, respectively. Although a fractal dimension of 2.6 therefore approximates the Larson relation, fractal dimensions of 1.6 and 2.0 vary from the Larson relation significantly. The work thoughout this thesis, as well as that of other work which used the box-fractal method, would therefore benefit from the box-fractal method being altered so that it conforms to the Larson relation for every chosen fractal dimension. To do this, part of the programme would need to be rewritten so that the velocity substructure does not depend of the chosen fractal dimension, and is instead less substructured than the spatial substructure.

More specifically, the work in *Chapter 5 Can Jupiters form before they are ejected?* will become more realistic once viscous evolution is included. And future work could involve simulating low density star-forming regions.

The work the work in *Chapter 4 Theft and Capture in Star-Forming Regions*, could be furthered by including binary stars and/or planetary systems with more than one planet in order to investigate how the inclusion of secular interactions affects the results. This could be done in a way that attempts to incorporate a realistic initial distribution of exoplanet orbits.

Across the field of star and planet formation, the direct detection of Planet 9 remains a possibility (Brown & Batygin, 2021). However, its existence may also be also be ruled out by null results from dedicated searches (Brown & Batygin, 2021). Furthermore, studies that investigate the likelihood of Planet 9 having been captured or stolen from another system calculate probability that these mechanisms could produce an orbit in Planet 9's predicted orbital range. The probabilities calculated are therefore dependant on the predicted possible range and will change as this range shrinks or increases. The study of the origin of Planet 9's orbit could therefore benefit from a Bayesian approach, where the probability of Planet 9 having been captured or stolen is calculated given a chosen orbit (Mustill, et al., 2016). Meanwhile, the discovery of more exoplanets will improve our understanding of their orbits, including ways in which our Solar System appears to be unusual.

References

Aarseth, S. J., 1999. From NBODY1 to NBODY6: The Growth of an Industry. *The Publications of the Astronomical Society of the Pacific,* 111(765), pp. 1333-1346.

Aarseth, S. J., 2003. *Gravitational N-Body Simulations: Tools and Algorithms.* Cambridge: Cambridge University Press.

Adams, F. C., 2010. The Birth Environment of the Solar System. *Annual Review of Astronomy and Astrophysics,* 9, Volume 48, pp. 47-85.

Adams, F. C., Hollenbach, D., Laughlin, G. & Gorti, U., 2004. Photoevaporation of Circumstellar Disks Due to External Far-Ultraviolet Radiation in Stellar Aggregates. *The Astrophysical Journal,* 611(1), pp. 360-379.

Adams, F. C., Proszkow, E. M., Fatuzzo, M. & Myers, P. C., 2006. Early Evolution of Stellar Groups and Clusters: Environmental Effects on Forming Planetary Systems. *The Astrophysical Journal,* 4, Volume 641, pp. 504-525.

Adibekyan, V. et al., 2021. On the stellar clustering and architecture of planetary systems. *arXiv e-prints,* 2.p. arXiv:2102.12346.

Allison, R. J. & Goodwin, S. P., 2011. On the formation of trapezium-like systems. *Monthly Notices of the Royal Astronomical Society,* 8, Volume 415, pp. 1967-1976.

Allison, R. J. et al., 2010. The early dynamical evolution of cool, clumpy star clusters. *Monthly Notices of the Royal Astronomical Society,* 9, Volume 407, pp. 1098-1107.

Alves, F. O. et al., 2020. A Case of Simultaneous Star and Planet Formation. *The Astrophysical Journal Letters,* 904(1), p. 6.

Alves, J., Lombardi, M. & Lada, C. J., 2007. The mass function of dense molecular cores and the origin of the IMF. *Astronomy and Astrophysics,* Volume 462, pp. L17-L21.

Anderson, D. R. et al., 2010. WASP-17b: An Ultra-Low Density Planet in a Probable Retrograde Orbit. *The Astrophysical Journal,* 709(1), pp. 159-167.

Anders, P., Baumgardt, H., Bissantz, N. & Portegies Zwart, S., 2009. How well do STARLAB and NBODY4 compare? I. Simple models. *Monthly Notices of the Royal Astronomical Society,* 395(4), pp. 2304-2316.

Anders, P., Baumgardt, H., Gaburov, E. & Portegies Zwart, S., 2012. How well do STARLAB and NBODY compare? II. Hardware and accuracy. *Monthly Notices of the Royal Astronomical Society,* 421(4), pp. 3557-3569.

André, P. et al., 2019. The role of molecular filaments in the origin of the prestellar core mass function and stellar initial mass function. *Astronomy & Astrophysics,* 629(L4), p. 8.

André, P. et al., 2014. From Filamentary Networks to Dense Cores in Molecular Clouds: Toward a New Paradigm for Star Formation. In: H. Beuther, R. S. Klessen, C. P. Dullemond & T. Henning, eds. *Protostars and Planets VI.* Tuscon: University of Arizona Press, p. 27.

André, P. et al., 2010. From filamentary clouds to prestellar cores to the stellar IMF: Initial highlights from the Herschel Gould Belt Survey. *Astronomy and Astrophysics,* 7, Volume 518, p. L102.

Andre, P., Ward-Thompson, D. & Barsony, M., 1993. Submillimeter Continuum Observations of rho Ophiuchi A: The Candidate Protostar VLA 1623 and Prestellar Clumps. *Astrophysical Journal,* Volume 406, p. 122.

Andrews, S. M., 2020. Observations of Protoplanetary Disk Structures. *Annual Review of Astronomy and Astrophysics,* Volume 58, pp. 483-528.

Andrews, S. M., 2020. Observations of Protoplanetary Disk Structures. *Annual Review of Astronomy and Astrophysics,* Volume 58, pp. 483-528.

Andrews, S. M. et al., 2018. The Disk Substructures at High Angular Resolution Project (DSHARP). I. Motivation, Sample, Calibration, and Overview. *The Astrophysical Journal Letters,* 869(2), p. L41.

Andrews, S. M., Rosenfeld, K. A., Kraus, A. L. & Wilner, D. J., 2013. The Mass Dependence between Protoplanetary Disks and their Stellar Hosts. *The Astrophysical Journal,* 771(2), p. 40.

Andrews, S. M. & Williams, J. P., 2007. A Submillimeter View of Circumstellar Dust Disks in ρ Ophiuchi. *The Astrophysical Journal,* 671(2), pp. 1800-1812.

Ansdell, M. et al., 2018. ALMA Survey of Lupus Protoplanetary Disks. II. Gas Disk Radii. *The Astrophysical Journal,* 859(1), p. 21.

Armitage, P. J., 2000. Suppression of giant planet formation in stellar clusters. *Astronomy and Astrophysics,* Volume 362, pp. 968-972.

Armitage, P. J., 2020. *Astrophysics of Planet Formation.* 2 ed. Cambridge: Cambridge University Press.

Arzoumanian, D. et al., 2011. Characterizing interstellar filaments with Herschel in IC 5146. *Astronomy & Astrophysics,* Volume 529, p. L6.

Arzoumanian, D. et al., 2019. Characterizing the properties of nearby molecular filaments observed with Herschel. *Astronomy and Astrophysics,* 1, Volume 621, p. A42.

Ballesteros-Paredes, J. et al., 2020. From Diffuse Gas to Dense Molecular Cloud Cores. *Space Science Reviews,* 216(5), p. A76.

Ballesteros-Paredes, J., Klessen, R. S., Mac Low, M. -M. & Vazquez-Semadeni, E., 2007. Molecular Cloud Turbulence and Star Formation. In: B. Reipurth, D. Jewitt & K. Keil, eds. *Protostars and Planets V.* Tuscon: University of Arizona Press, pp. 63-80.

Ballone, A. et al., 2020. Evolution of fractality and rotation in embedded star clusters. *arXiv e-prints,* 1.p. arXiv:2001.10003.

Bastian, N. et al., 2007. Hierarchical star formation in M33: fundamental properties of the star-forming regions. *Monthly Notices of the Royal Astronomical Society,* 379(4), pp. 1302-1312.

Bastian, N., Gieles, M., Ercolano, B. & Gutermuth, R., 2009. The spatial evolution of stellar structures in the Large Magellanic Cloud. *Monthly Notices of the Royal Astronomical Society,* 1, Volume 392, pp. 868-878.

Bate, M. R., 2009. The dependence of star formation on initial conditions and molecular cloud structure. *Monthly Notices of the Royal Astronomical Society,* 397(1), pp. 232-248.

Batygin, K., Adams, F. C., Brown, M. E. & Becker, J. C., 2019. The planet nine hypothesis. *Physics Reports,* 5, Volume 805, pp. 1-53.

Batygin, K. & Brown, M. E., 2016. Evidence for a Distant Giant Planet in the Solar System. *Astronomical Journal,* 2, Volume 151, p. 22.

Baumgardt, H. & Kroupa, P., 2007. A comprehensive set of simulations studying the influence of gas expulsion on star cluster evolution. *Monthly Notices of the Royal Astronomical Society,* 10, Volume 380, pp. 1589-1598.

Bell, C. P. M. et al., 2013. Pre-main-sequence isochrones - II. Revising star and planet formation time-scales. *Monthly Notices of the Royal Astronomical Society,* 9, Volume 434, pp. 806-831.

Binney, J. & Tremaine, S., 2008. *Galactic Dynamics.* 2nd ed. Princeton: Princeton University Press.

Blaauw, A., 1961. On the origin of the O- and B-type stars with high velocities (the "run-away" stars), and some related problems. *Bulletin of the Astronomical Institutes of the Netherlands,* Volume 15, p. 265.

Bodenheimer, P. & Pollack, J. B., 1986. Calculations of the accretion and evolution of giant planets: The effects of solid cores. *Icarus,* 67(3), pp. 391-408.

Bonnell, I. A. & Bate, M. R., 2005. Binary systems and stellar mergers in massive star formation. *Monthly Notices of the Royal Astronomical Society,* 362(3), pp. 915-920.

Bonnell, I. A., Bate, M. R., Clarke, C. J. & Pringle, J. E., 1997. Accretion and the stellar mass spectrum in small clusters. *Monthly Notices of the Royal Astronomical Society,* 285(1), pp. 201-208.

Bonnell, I. A., Bate, M. R., Clarke, C. J. & Pringle, J. E., 2001. Competitive accretion in embedded stellar clusters. *Monthly Notices of the Royal Astronomical Society,* 323(4), pp. 785-794.

Bonnell, I. A., Bate, M. R. & Zinnecker, H., 1998. On the formation of massive stars. *Monthly Notices of the Royal Astronomical Society,* 298(1), pp. 93-102.

Bonnell, I. A., Smith, K. W., Davies, M. B. & Horne, K., 2001. Planetary dynamics in stellar clusters. *Monthly Notices of the Royal Astronomical Society,* 322(4), pp. 859-865.

Boss, A. P., 1997. Giant planet formation by gravitational instability. *Science,* 1, Volume 276, pp. 1836-1839.

Bressert, E. et al., 2010. The spatial distribution of star formation in the solar neighbourhood: do all stars form in dense clusters?. *Monthly Notices of the Royal Astronomical Society: Letters,* 409(1), pp. L54-L58.

Brown, A. G., 2021. Microarcsecond Astrometry: Science Highlights from Gaia. *Annual Review of Astronomy and Astrophysics,* Volume 59, pp. 59-115.

Brown, M. E. & Batygin, K., 2021. The Orbit of Planet Nine. *The Astronomical Journal,* 162(5), p. 16.

Buckner, A. S. M. et al., 2019. The spatial evolution of young massive clusters. I. A new tool to quantitatively trace stellar clustering. *Astronomy and Astrophysics,* 2, Volume 622, p. A184.

Buser, R. & Kurucz, R. L., 1992. A library of theoretical stellar flux spectra. I. Synthetic UBVRI photometry and the metallicity scale for F- to K-type stars.. *Astronomy and Astrophysics,* Volume 264, pp. 557-591.

Cai, M. X., Portegies Zwart, S., Kouwenhoven, M. B. N. & Spurzem, R., 2019. On the survivability of planets in young massive clusters and its implication of planet orbital architectures in globular clusters. *Monthly Notices of the Royal Astronomical Society,* 11, Volume 489, pp. 4311-4321.

Cartwright, A., 2009. Measuring clustering in 2dv space. *Monthly Notices of the Royal Astronomical Society,* 12, Volume 400, pp. 1427-1430.

Cartwright, A. & Whitworth, A. P., 2004. The statistical analysis of star clusters. *Monthly Notices of the Royal Astronomical Society,* 2, Volume 348, pp. 589-598.

Cassan, A. et al., 2012. One or more bound planets per Milky Way star from microlensing observations. *Nature,* 481(7380), pp. 167-169.

Chabrier, G., Johansen, A. s. b. o., Janson, M. & Rafikov, R., 2014. Giant Planet and Brown Dwarf Formation. In: H. Beuther, R. S. Klessen, C. P. Dullemond & T. Henning, eds. *Protostars and Planets VI.* Tuscon: University of Arizona Press, pp. 619-642.

Chatterjee, S., Ford, E. B., Matsumura, S. & Rasio, F. A., 2008. Dynamical Outcomes of Planet-Planet Scattering. *The Astrophysical Journal,* 686(1), pp. 580-602.

Chen, X. et al., 2013. SMA Observations of Class 0 Protostars: A High Angular Resolution Survey of Protostellar Binary Systems. *The Astrophysical Journal,* 768(2), p. 31.

Clanton, C. & Gaudi, B. S., 2017. Constraining the Frequency of Free-floating Planets from a Synthesis of Microlensing, Radial Velocity, and Direct Imaging Survey Results. *The Astrophysical Journal,* 1, Volume 834, p. 46.

Clarke, C., 1992. Stars arriving two by two. *Nature,* 357(6375), pp. 197-198.

Clarke, C., 2011. The Dispersal of Disks around Young Stars. In: P. Garcia, ed. *Physical Processes in Circumstellar Disks around Young Stars.* Chicago: University of Chicago Press, pp. 356-413.

Clarke, C. J. & Pringle, J. E., 1993. Accretion disc response to a stellar fly-by. *Monthly Notices of the Royal Astronomical Society,* 261(1), pp. 190-202.

Clark, P. C., Klessen, R. S. & Bonnell, I. A., 2007. Clump lifetimes and the initial mass function. *Monthly Notices of the Royal Astronomical Society,* 379(1), pp. 57-62.

Clement, M. S. & Kaib, N. A., 2020. Orbital Precession in the Distant Solar System: Further Constraining the Planet Nine Hypothesis with Numerical Simulations. *The Astronomical Journal,* 6, Volume 159, p. 285.

Concha-Ramírez, F., Wilhelm, M. J. C., Portegies Zwart, S. & Haworth, T. J., 2019. External photoevaporation of circumstellar discs constrains the time-scale for planet formation. *Monthly Notices of the Royal Astronomical Society,* 490(4), pp. 5678-5690.

Craig, J. & Krumholz, M. R., 2013. Close Stellar Encounters in Young, Substructured, Dissolving Star Clusters: Statistics and Effects on Planetary Systems. *The Astrophysical Journal,* 6, Volume 769, p. 150.

Crowther, P. A. et al., 2010. The R136 star cluster hosts several stars whose individual masses greatly exceed the accepted 150Msolar stellar mass limit. *Monthly Notices of the Royal Astronomical Society,* 408(2), pp. 731-751.

Da Rio, N. et al., 2010. A Multi-color Optical Survey of the Orion Nebula Cluster. II. The H-R Diagram. *The Astrophysical Journal,* 10, Volume 722, pp. 1092-1114.

Da Rio, N., Tan, J. C. & Jaehnig, K., 2014. The Structure, Dynamics, and Star Formation Rate of the Orion Nebula Cluster. *The Astrophysical Journal,* 11, Volume 795, p. 55.

Daffern-Powell, E. C. & Parker, R. J., 2020. Dynamical evolution of fractal structures in star-forming regions. *Monthly Notices of the Royal Astronomical Society,* 4, Volume 493, pp. 4925-4935.

Dale, J. E., Ercolano, B. & Bonnell, I. A., 2012. Ionizing feedback from massive stars in massive clusters - II. Disruption of bound clusters by photoionization. *Monthly Notices of the Royal Astronomical Society,* 424(1), pp. 377-392.

Damasso, M. et al., 2020. A precise architecture characterization of the π Mensae planetary system. *Astronomy & Astrophysics,* 642(A31), p. 14.

Dawson, R. I. & Johnson, J. A., 2018. Origins of Hot Jupiters. *Annual Review of Astronomy and Astrophysics,* Volume 56, pp. 175-221.

De Rosa, R. J., Dawson, R. & Nielsen, E. L., 2020. A significant mutual inclination between the planets within the π Mensae system. *Astronomy & Astrophysics,* 640(A73), p. 13.

Deacon, N. R., Schlieder, J. E. & Murphy, S. J., 2016. A nearby young M dwarf with a wide, possibly planetary-mass companion. *Monthly Notices of the Royal Astronomical Society,* 4, Volume 457, pp. 3191-3199.

Dehnen, W. & Read, J. I., 2011. N-body simulations of gravitational dynamics. *The European Physical Journal Plus,* Volume 126.

Deleuil, M. et al., 2020. Observational Constraints on the Formation and Evolution of Neptune-Class Exoplanets. *Space Science Reviews,* 216(6), p. A105.

Delgado, A. J., Djupvik, A. A., Costado, M. T. & Alfaro, E. J., 2013. Berkeley 94 and Berkeley 96: two young clusters with different dynamical evolution. *Monthly Notices of the Royal Astronomical Society,* 10, Volume 435, pp. 429-439.

Dobbs, C. L. et al., 2014. Formation of Molecular Clouds and Global Conditions for Star Formation. In: H. Beuther, R. Klessen, C. Dullemond & T. Henning, eds. *Protostars and Planets VI.* Tuscon: University of Arizona Press, pp. 3-26.

Downey, B. G. & Morbidelli, A., 2020. An attempt to constrain Planet Nine's orbit and position via resonant confinement of distant TNOs. *Monthly Notices of the Royal Astronomical Society,* 4, Volume 494, pp. 2045-2052.

Duchêne, G. & Kraus, A., 2013. Stellar Multiplicity. *Annual Review of Astronomy and Astrophysics,* Volume 51, pp. 269-310.

Dupuy, T. J. & Kraus, A. L., 2013. Distances, Luminosities, and Temperatures of the Coldest Known Substellar Objects. *Science,* 9, Volume 341, pp. 1492-1495.

Durkan, S., Janson, M. & Carson, J. C., 2016. High Contrast Imaging with Spitzer: Constraining the Frequency of Giant Planets out to 1000 au Separations. *The Astrophysical Journal,* 824(1), p. 58.

Eldridge, J. J., 2009. A new-age determination for γ2 Velorum from binary stellar evolution models. *Monthly Notices of the Royal Astronomical Society: Letters,* 400(1), pp. L20-L23.

Elmegreen, B. G., 1991. Cloud Formation by Combined Instabilities in Galactic Gas Layers: Evidence for a Q Threshold in the Fragmentation of Shearing Wavelets. *Astrophysical Journal,* Volume 378, p. 139.

Elmegreen, B. G., 2000. Star Formation in a Crossing Time. *The Astrophysical Journal,* 530(1), pp. 277-281.

Elmegreen, B. G. & Elmegreen, D. M., 2001. Fractal Structure in Galactic Star Fields. *The Astronomical Journal,* 3, Volume 121, pp. 1507-1511.

Fatuzzo, M. & Adams, F. C., 2008. UV Radiation Fields Produced by Young Embedded Star Clusters. *The Astrophysical Journal,* 675(2), pp. 1361-1374.

Fedele, D. et al., 2010. Timescale of mass accretion in pre-main-sequence stars. *Astronomy and Astrophysics,* 510(A72), p. 7.

Fienga, A. et al., 2020. New constraints on the location of P9 obtained with the INPOP19a planetary ephemeris. *Astronomy and Astrophysics,* 8, Volume 640, p. A6.

Flammini Dotti, F., Kouwenhoven, M. B. N., Cai, M. X. & Spurzem, R., 2019. Planetary systems in a star cluster I: the Solar system scenario. *Monthly Notices of the Royal Astronomical Society,* 10, Volume 489, pp. 2280-2297.

Forbrich, J. et al., 2016. The Population of Compact Radio Sources in the Orion Nebula Cluster. *The Astrophysical Journal,* 5, Volume 822, p. 93.

Forgan, D., Parker, R. J. & Rice, K., 2015. The dynamical fate of self-gravitating disc fragments after tidal downsizing. *Monthly Notices of the Royal Astronomical Society,* 2, Volume 447, pp. 836-845.

Foster, J. B. et al., 2015. IN-SYNC. II. Virial Stars from Subvirial Cores—the Velocity Dispersion of Embedded Pre-main-sequence Stars in NGC 1333. *The Astrophysical Journal,* 2, Volume 799, p. 136.

Fractal Foundation, 2021. *What are Fractals?.* [Online] Available at: https://fractalfoundation.org/resources/what-are-fractals/ [Accessed 21st November 2021].

Fregeau, J. M., Chatterjee, S. & Rasio, F. A., 2006. Dynamical Interactions of Planetary Systems in Dense Stellar Environments. *The Astrophysical Journal,* 4, Volume 640, pp. 1086-1098.

Fregeau, J. M., Cheung, P., Portegies Zwart, S. F. & Rasio, F. A., 2004. Stellar collisions during binary-binary and binary-single star interactions. *Monthly Notices of the Royal Astronomical Society,* 7, Volume 352, pp. 1-19.

Fujii, M. S. & Hori, Y., 2019. Survival rates of planets in open clusters: the Pleiades, Hyades, and Praesepe clusters. *Astronomy and Astrophysics,* 4, Volume 624, p. A110.

Gaudi, B. S., 2012. Microlensing Surveys for Exoplanets. *Annual Review of Astronomy and Astrophysics,* Volume 50, pp. 411-453.

Gieles, M. et al., 2006. Observational evidence for a truncation of the star cluster initial mass function at the high mass end. *Astronomy and Astrophysics,* 446(2), pp. L9-L12.

Gieles, M., Moeckel, N. & Clarke, C. J., 2012. Do all stars in the solar neighbourhood form in clusters? A cautionary note on the use of the distribution of surface densities. *Monthly Notices of the Royal Astronomical Society,* 10, Volume 426, pp. L11-L15.

Girichidis, P., Federrath, C., Banerjee, R. & Klessen, R. S., 2011. Importance of the initial conditions for star formation - I. Cloud evolution and morphology. *Monthly Notices of the Royal Astronomical Society,* 413(4), pp. 2741-2759.

Girichidis, P. et al., 2020. Physical Processes in Star Formation. *Space Science Reviews,* 216(4), p. 68.

Gomez, M., Hartmann, L., Kenyon, S. J. & Hewett, R., 1993. On the Spatial Distribution of pre-Main-Sequence Stars in Taurus. *The Astronomical Journal,* 5, Volume 105, p. 1927.

Goodwin, S. P., 1997. Residual gas expulsion from young globular clusters. *Monthly Notices of the Royal Astronomical Society,* 2, Volume 284, pp. 785-802.

Goodwin, S. P. & Bastian, N., 2006. Gas expulsion and the destruction of massive young clusters. *Monthly Notices of the Royal Astronomical Society,* 373(2), pp. 752-758.

Goodwin, S. P. & Whitworth, A. P., 2004. The dynamical evolution of fractal star clusters: The survival of substructure. *Astronomy and Astrophysics,* 1, Volume 413, pp. 929-937.

Goswami, J. N., 2004. Short-lived nuclides in the early solar system: the stellar connection. *New Astronomy Reviews,* 48(1-4), pp. 125-132.

Gouliermis, D. A., Hony, S. & Klessen, R. S., 2014. The complex distribution of recently formed stars. Bimodal stellar clustering in the star-forming region NGC 346. *Monthly Notices of the Royal Astronomical Society,* 4, Volume 439, pp. 3775-3789.

Goulinski, N. & Ribak, E. N., 2018. Capture of free-floating planets by planetary systems. *Monthly Notices of the Royal Astronomical Society,* 1, Volume 473, pp. 1589-1595.

Gounelle, M. & Meynet, G., 2012. Solar system genealogy revealed by extinct short-lived radionuclides in meteorites. *Astronomy & Astrophysics,* Volume 545, p. A4.

Gower, J. C. & Ross, G. J. S., 1969. Minimum Spanning Trees and Single Linkage Cluster Analysis. *Journal of the Royal Statistical Society. Series C (Applied Statistics),* 18(1), pp. 54-64.

Greaves, J. S. & Rice, W. K. M., 2010. Have protoplanetary discs formed planets?. *Monthly Notices of the Royal Astronomical Society,* 407(3), pp. 1981-1988.

Gutermuth, R. A. et al., 2009. A Spitzer Survey of Young Stellar Clusters Within One Kiloparsec of the Sun: Cluster Core Extraction and Basic Structural Analysis. *The Astrophysical Journals,* 9, Volume 184, pp. 18-83.

Gvaramadze, V. V. & Bomans, D. J., 2008. Search for OB stars running away from young star clusters. I. NGC 6611. *Astronomy and Astrophysics,* 490(3), pp. 1071-1077.

Hacar, A., Tafalla, M., Kauffmann, J. & Kovács, A., 2013. Cores, filaments, and bundles: hierarchical core formation in the L1495/B213 Taurus region. *Astronomy & Astrophysics,* Volume 554, p. A55.

Haisch, J., Lada, E. A. & Lada, C. J., 2001a. Disk Frequencies and Lifetimes in Young Clusters. *The Astrophysical Journal,* 6, Volume 553, pp. L153-L156.

Haisch, K. E. J., Lada, E. A. & Lada, C. J., 2001b. Circumstellar Disks in the IC 348 Cluster. *The Astronomical Journal,* 121(4), pp. 2065-2074.

Hao, W., Kouwenhoven, M. B. N. & Spurzem, R., 2013. The dynamical evolution of multiplanet systems in open clusters. *Monthly Notices of the Royal Astronomical Society,* 7, Volume 433, pp. 867-877.

Hartmann, L., 2003. Comments on Inferences of Star Formation Histories and Birth Lines. *The Astrophysical Journal,* 585(1), pp. 398-405.

Hartmann, L., Ballesteros-Paredes, J. & Bergin, E. A., 2001. Rapid Formation of Molecular Clouds and Stars in the Solar Neighborhood. *The Astrophysical Journal,* 562(3), pp. 852-868.

Haworth, T. J. & Clarke, C. J., 2019. The first multidimensional view of mass loss from externally FUV irradiated protoplanetary discs. *Monthly Notices of the Royal Astronomical Society,* 485(3), pp. 3895-3908.

Haworth, T. J. s. b. o. et al., 2018. The FRIED grid of mass-loss rates for externally irradiated protoplanetary discs. *Monthly Notices of the Royal Astronomical Society,* 481(1), pp. 452-466.

Heggie, D. C., 1975. Binary evolution in stellar dynamics. *Monthly Notices of the Royal Astronomical Society,* Volume 173, pp. 729-787.

Heggie, D. C. & Mathieu, R. D., 1986. Standardised Units and Time Scales. In: P. H. a. S. McMillan, ed. *The Use of Supercomputers in Stellar Dynamics.* Berlin: Springer Verlag, p. 233.

Helled, R. et al., 2014. Giant Planet Formation, Evolution, and Internal Structure. In: H. Beuther, R. S. Klessen, C. P. Dullemond & T. Henning, ed. *Protostars and Planets VI.* Tucson: University of Arizona Press, pp. 643-665.

Hendler, N. et al., 2020. The Evolution of Dust Disk Sizes from a Homogeneous Analysis of 1-10 Myr old Stars. *The Astrophysical Journal,* 895(2), p. 26.

Herbig, G. H., Vrba, F. J. & Rydgren, A. E., 1986. A spectroscopic survey of the Taurus-Auriga dark clouds for pre-main-sequence stars having CA II H, K emission. *Astronomical Journal,* Volume 91, pp. 575-582.

Hetem, A. & Gregorio-Hetem, J., 2019. Fractal statistics in young star clusters: structural parameters and dynamical evolution. *Monthly Notices of the Royal Astronomical Society,* 490(2), pp. 2521-2541.

Hetherington, N., 1997. Nebular hypothesis: Kant—Laplace. In: J. Shirley & R. W. Fairbridge, eds. *Encyclopedia of Planetary Science.* Dordrecht: Springer, pp. 519-520.

Hillenbrand, L. A., 1997. On the Stellar Population and Star-Forming History of the Orion Nebula Cluster. *The Astronomical Journal,* 5, Volume 113, pp. 1733-1768.

Hillenbrand, L. A. & Hartmann, L. W., 1998. A Preliminary Study of the Orion Nebula Cluster Structure and Dynamics. *The Astrophysical Journal,* 1, Volume 492, pp. 540-553.

Hills, J. G., 1975a. Encounters between binary and single stars and their effect on the dynamical evolution of stellar systems. *Astronomical Journal,* Volume 80, pp. 809-825.

Hills, J. G., 1975b. Effect of binary stars on the dynamical evolution of stellar clusters. II. Analytic evolutionary models. *Astronomical Journal,* Volume 80, pp. 1075-1080.

Huang, C. X., Petrovich, C. & Deibert, E., 2017. Dynamically Hot Super-Earths from Outer Giant Planet Scattering. *The Astronomical Journal,* Volume 153, p. 12.

Hughes, A. M., Duchêne, G. & Matthews, B. C., 2018. Debris Disks: Structure, Composition, and Variability. *Annual Review of Astronomy and Astrophysics ,* Volume 56, pp. 541-591.

Hurley, J. R. & Shara, M. M., 2002. Free-floating Planets in Stellar Clusters: Not So Surprising. *The Astrophysical Journal,* 2, Volume 565, pp. 1251-1256.

Jaehnig, K. O., Da Rio, N. & Tan, J. C., 2015. The Structural Evolution of Forming and Early Stage Star Clusters. *The Astrophysical Journal,* 1, Volume 798, p. 126.

Jaffa, S. E., Whitworth, A. P. & Lomax, O., 2017. Q^+: characterizing the structure of young star clusters. *Monthly Notices of the Royal Astronomical Society,* 4, Volume 466, pp. 1082-1092.

Jeans, J. H., 1902. The Stability of a Spherical Nebula. *Philosophical Transactions of the Royal Society of London,* 199(A), pp. 1-53.

Jeffries, R. D., 2017. Ages and age spreads in young stellar clusters. *Memorie della Societa Astronomica Italiana,* Volume 88, p. 637.

Johnson, J. A., Aller, K. M., Howard, A. W. & Crepp, J. R., 2010. Giant Planet Occurrence in the Stellar Mass-Metallicity Plane. *Publications of the Astronomical Society of the Pacific,* 122(894), p. 905.

Johnstone, D., Hollenbach, D. & Bally, J., 1998. Photoevaporation of Disks and Clumps by Nearby Massive Stars: Application to Disk Destruction in the Orion Nebula. *The Astrophysical Journal,* 499(2), pp. 758-776.

Kenyon, S. J. & Bromley, B. C., 2004. Stellar encounters as the origin of distant Solar System objects in highly eccentric orbits. *Nature,* 432(7017), pp. 598-602.

Keppler, M. et al., 2018. Discovery of a planetary-mass companion within the gap of the transition disk around PDS 70. *Astronomy & Astrophysics,* 617(A44), p. 21.

King, I., 1962. The structure of star clusters. I. an empirical density law. *Astronomical Journal,* Volume 67, p. 471.

King, I. R., 1966. The structure of star clusters. III. Some simple dynamical models. *Astronomical Journal,* Volume 71, p. 64.

King, R. R., Parker, R. J., Patience, J. & Goodwin, S. P., 2012. Testing the universality of star formation - I. Multiplicity in nearby star-forming regions. *Monthly Notices of the Royal Astronomical Society,* 4, Volume 421, pp. 2025-2042.

Kirk, H. & Myers, P. C., 2011. Young Stellar Groups and Their Most Massive Stars. *The Astrophysical Journal,* 2, Volume 727, p. 64.

Kley, W. & Nelson, R., 2012. Planet-Disk Interaction and Orbital Evolution. *Annual Review of Astronomy and Astrophysics,* Volume 50, pp. 211-249.

Korchagin, V. I. et al., 2003. Local Surface Density of the Galactic Disk from a Three-Dimensional Stellar Velocity Sample. *The Astronomical Journal,* 12, Volume 126, pp. 2896-2909.

Kouwenhoven, M. B. N., Shu, Q., Cai, M. X. & Spurzem, R., 2016. Planetary systems in star clusters. *Memoire della Societa Astronomica Italiana,* 1, Volume 87, p. 630.

Kratter, K. M., Murray-Clay, R. A. & Youdin, A. N., 2010. The Runts of the Litter: Why Planets Formed Through Gravitational Instability Can Only Be Failed Binary Stars. *The Astrophysical Journal,* 710(2), pp. 1375-1386.

Kroupa, P., 1995a. Inverse dynamical population synthesis and star formation. *Monthly Notices of the Royal Astronomical Society,* 12, Volume 277, p. 1491.

Kroupa, P., 1995b. The dynamical properties of stellar systems in the Galactic disc. *Monthly Notices of the Royal Astronomical Society,* 12, Volume 277, p. 1507.

Kroupa, P., 2008. Initial Conditions for Star Clusters. In: S. J. Aarseth, C. A. Tout & R. A. Mardling, eds. *The Cambridge N-Body Lectures.* Berlin Heidelberg: Springer-Verlag, p. 181.

Kroupa, P. & Petr-Gotzens, M. G., 2011. The initial period function of late-type binary stars and its variation. *Astronomy & Astrophysics,* Volume 529, p. A92.

Krumholz, M. R., 2014. The big problems in star formation: The star formation rate, stellar clustering, and the initial mass function. *Physics Reports,* Volume 539, pp. 49-134.

Krumholz, M. R., McKee, C. F. & Bland-Hawthorn, J., 2019. Star Clusters Across Cosmic Time. *Annual Review of Astronomy and Astrophysics,* Volume 57, pp. 227-303.

Kuhn, M. A. et al., 2014. The Spatial Structure of Young Stellar Clusters. I. Subclusters. *The Astrophysical Journal,* 6, Volume 787, p. 107.

Lada, C. J., 1987. Star formation: from OB associations to protostars. *IAU Symposium,* Volume 115, p. 1.

Lada, C. J. & Lada, E. A., 2003. Embedded Clusters in Molecular Clouds. *Annual Review of Astronomy and Astrophysics,* 1, Volume 41, pp. 57-115.

Larson, R. B., 1981. Turbulence and star formation in molecular clouds.. *Monthly Notices of the Royal Astronomical Society,* 3, Volume 194, pp. 809-826.

Larson, R. B., 1995. Star formation in groups. *Monthly Notices of the Royal Astronomical Society,* 1, Volume 272, pp. 213-220.

Laughlin, G. & Adams, F. C., 1998. The Modification of Planetary Orbits in Dense Open Clusters. *The Astrophysical Journal Letters,* 12, Volume 508, pp. L171-L174.

Lichtenberg, T. et al., 2019. A water budget dichotomy of rocky protoplanets from ^{26}Al-heating. *Nature Astronomy,* 2, Volume 3, pp. 307-313.

Lichtenberg, T., Parker, R. J. & Meyer, M. R., 2016. Isotopic enrichment of forming planetary systems from supernova pollution. *Monthly Notices of the Royal Astronomical Society,* 11, Volume 462, pp. 3979-3992.

Li, D., Mustill, A. J. & Davies, M. B., 2019. Fly-by encounters between two planetary systems I: Solar system analogues. *Monthly Notices of the Royal Astronomical Society,* 9, Volume 488, pp. 1366-1376.

Liffman, K., 2003. The Gravitational Radius of an Irradiated Disk. *Publications of the Astronomical Society of Australia,* 20(4), pp. 337-339.

Li, G. & Adams, F. C., 2016. Interaction Cross Sections and Survival Rates for Proposed Solar System Member Planet Nine. *The Astrophysical Journal Letters,* 5, Volume 823, p. L3.

Lin, Z., MacDonald, R. J., Kaltenegger, L. & Wilson, D. J., 2021. Differentiating modern and prebiotic Earth scenarios for TRAPPIST-1e: high-resolution transmission spectra and predictions for JWST. *Monthly Notices of the Royal Astronomical Society,* 505(3), pp. 3562-3578.

Li, Z. Y. et al., 2014. The Earliest Stages of Star and Planet Formation: Core Collapse, and the Formation of Disks and Outflows. In: H. Beuther, R. S. Klessen, C. P. Dullemond & T. Henning, eds. *Protostars and Planets VI.* Tuscon: University of Arizona Press, pp. 173-194.

Lodato, G. et al., 2019. The newborn planet population emerging from ring-like structures in discs. *Monthly Notices of the Royal Astronomical Society,* 486(1), pp. 453-461.

Lomax, O., Bates, M. L. & Whitworth, A. P., 2018. Modelling the structure of star clusters with fractional Brownian motion. *Monthly Notices of the Royal Astronomical Society,* 10, Volume 480, pp. 371-380.

Lomax, O., Whitworth, A. P. & Cartwright, A., 2011. Statistical comparison of clouds and star clusters. *Monthly Notices of the Royal Astronomical Society,* 3, Volume 412, pp. 627-633.

Longmore, S. N. et al., 2014. The Formation and Early Evolution of Young Massive Clusters. In: H. Beuther, R. S. Klessen, C. P. Dullemond & T. Henning, ed. *Protostars and Planets VI.* Tuscon: University of Arizona Press, pp. 291-314.

Looney, L. W., Tobin, J. J. & Fields, B. D., 2006. Radioactive Probes of the Supernova-contaminated Solar Nebula: Evidence that the Sun Was Born in a Cluster. *The Astrophysical Journal,* 652(2), pp. 1755-1762.

Luhman, K. L., 2007. The Stellar Population of the Chamaeleon I Star-forming Region. *The Astrophysical Journals,* 11, Volume 173, pp. 104-136.

Luhman, K. L. et al., 2010. The Disk Population of the Taurus Star-Forming Region. *The Astrophysical Journals,* 1, Volume 186, pp. 111-174.

Luhman, K. L., Burgasser, A. J. & Bochanski, J. J., 2011. Discovery of a Candidate for the Coolest Known Brown Dwarf. *The Astrophysical Journal Letters,* 3, Volume 730, p. L9.

Luhman, K. L., Esplin, T. L. & Loutrel, N. P., 2016. A Census of Young Stars and Brown Dwarfs in IC 348 and NGC 1333. *The Astrophysical Journal,* 8, Volume 827, p. 52.

Lustig-Yaeger, J., Meadows, V. S. & Lincowski, A. P., 2019. The Detectability and Characterization of the TRAPPIST-1 Exoplanet Atmospheres with JWST. *The Astronomical Journal,* 158(1), p. 28.

Lynden-Bell, D., 1967. Statistical mechanics of violent relaxation in stellar systems. *Monthly Notices of the Royal Astronomical Society,* Volume 136, p. 101.

Madau, P. & Dickinson, M., 2014. Cosmic Star-Formation History. *Annual Review of Astronomy and Astrophysics,* Volume 52, pp. 415-486.

Makino, J., 1991. A Modified Aarseth Code for GRAPE and Vector Processors. *Publications of the Astronomical Society of Japan,* Volume 43, pp. 859-876.

Makino, J. & Aarseth, S. J., 1992. On a Hermite Integrator with Ahmad-Cohen Scheme for Gravitational Many-Body Problems. *Publications of the Astronomical Society of Japan,* Volume 44, pp. 141-151.

Mamajek, E. E., 2009. Initial Conditions of Planet Formation: Lifetimes of Primordial. In: M. T. a. M. I. T. Usuda, ed. *Exoplanets and Disks: Their Formation and Diversity.* Keauhou, Hawaii: American Institute of Physics Conference Series, pp. 3-10.

Mann, A. W. et al., 2017. Zodiacal Exoplanets in Time (ZEIT). IV. Seven Transiting Planets in the Praesepe Cluster. *The Astronomical Journal,* 153(2), p. 15.

Marks, M. & Kroupa, P., 2012. Inverse dynamical population synthesis. Constraining the initial conditions of young stellar clusters by studying their binary populations. *Astronomy and Astrophysics,* 7, Volume 543, p. A8.

Marois, C. et al., 2008. Direct Imaging of Multiple Planets Orbiting the Star HR 8799. *Science,* 322(5906), p. 1348.

Maschberger, T., 2013. On the function describing the stellar initial mass function. *Monthly Notices of the Royal Astronomical Society,* 2, Volume 429, pp. 1725-1733.

Maschberger, T. & Clarke, C. J., 2008. Maximum stellar mass versus cluster membership number revisited. *Monthly Notices of the Royal Astronomical Society,* 391(2), pp. 711-717.

Masuda, K. & Winn, J. N., 2017. Reassessment of the Null Result of the HST Search for Planets in 47 Tucanae. *The Astronomical Journal,* Volume 153, p. 8.

Mayer, L., Quinn, T., Wadsley, J. & Stadel, J., 2002. Formation of Giant Planets by Fragmentation of Protoplanetary Disks. *Science,* 11, Volume 298, pp. 1756-1759.

Mayer, L., Quinn, T., Wadsley, J. & Stadel, J., 2002. Formation of Giant Planets by Fragmentation of Protoplanetary Disks. *Science,* 298(5599), pp. 1756-1759.

Mayor, M. & Queloz, D., 1995. A Jupiter-mass companion to a solar-type star. *Nature,* 378(6555), pp. 355-359.

McKee, C. F. & Ostriker, E. C., 2007. Theory of Star Formation. *Annual Review of Astronomy and Astrophysics,* Volume 45, pp. 565-687.

McMillan, S. L. W., 1986. A Unified N-Body and Statistical Treatment of Stellar Dynamics. III. Early Postcollapse Evolution of Globular Clusters. *Astrophysical Journal,* Volume 307, p. 126.

McMillan, S. L. W. & Hut, P., 1996. Binary-Single-Star Scattering. VI. Automatic Determination of Interaction Cross Sections. *Astrophysical Journal,* Volume 467, p. 348.

Meru, F., 2015. Triggered fragmentation in self-gravitating discs: forming fragments at small radii. *Monthly Notices of the Royal Astronomical Society,* 454(3), pp. 2529-258.

Mestel, L. & Spitzer, L. J., 1956. Star formation in magnetic dust clouds. *Monthly Notices of the Royal Astronomical Society,* Volume 116, p. 503.

Mikkola, S. & Aarseth, S. J., 1998. An efficient integration method for binaries in N-body simulations. *New Astronomy,* 3(5), pp. 309-320.

Miville-Deschênes, M. et al., 2010. Herschel-SPIRE observations of the Polaris flare: Structure of the diffuse interstellar medium at the sub-parsec scale. *Astronomy and Astrophysics,* 518(L92), p. 5.

Monteux, J. et al., 2018. Water and the Interior Structure of Terrestrial Planets and Icy Bodies. *Space Science Reviews,* 2, Volume 214, p. 39.

Mróz, P., Radosław, P., Cheongho, H. *et al.*, 2020. A Free-floating or Wide-orbit Planet in the Microlensing Event OGLE-2019-BLG-0551. *Astronomical Journal,* 6, Volume 159, p. 262.

Mróz, P., Udalski, A., Skowron, J. *et al.,* 2017. No large population of unbound or wide-orbit Jupiter-mass planets. *Nature,* 8, Volume 548, pp. 183-186.

Mróz, P., Udalski, A., Bennett, D. *et al.*, 2019. Two new free-floating or wide-orbit planets from microlensing. *Astronomy & Astrophysics,* Volume 622, p. A201.

Mustill, A. J., Raymond, S. N. & Davies, M. B., 2016. Is there an exoplanet in the Solar system?. *Monthly Notices of the Royal Astronomical Society,* 7, Volume 460, pp. L109-L113.

Myers, P. C., 2009. Filamentary Structure of Star-forming Complexes. *The Astrophysical Journal,* 700(2), pp. 1609-1625.

Napier, K. J. et al., 2021. No Evidence for Orbital Clustering in the Extreme Trans-Neptunian Objects. *arXiv e-prints,* 2.p. arXiv:2102.05601.

Naud, M.-E.et al., 2014. Discovery of a Wide Planetary-mass Companion to the Young M3 Star GU Psc. *The Astrophysical Journal,* 787(1), p. 16.

Nesvorný, D., 2018. Dynamical Evolution of the Early Solar System. *Annual Review of Astronomy and Astrophysics,* Volume 56, pp. 137-174.

Nicholson, R. B. & Parker, R. J., 2017. Supernova enrichment of planetary systems in low-mass star clusters. *Monthly Notices of the Royal Astronomical Society,* 2, Volume 464, pp. 4318-4324.

Nicholson, R. B. et al., 2019. Rapid destruction of protoplanetary discs due to external photoevaporation in star-forming regions. *Monthly Notices of the Royal Astronomical Society,* 6, Volume 485, pp. 4893-4905.

Nixon, C. J., King, A. R. & Pringle, J. E., 2018. The Maximum Mass Solar Nebula and the early formation of planets. *Monthly Notices of the Royal Astronomical Society,* 477(3), pp. 3273-3278.

O'dell, C. R., Wen, Z. & Hu, X., 1993. Discovery of New Objects in the Orion Nebula on HST Images: Shocks, Compact Sources, and Protoplanetary Disks. *Astrophysical Journal ,* Volume 410, p. 696.

Offner, S. S. R. et al., 2014. The Origin and Universality of the Stellar Initial Mass Function. In: H. Beuther, R. S. Klessen, C. P. Dullemond & a. T. Henning, eds. *Protostars and Planets VI.* Tuscon: University of Arizona Press, pp. 53-75.

Önehag, A. et al., 2011. M67-1194, an unusually Sun-like solar twin in M67. *Astronomy & Astrophysics,* Volume 528, p. A85.

Owen, J. E., 2020. Snow lines can be thermally unstable. *Monthly Notices of the Royal Astronomical Society,* 495(3), pp. 3160-3174.

Pan, M. & Schlichting, H. E., 2012. Self-consistent Size and Velocity Distributions of Collisional Cascades. *The Astrophysical Journal,* 747(2), p. 10.

Parker, R., 2020. The birth environment of planetary systems. *Royal Society Open Science,* Volume 7.

Parker, R. J., 2014. Dynamics versus structure: breaking the density degeneracy in star formation. *Monthly Notices of the Royal Astronomical Society,* 12, Volume 445, pp. 4037-4044.

Parker, R. J., 2018. On the spatial distributions of dense cores in Orion B. *Monthly Notices of the Royal Astronomical Society,* 5, Volume 476, pp. 617-629.

Parker, R. J. & Alves de Oliveira, C., 2017. Dynamical histories of the IC 348 and NGC 1333 star-forming regions in Perseus. *Monthly Notices of the Royal Astronomical Society,* 7, Volume 468, pp. 4340-4350.

Parker, R. J., Church, R. P., Davies, M. B. & Meyer, M. R., 2014. Supernova enrichment and dynamical histories of solar-type stars in clusters. *Monthly Notices of the Royal Astronomical Society,* 437(1), pp. 946-958.

Parker, R. J. & Dale, J. E., 2015. On the spatial distributions of stars and gas in numerical simulations of molecular clouds. *Monthly Notices of the Royal Astronomical Society,* 8, Volume 451, pp. 3664-3670.

Parker, R. J. & Dale, J. E., 2016. Did the Solar system form in a sequential triggered star formation event?. *Monthly Notices of the Royal Astronomical Society,* 2, Volume 456, pp. 1066-1072.

Parker, R. J. & Goodwin, S. P., 2007. Do O-stars form in isolation?. *Monthly Notices of the Royal Astronomical Society,* 380(3), pp. 1271-1275.

Parker, R. J. & Goodwin, S. P., 2012. The same, but different: stochasticity in binary destruction. *Monthly Notices of the Royal Astronomical Society,* 424(1), pp. 272-281.

Parker, R. J., Goodwin, S. P. & Allison, R. J., 2011. The evolution of binary populations in cool, clumpy star clusters. *Monthly Notices of the Royal Astronomical Society,* 12, Volume 418, pp. 2565-2575.

Parker, R. J. et al., 2016. Mass segregation in star clusters is not energy equipartition. *Monthly Notices of the Royal Astronomical Society: Letters,* 459(1), pp. L119-L123.

Parker, R. J., Lichtenberg, T. & Quanz, S. P., 2017. Was Planet 9 captured in the Sun's natal star-forming region?. *Monthly Notices of the Royal Astronomical Society,* 11, Volume 472, pp. L75-L79.

Parker, R. J. & Meyer, M. R., 2012. Characterizing the dynamical state of star clusters from snapshots of their spatial distributions. *Monthly Notices of the Royal Astronomical Society,* 11, Volume 427, pp. 637-650.

Parker, R. J. & Meyer, M. R., 2014. Binaries in the field: fossils of the star formation process?. *Monthly Notices of the Royal Astronomical Society,* 8, Volume 442, pp. 3722-3736.

Parker, R. J., Nicholson, R. B. & Alcock, H. L., 2021. Far and extreme ultraviolet radiation fields and consequent disc destruction in star-forming regions. *Monthly Notices of the Royal Astronomical Society,* 502(2), pp. 2665-2681.

Parker, R. J. & Quanz, S. P., 2012. The effects of dynamical interactions on planets in young substructured star clusters. *Monthly Notices of the Royal Astronomical Society,* 1, Volume 419, pp. 2448-2458.

Parker, R. J. & Reggiani, M. M., 2013. The binary companion mass ratio distribution: an imprint of the star formation process?. *Monthly Notices of the Royal Astronomical Society,* 7, Volume 432, pp. 2378-2384.

Parker, R. J. & Wright, N. J., 2018. Evolution of spatio-kinematic structures in star-forming regions: are Friends of Friends worth knowing?. *Monthly Notices of the Royal Astronomical Society,* 481(2), pp. 1679-1689.

Parker, R. J., Wright, N. J., Goodwin, S. P. & Meyer, M. R., 2014. Dynamical evolution of star-forming regions. *Monthly Notices of the Royal Astronomical Society,* 2, Volume 438, pp. 620-638.

Perets, H. B. & Kouwenhoven, M. B. N., 2012. On the Origin of Planets at Very Wide Orbits from the Recapture of Free Floating Planets. *The Astrophysical Journal,* 5, Volume 750, p. 83.

Peretto, N. et al., 2012. The Pipe Nebula as seen with Herschel: formation of filamentary structures by large-scale compression?. *Astronomy & Astrophysics,* 541(A63), p. 8.

Pfalzner, S., Bhandare, A., Vincke, K. & Lacerda, P., 2018. Outer Solar System Possibly Shaped by a Stellar Fly-by. *The Astrophysical Journal,* 8, Volume 863, p. 45.

Pineda, J. E. et al., 2015. The formation of a quadruple star system with wide separation. *Nature,* Volume 518, pp. 213-215.

Pinte, C. et al., 2020. Nine Localized Deviations from Keplerian Rotation in the DSHARP Circumstellar Disks: Kinematic Evidence for Protoplanets Carving the Gaps. *The Astrophysical Journal Letters,* 890(1), p. L9.

Plummer, H. C., 1911. On the problem of distribution in globular star clusters. *Monthly Notices of the Royal Astronomical Society,* 3, Volume 71, pp. 460-470.

Plummer, H. C., 1911. On the problem of distribution in globular star clusters. *Monthly Notices of the Royal Astronomical Society,* Volume 71, pp. 460-470.

Pollack, J. B. et al., 1996. Formation of the Giant Planets by Concurrent Accretion of Solids and Gas. *Icarus,* 11, Volume 124, pp. 62-85.

Porras, A. et al., 2003. A Catalog of Young Stellar Groups and Clusters within 1 Kiloparsec of the Sun. *The Astronomical Journal,* 126(4), pp. 1916-1924.

Portegies Zwart, S., 2019. The formation of solar-system analogs in young star clusters. *Astronomy and Astrophysics,* 2, Volume 622, p. A69.

Portegies Zwart, S. F., Hut, P., Makino, J. & McMillan, S. L. W., 1998. On the dissolution of evolving star clusters. *Astronomy and Astrophysics,* Volume 337, pp. 363-371.

Portegies Zwart, S. F., Makino, J., McMillan, S. L. W. & Hut, P., 1999. Star cluster ecology. III. Runaway collisions in young compact star clusters. *Astronomy and Astrophysics,* 8, Volume 348, pp. 117-126.

Portegies Zwart, S. F., McMillan, S. L. W. & Gieles, M., 2010. Young Massive Star Clusters. *Annual Review of Astronomy and Astrophysics,* Volume 48, pp. 431-493.

Portegies Zwart, S. F., McMillan, S. L. W., Hut, P. & Makino, J., 2001. Star cluster ecology - IV. Dissection of an open star cluster: photometry. *Monthly Notices of the Royal Astronomical Society,* 2, Volume 321, pp. 199-226.

Poveda, A., Ruiz, J. & Allen, C., 1967. Run-away Stars as the Result of the Gravitational Collapse of Proto-stellar Clusters. *Boletín de los Observatorios de Tonantzintla y Tacubaya,* Volume 4, pp. 86-90.

Pu, B. & Lai, D., 2021. Strong Scatterings of Cold Jupiters and their Influence on Inner. *Monthly Notices of the Royal Astronomical Society,* 508(1), pp. 597-616.

Quanz, S. P. et al., 2015. Confirmation and Characterization of the Protoplanet HD 100546 b—Direct Evidence for Gas Giant Planet Formation at 50 AU. *The Astrophysical Journal,* 807(64), p. 13.

Quanz, S. P. et al., 2012. Direct imaging constraints on planet populations detected by microlensing. *Astronomy and Astrophysics,* 5, Volume 541, p. A133.

Quinn, S. N. et al., 2012. Two "b"s in the Beehive: The Discovery of the First Hot Jupiters in an Open Cluster. *The Astrophysical Journal Letters,* 756(2), p. L33.

Rafikov, R. R., 2005. Can Giant Planets Form by Direct Gravitational Instability?. *The Astrophysical Journal,* 621(1), pp. L69-72.

Raymond, S. N. et al., 2014. Terrestrial Planet Formation at Home and Abroad. In: H. Beuther, R. S. Klessen, C. P. Dullemond & a. T. Henning, eds. *Protostars and Planets VI.* Tuscon: University of Arizona Press, pp. 595-618.

Reggiani, M. et al., 2011. Quantitative evidence of an intrinsic luminosity spread in the Orion nebula cluster. *Astronomy and Astrophysics,* 10, Volume 534, p. A83.

Richert, A. J. W. et al., 2018. Circumstellar disc lifetimes in numerous galactic young stellar clusters. *Monthly Notices of the Royal Astronomical Society,* 477(4), pp. 5191-5206.

Rosotti, G. P. et al., 2014. Protoplanetary disc evolution affected by star-disc interactions in young stellar clusters. *Monthly Notices of the Royal Astronomical Society,* 441(3), pp. 2094-2110.

Salpeter, E. E., 1955. The Luminosity Function and Stellar Evolution. *Astrophysical Journal,* Volume 121, p. 161.

Sánchez, N. & Alfaro, E. J., 2009. The Spatial Distribution of Stars in Open Clusters. *The Astrophysical Journal,* 5, Volume 696, pp. 2086-2093.

Scally, A. & Clarke, C., 2001. Destruction of protoplanetary discs in the Orion Nebula Cluster. *Monthly Notices of the Royal Astronomical Society,* 325(2), pp. 449-456.

Schaller, G., Schaerer, D., Meynet, G. & Maeder, A., 1992. New grids of stellar models from 0.8 to 120 $M_\odot$ at Z=0.020 and Z=0.001. *Astronomy and Astrophysics Supplement,* Volume 96, p. 269.

Schmeja, S., 2011. Identifying star clusters in a field: A comparison of different algorithms. *Astronomische Nachrichten,* 2, Volume 332, p. 172.

Schmeja, S. & Klessen, R. S., 2006. Evolving structures of star-forming clusters. *Astronomy and Astrophysics,* 4, Volume 449, pp. 151-159.

Schoettler, C., de Bruijne, J., Vaher, E. & Parker, R. J., 2020. Runaway and walkaway stars from the ONC with Gaia DR2. *Monthly Notices of the Royal Astronomical Society,* 495(3), pp. 3104-3123.

Segura-Cox, D. M. et al., 2020. Four annular structures in a protostellar disk less than 500,000 years old. *Nature,* 586(7828), pp. 228-231.

Shankman, C. et al., 2017. OSSOS. VI. Striking Biases in the Detection of Large Semimajor Axis Trans-Neptunian Objects. *The Astronomical Journal,* 8, Volume 154, p. 50.

Sheppard, S. S. & Trujillo, C., 2016. New Extreme Trans-Neptunian Objects: Toward a Super-Earth in the Outer Solar System. *The Astronomical Journal,* 12, Volume 152, p. 221.

Shu, F. H., Adams, F. C. & Lizano, S., 1987. Star formation in molecular clouds: observation and theory. *Annual Review of Astronomy and Astrophysics,* Volume 25, pp. 23-81.

Sigurdsson, S. et al., 2003. A Young White Dwarf Companion to Pulsar B1620-26: Evidence for Early Planet Formation. *Science,* 301(5630), pp. 193-196.

Sills, A. et al., 2018. Dynamical evolution of stars and gas of young embedded stellar sub-clusters. *Monthly Notices of the Royal Astronomical Society,* 477(2), pp. 1903-1912.

Smith, A. M. S. et al., 2018. K2-137 b: an Earth-sized planet in a 4.3-h orbit around an M-dwarf. *Monthly Notices of the Royal Astronomical Society,* 464(4), pp. 5523-5533.

Smith, K. W. & Bonnell, I. A., 2001. Free-floating planets in stellar clusters?. *Monthly Notices of the Royal Astronomical Society,* 3, Volume 322, pp. L1-L4.

Soderblom, D. R. et al., 2014. Ages of Young Stars. In: *Protostars and Planets VI.* Tuscon: The University of Arizona Press, p. 219.

Spera, M., Mapelli, M. & Jeffries, R. D., 2016. Do open star clusters evolve towards energy equipartition?. *Monthly Notices of the Royal Astronomical Society,* 460(1), pp. 317-328.

Spitzer, L., 1987. *Dynamical evolution of globular clusters.* Princeton: Princeton University Press.

Spitzer, L. J., 1969. Equipartition and the Formation of Compact Nuclei in Spherical Stellar Systems. *Astrophysical Journal,* Volume 158, p. L139.

Spurzem, R., Giersz, M., Heggie, D. C. & Lin, D. N. C., 2009. Dynamics of Planetary Systems in Star Clusters. *The Astrophysical Journal,* 5, Volume 697, pp. 458-482.

Sternberg, A., Hoffmann, T. L. & Pauldrach, A. W. A., 2003. Ionizing Photon Emission Rates from O- and Early B-Type Stars and Clusters. *The Astrophysical Journal,* 599(2), pp. 1333-1343.

Störzer, H. & Hollenbach, D., 1999. Photodissociation Region Models of Photoevaporating Circumstellar Disks and Application to the Proplyds in Orion. *The Astrophysical Journal,* 515(2), pp. 669-684.

Sumi, T., Kamiya, K., Bennett, D., *et al.*, 2011. Unbound or distant planetary mass population detected by gravitational microlensing. *Nature,* 5, Volume 473, pp. 349-352.

Tan, J. C. et al., 2014. Massive Star Formation. In: R. S. K. C. P. D. a. T. H. Henrik Beuther, ed. *Protostars and Planets VI.* Tucson: University of Arizona Press, pp. 149-172.

Toomre, A., 1964. On the gravitational stability of a disk of stars.. *Astrophysical Journal,* Volume 139, pp. 1217-1238.

Trujillo, C. A. & Sheppard, S. S., 2014. A Sedna-like body with a perihelion of 80 astronomical units. *Nature,* 3, Volume 507, pp. 471-474.

Tutukov, A. V., 1978. Early Stages of Dynamical Evolution of Star Cluster Models. *Astronomy and Astrophysics,* 11, Volume 70, p. 57.

Vacca, W. D., Garmany, C. D. & Shull, J. M., 1996. The Lyman-Continuum Fluxes and Stellar Parameters of O and Early B-Type Stars. *Astrophysical Journal,* Volume 460, p. 914.

van Elteren, A. et al., 2019. Survivability of planetary systems in young and dense star clusters. *Astronomy and Astrophysics,* 4, Volume 624, p. A120.

Venturini, J., Ronco, M. P. & Guilera, O. M., 2020. Setting the Stage: Planet Formation and Volatile Delivery. *Space Science Reviews,* 216(5), p. A86.

Vincke, K. & Pfalzner, S., 2016. Cluster Dynamics Largely Shapes Protoplanetary Disk Sizes. *The Astrophysical Journal,* 828(1), p. 10.

Wang, L. et al., 2015. Close encounters involving free-floating planets in star clusters. *Monthly Notices of the Royal Astronomical Society,* 6, Volume 449, pp. 3543-3558.

Wang, Y.-H., Perna, R. & Leigh, N. W. C., 2020. Giant Planet Swaps during Close Stellar Encounters. *The Astrophysical Journal Letters,* 3, Volume 891, p. L14.

Wang, Y.-H., Perna, R. & Leigh, N. W. C., 2020. Planetary Architectures in Interacting Stellar Environments. *Monthly Notices of the Royal Astronomical Society,* 6.

Ward-Thompson, D. & Whitworth, A. P., 2011. *An Introduction to Star-Formation.* Cambridge: Cambridge University Press.

Weidner, C. & Kroupa, P., 2006. The maximum stellar mass, star-cluster formation and composite stellar populations. *Monthly Notices of the Royal Astronomical Society,* 365(4), pp. 1333-1347.

Williams, J. P. & Cieza, L. A., 2011. Protoplanetary Disks and Their Evolution. *Annual Review of Astronomy and Astrophysics,* 9, Volume 49, pp. 67-117.

Winn, J. N. & Fabrycky, D. C., 2015. The Occurrence and Architecture of Exoplanetary Systems. *Annual Review of Astronomy and Astrophysics,* Volume 53, pp. 409-447.

Winter, A. J. et al., 2018. Protoplanetary disc truncation mechanisms in stellar clusters: comparing external photoevaporation and tidal encounters. *Monthly Notices of the Royal Astronomical Society,* 478(2), pp. 2700-2722.

Winter, A. J., Kruijssen, J. M. D., Longmore, S. N. & Chevance, M., 2020. Stellar clustering shapes the architecture of planetary systems. *Nature,* 10, Volume 586, pp. 528-532.

Xuan, J. W. & Wyatt, M. C., 2020. Evidence for a high mutual inclination between the cold Jupiter and transiting super Earth orbiting π Men. *Monthly Notices of the Royal Astronomical Society,* 497(2), pp. 2096-2118.

Zapatero Osorio, M. R. et al., 2000. Discovery of Young, Isolated Planetary Mass Objects in the Sigma Orionis Star Cluster. *Science,* 10, Volume 290, pp. 103-107.

Zheng, X., Kouwenhoven, M. B. N. & Wang, L., 2015. The dynamical fate of planetary systems in young star clusters. *Monthly Notices of the Royal Astronomical Society,* 11, Volume 453, pp. 2759-2770.

Zhu, W. & Dong, S., 2021. Exoplanet Statistics and Theoretical Implications. *Annual Review of Astronomy and Astrophysics ,* Volume 59, pp. 293-338.

Zinnecker, H. & Yorke, H. W., 2007. Toward Understanding Massive Star Formation. *Annual Review of Astronomy and Astrophysics,* Volume 45, pp. 481-563.